INVESTIGATION OF A HA/PDLGA/CARBON FOAM MATERIAL SYSTEM FOR ORTHOPEDIC FIXATION PLATES BASED ON TIME-DEPENDENT PROPERTIES

A Dissertation

by

DOUGLAS EUGENE RODRIGUEZ

Submitted to the Office of Graduate Studies of
Texas A&M University
in partial fulfillment of the requirements for the degree of

DOCTOR OF PHILOSOPHY

August 2009

Major Subject: Mechanical Engineering

INVESTIGATION OF A HA/PDLGA/CARBON FOAM MATERIAL SYSTEM FOR ORTHOPEDIC FIXATION PLATES BASED ON TIME-DEPENDENT PROPERTIES

A Dissertation

by

DOUGLAS EUGENE RODRIGUEZ

Submitted to the Office of Graduate Studies of
Texas A&M University
in partial fulfillment of the requirements for the degree of

DOCTOR OF PHILOSOPHY

Approved by:

Chair of Committee,	Ozden O. Ochoa
Committee Members,	Hung-Jue Sue
	Harry Hogan
	William Hyman
	Sharon Kerwin
Head of Department,	Dennis O'Neal

August 2009

Major Subject: Mechanical Engineering

ABSTRACT

Investigation of a HA/PDLGA/Carbon Foam Material System for Orthopedic Fixation Plates Based on Time-Dependent Properties. (August 2009)

Douglas Eugene Rodriguez, B.S., Texas A&M University;

M.S., Texas A&M University

Chair of Advisory Committee: Dr. Ozden O. Ochoa

While there is continuing interest in bioresorbable materials for orthopedic fixation devices, the major challenge in utilizing these materials in load-bearing applications is creating materials sufficiently stiff and strong to sustain loads throughout healing while maintaining fracture stability. The primary aim of this study is to quantify the degradation rate of a bioresorbable material system, then use this degradation rate to determine the material response of an orthopedic device made of the same material as healing progresses. The present research focuses on the development and characterization of a material system consisting of carbon foam infiltrated with hydroxyapatite (HA) reinforced poly($_{D,L}$-lactide)-co-poly(glycolide) (PDLGA). A processing technique is developed to infiltrate carbon foam with HA/PDLGA and material morphology is investigated. Additionally, short-term rat osteoblast cell studies are undertaken to establish a starting point for material biocompatibility. Degradation experiments are conducted to elicit the time-dependent properties of the material system at the material scale. These properties are then incorporated into computational models

of an internal plate attached to a fractured human femur to design and predict the material response to applied physiological loads. Results from this work demonstrate the importance of material dissolution rate as well as material strength when designing internal fixation plates.

To My Family

ACKNOWLEDGEMENTS

I would like to express my thanks to my committee chair, Dr. Ozden O. Ochoa, whose support, guidance, and encouragement over the past decade has shaped my life in ways I am eternally grateful. I would also like to thank Dr. H.J. Sue, Dr. Harry Hogan, Dr. Sharon Kerwin, and Dr. William Hyman for sharing their valuable insight and feedback as committee members. I also appreciate the contributions from Dr. Mariah Hahn in her help with the cell studies in this work.

I am especially grateful for the interaction and support of my labmates, classmates, and fellow graduate students throughout this journey over the years.

Finally, I would like to express my unending gratitude to both my immediate and my extended family. Without your support this would not be possible.

TABLE OF CONTENTS

Page

Page

Page

LIST OF FIGURES

FIGURE Page

FIGURE Page

FIGURE Page

FIGURE Page

FIGURE Page

FIGURE Page

LIST OF TABLES

1. INTRODUCTION

1.1 Significance, Objectives, and Outcomes

The use of bioresorbable polymers, materials that degrade within the body and are resorbed through the body's metabolic cycle, has been proposed for orthopedic applications since the advent of these polymers as a biomaterial[1]. Since the introduction of DEXON™ in 1970, the first commercially-available, fully resorbable suture[2], bioresorbable polymers have been investigated for stents, drug delivery, tissue scaffolds, and orthopedic applications. These materials are especially attractive for orthopedic devices because of the degradative nature of the material. Here, there are two main advantages: 1) the use of bioresorbable materials in these devices eliminates the necessity of further surgeries to remove the device, and 2) the gradual reduction of stiffness allows load transfer to the bone as it heals, thus having the potential to avoid stress protection atrophy in load-bearing bones.

The appeal of using bioresorbable polymers in load-bearing orthopedic applications lies in the potential for stress protection atrophy with the use of standard titanium alloy or fixation plates[3]. Once bone union is achieved in a fracture bridged with these rigid plates, the plate continues to carry a large portion of the applied loads because of the mismatch of stiffness between plate and bone. This action prevents the bone from realizing normal stress levels; it is this shielding effect that results in reduced

---

This dissertation follows the style of Biomaterials.

bone mass as the bone responds to the reduced stress state, as stated by Wolff's law[†][3, 4]. This phenomenon is a cause for concern because upon removal of the fixation plate, the shielded area of bone then experiences increased stress levels, sometimes leading to fracture. As such, bioresorbable polymers have been the recent focus of research aimed at decreasing the probability for occurrence of stress protection atrophy.

There indeed have been numerous bioresorbable orthopedic devices commercially available, among them are pins, screws, internal fixation plates, suture anchors, meshes, and staples[8, 9]. Examples of these devices are shown in Figure 1.1. These applications, however, are limited to areas where low stress is experienced, such as interference screws in the ankle, knee, and hand, and screws and plates for craniomaxillofacial fixation[9, 10]. Here, these devices are intended to stabilize the fracture until union is achieved; the devices are not intended to transfer loads across the interfragmentary gap in load-bearing situations.

The major challenge in utilizing these bioresorbable materials in load-bearing applications is creating materials sufficiently stiff and strong to sustain loads throughout healing while maintaining fracture stability. As shown in Tables 1.1 and 1.2, the mechanical properties of bone and bioresorbable polymers are an order of magnitude different. As such, most of the research on resorbable biomaterials (where mechanical properties are the primary concern) focuses on: 1) the initial *modulus* and strength of potential material systems (at a material scale), and 2) the experimentally measured

[†] Although there is debate in the scientific community as to the validity of Wolff's original concept referred to as "Wolff's law" [5-7], the general concept of "bone functional adaption" is recognized whereby "over time, the mechanical load applied to living bone influences the structure of bone tissue" [6].

change in *stiffness* and strength of devices as a result of degradation. Here, modulus and stiffness are italicized to emphasize the difference between the mechanical property on a material scale and a structural scale. There is a gap in the literature regarding the tailoring of degradation rates to healing rates at a material scale, as will be demonstrated in the literature survey in the next section.

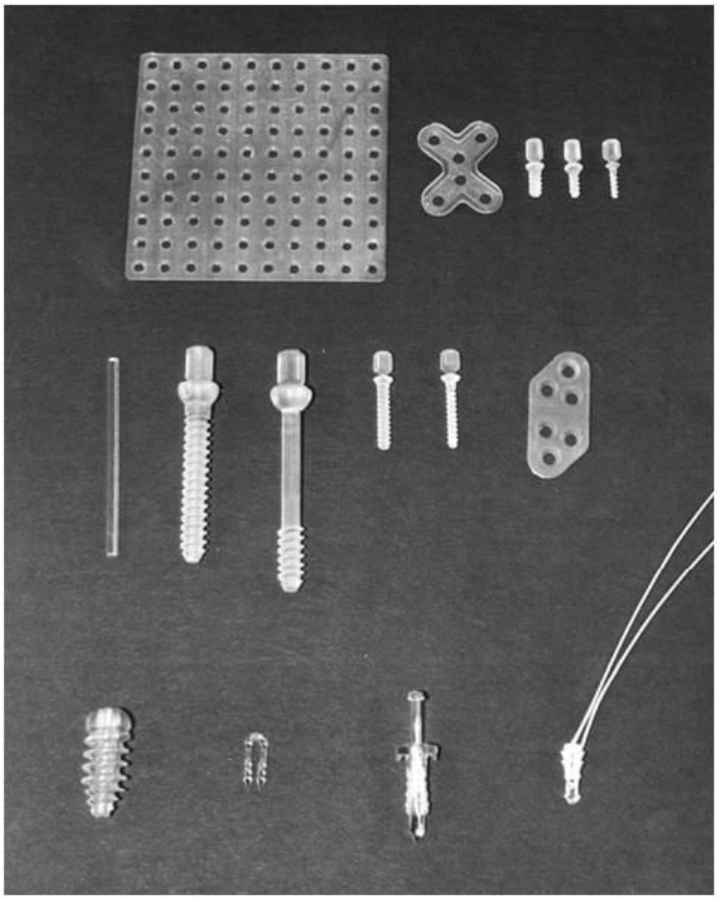

Figure 1.1. Image of bioresorbable orthopedic devices: (top row) craniomaxillofacial mesh, plate, and screws; (middle row) orthopedic pins, screws, plate; (bottom row) ACL interference screw, meniscal staple, shoulder rivet, and suture anchor. (from Pietrzak[11])

Table 1.1. Mechanical properties of bone and typical metallic and ceramic biomaterials[12] (as detailed by Ramakrishna et al.[13]).

	Modulus (GPa)	Tensile Strength (MPa)
Cortical bone		
(longitudinal)	17.7	133
(transverse)	12.8	52
Cancellous bone	0.4	7.4
Metal Alloys		
Stainless steel alloy	190	586
Co-Cr alloy	210	1085
Titanium alloy	116	965
Amalgam	30	58
Ceramics		
Alumina	380	300
Zirconia	220	820
Bioglass	35	42
Hydroxyapatite	95	50

Table 1.2. Mechanical properties of typical bioresorbable polymers[14].

	Modulus (GPa)	Tensile Strength (MPa)
PLA		
poly (lactide)	1.2 – 3.0	25 – 50
PLLA		
poly($_L$-lactide)	3 – 4	11 – 72
PGA		
poly(glycolide)	6 – 7	57
PCL		
polycaprolactone		19 – 21

The *research objective* of this dissertation is to elicit the time-dependent properties of a bioresorbable material system at the material scale and incorporate these properties into computational models to design and predict the material response at the device scale. The primary aim of this study is to quantify the degradation rate of a bioresorbable material system, then use this degradation rate to determine the material response of an orthopedic device made of the same material as healing progresses. In pursuit of this goal, several research aspects are accomplished:

- Development of a processing technique to infiltrate carbon foam with a hydroxyapatite/poly($_{D,L}$-lactide)-co-poly(glycolide) (HA/PDLGA) system
- Characterization of as processed material system including morphological studies and short-term cell study
- Development of test matrix to examine degradation characteristics such as water uptake, mass loss, and dissolution rate of HA/PDLGA/Carbon foam specimens
- Development of computational models simulating the carbon foam microstructure to determine the influence on the change of effective stiffness, effective strength, and load paths when infiltrated with HA/PDLGA
- Sizing and assessment of an internal fixation plate composed of HA/PDLGA/Carbon foam when attached to a transversely fractured femur.

1.2 Background

1.2.1 Bioresorbable Polymers and Characterization Thereof

Since one of the first reported uses of synthetic bioresorbable polymers in surgical applications in 1966[1], poly(lactide) (PLA) remains among the two most widely investigated bioresorbable systems along with poly(glycolide)[15]. Among other investigated systems are polycaprolactone (PCL), poly(dioxanone) (PDS), poly(trimethylene carbonate) (PTMC), and poly(3-hydroxybutyrate) (PHB). Although this list is not exhaustive by any means, there are detailed reviews on bioresorbable materials in the biomaterial literature[16, 17]. As such, only PGA and PLA will be discussed here for the sake of brevity.

PGA has a highly crystalline structure, for which the structural formula is shown below in Figure 1.2a. PGA has a reported modulus of up to 6-7 GPa and strength of 60-100 MPa[18]; however, it should be recognized that the mechanical properties are highly dependent on the molecular weight, degree of crystallinity, and processing methods which influence polymer chain orientation. PGA is more hydrophobic when compared to PLA, leading to increased hydrolysis rates and shorter material lifetime (PGA sutures typically lose mechanical strength 2 to 4 weeks after implantation[2]). The rapid degradation of PGA results in an accumulation of the glycolic acid by-product because there is less time for the glycolic acid to enter the body's metabolic cycle. This acidic build-up often times leads to adverse tissue reactions and inflammations[18].

PLA exists in four morphologically distinct polymers because it has two steroisomeric forms: the stereoregular forms are D-PLA and L-PLA (both semi-

crystalline); and the racemic form is D,L-PLA (amorphous)[2]. PLA has a reported modulus of up to 3-4 GPA and strength of 50-70 MPa, but again these properties are dependent on the molecular weight, crystallinity, and polymer processing[18]. When compared to PGA, PLA is more hydrophobic because of an additional methyl group in the chemical structure (shown in Figure 1.2b), resulting in slower degradation rates where complete mass loss is reported to be on the order of years[18].

In addition, copolymers of PGA and PLA have been used to tailor the modulus, strength, and degradation rates of the resulting copolymer. There is not, however, a linear relationship between the physicomechanical properties of the copolymer and the corresponding ratio of PGA and PLA present in the system[2].

a) 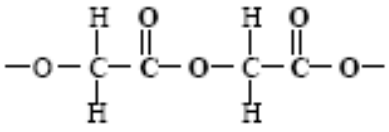 b) 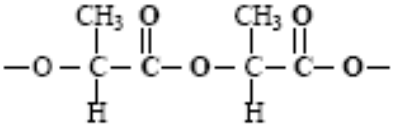

Figure 1.2. Chemical structures of a) PGA and b) PLA.

PGA and PLA both degrade through a hydrolytic process, where water uptake results in hydrolytic scission of the ester bonds in the polymer chains[14]. Here, chain-scission continues until the monomer (lactic acid or glycolic acid) enters the tricarboxylic acid cycle and is broken down to eventually leave the body as water and carbon dioxide[14]. The dominant factors that affect material *degradation rates* include: the functional group in the monomer, polymer chain endgroups, molecular weight, and crystallinity[9, 19]. These molecular parameters influence the diffusivity of water into the material, as well as the rate at which the polymer chain hydrolyzes. In addition to these factors, geometry of the material plays an important role as to the *degradation mode* of the material[20]. Here, if the diffusion rate is higher than the rate at which the polymer hydrolyzes, degradation of the polymer occurs throughout the volume of the material; this degradation mode is classified as bulk erosion. On the other hand, the surface erosion mode occurs if the diffusion rate is lower than the hydrolyzation rate, where degradation is limited to the surface of the material.

A combination of material and mechanical techniques are used to characterize the effects of degradation on bioresorbable polymers. To simulate the effects of implantation, *in vitro* degradation testing of the bioresorbable composite materials is performed by incubation of specimens in a simulated physiological environment[21]. Specimens are then removed at periodic intervals and tested to determine degradation characteristics as well as material and mechanical properties. Among the parameters of interest in determining degradation mechanisms and rates are changes in specimen mass, molecular weight, bulk and surface morphology, chemical composition, and changes in

specimen stiffness and strength[22]. The techniques that are often employed to study these parameters are transmission electron microscopy (TEM), scanning electron microscopy (SEM) and optical microscopy (OM) to analyze morphology and degradation modes, gel permeation chromatography (GPC) to measure polymer molecular weight, and differential scanning calorimetry (DSC) to measure glass-transition temperature and melting temperature as well as changes in crystallinity. Degradation rates are often quantitavitely characterized via mass loss analyses, where specimen mass at specified degradation times are compared to initial mass. In addition, mechanical tests are performed to determine specimen stiffness and strength at specified degradation times. Among the tests conducted are tensile and compression tests, flexure tests, and fatigue tests.

1.2.2 Composite Bioresorbable Systems

In efforts to increase the mechanical properties of bioresorbable systems, composite systems have been investigated where reinforcement is typically in fiber or particulate form. There are several in-depth reviews of bioreserobable composite systems[13, 18, 23], so a brief overview is given here.

Bioactive ceramic materials, namely, bioglass and hydroxyapatite (HA), have been the focus of much research for reinforcement of bioresorbable polymers[13, 18]. The advantages of utilizing bioactive materials include improved osteoconductivity and bone-bonding properties, enhanced biocompatibility, minimization of foreign body reactions due to buffering effects of resorption of the materials, and delayed degradation of the bioresorbable matrix[18]. Both bioglass and HA exhibit relatively high modulus

and tensile strength, as shown in Table 1.1, when compared to those values of the bioresorbable polymer matrix.

In addition to bioactive materials, self-reinforced bioresorbable composites have been investigated. In these material systems, fibers are made from the bioresorbable material and used to reinforce the bulk matrix. Using solution-spinning, for example, has resulted in PLLA fibers with initial tensile modulus of 9.6 – 16 GPa and tensile strength of 560 – 2300 MPa[18]. The biggest drawback for self-reinforced composites, however, is the lack of wettability of resorbable fibers. Though the alternate manufacturing processes result in higher mechanical properties of the polymer through alignment of the polymer chains, the thermal properties are still the same. Since the glass-transition temperatures and melting temperatures of the fibers and matrix are similar, it is difficult to achieve sufficient interfacial bonding.

One area of focus for research in reinforced bioresorbable polymers has been tissue engineering applications. Most of this work focuses on reinforced scaffolds, which allow an avenue for tissue growth as the scaffold degrades. Because of the three-dimensional networked structure of these porous scaffolds, these materials typically have relatively low stiffness, thus the need for reinforcement. Numerous studies have been undertaken to determine the effects of scaffold reinforcement with bioglass or HA. For example, Zhang et al.[24] showed that particulate bioglass reinforcement of porous PLLA resulted in an increase of tensile stiffness. Tensile tests showed that an increase in glass content increased the elastic modulus from 107 MPa for a neat PLLA scaffold to 145 MPa and 178 MPA for bioglass/PLLA scaffolds with 0.09 and 0.29 bioglass volume

fractions (v_f), respectively. They also showed that silane pretreatment of the glass resulted in enhancing the increase of modulus as glass content increased while preventing the decrease in tensile strength of the composite often seen with small v_f of particulate reinforced scaffolds. Bleach et al.[25] showed that both strength and failure strain decreases as a result in increased biophasic calcium phosphate (BCP) content suspended in a PLA matrix. Ultimate tensile strength of the neat scaffold was approximately 57 MPa compared to 50 MPa for BCP v_f of 0.05, 30 MPa for v_f of 0.15, and 27 MPa for v_f of 0.25. In addition, the unfilled polymer had a failure strain of 17% whereas for 0.05 v_f of BCP failure strain was approximately 7%, gradually decreasing to 5% as volume fraction increased to 0.25. However, Boccaccini and Maquet[26] showed that compressive strength is increased at high volume fractions of bioglass particulates in foam-like structures of poly(lactide-co-glycolide) (PLGA). In their work, a 50 wt% bioglass/PLGA foam resulted in compressive strength of 22 MPa as compared to 7 MPa for neat PLGA foam. Furthermore, addition of bioglass resulted in a retarded polymer degradation rate, as indicated by weight loss and molecular weight measurements. Addition of HA to porous scaffolds also results in increased compressive strength and stiffness as shown by Ramay and Zhang[27]. In addition to these same enhanced mechanical properties, Wei and Ma[28] showed that a 50 wt% nano-HA/PLLA scaffold results in protein adsorption three times that of a neat PLLA scaffold.

Moving more in-line with orthopedic applications, Furukawa et al. performed *in vivo* animal studies on dense PLLA rods reinforced with HA[29]. Two types of composite rods were implanted in the subcutis and in the medullary cavities of rabbits:

PLLA reinforced with 30 wt% uncalcined HA (u-HA/PLLA), and PLLA reinforced with 30 wt% calcined HA (c-HA/PLLA). Initial tensile modulus of 12 GPa was achieved and the bending strength of the composites implanted in the subcutis was maintained at more than 200 MPa at 25 weeks and at 150 MPa at 52 weeks. Additionally, Dauner et al.[30] performed both *in vivo* and *in vitro* testing of PLLA melt-spun fibers, with strength of 800 MPa, embedded in a poly(L/DL-lactide) (PLDLLA) matrix. The 30% fiber volume fraction composite had initial bending modulus of 6 GPa and retained 50% strength after 10 weeks of degradation.

Mini-screws and mini-plates composed of forged raw hydroxyapatite (u-HA) particles embedded in PLLA matrix were evaluated for cranio-, oral and maxillo-facial surgeries and compared to PLLA devices and titanium devices by Shikinami and Okuno[31, 32]. In both the miniscrews (30 wt% u-HA) and miniplates (40 wt% u-HA), initial mechanical properties were equivalent to those of neat PLLA devices, while the titanium devices exhibited properties two to three times greater than those of the polymeric devices. The fatigue resistance of the polymeric devices, however, revealed that after 60 cycles of alternate bendings, the devices retained 70% of their initial strength, whereas titanium devices fully broke after 8 cycles.

Shikinami and Okuno fabricated spinal/cervical interbody fusion cages from a forged composite of raw (neither calcined nor sintered) particulate HA, u-HA/PLLA, with an u-HA 40 wt% fraction[33]. Initial compressive strengths of the three types of cages investigated (open-box, screw, and cylinder) surpassed those of carbon-fiber/polymer composite cages and titanium cages. In addition, fatigue resistance to

compressive loading while submerged in simulated body fluid (SBF) persisted for longer than the minimum period (6 months) necessary for spinal devices.

1.2.3 Computational Analysis

In addition to experimentation, computational modeling has been utilized to predict stiffness and strength of the composites as well as predict device response under simulated loading conditions. In determining effective properties, the present state of the art in modeling in composite biomaterials is largely based on single particles embedded in a matrix which is mostly treated as an elastic system. Most work focuses on reinforcement of non-resorbable polymer matrices, and when resorbable matrices are considered, degraded properties are not incorporated into the models. Below are brief summaries of work in this area as found in the literature. Though most do not involve resorbable matrices, these are included to give an overview of current research.

In the pursuit of evaluating effective material properties, several finite element analysis (FEA) models of a unit cell composed of a single hydroxyapatite (HA) particle embedded in matrix have been undertaken[34-36]. Utilizing linear elastic properties in a three-dimensional FEA model, stress concentrations and stress distributions due to compressive loading of a HA particle embedded in polyethylene matrix is investigated[35]. Similarly using the particle/matrix unit cell, the compressive modulus of HA/PLLA composite is predicted for a range of HA volume fractions based on linear elastic constituent properties. It was found that compressive modulus varies from approximately 7 GPa at 0.24 HA volume fraction to 32 GPa at 0.65 HA volume fraction. In addition, particle roundness is found to have little effect on the stress state[34]. More

recently, a three-phase model of an elastic-brittle HA particle embedded in elasto-plastic matrix (PEEK) with an interface region is created with two-dimensional axisymmetric elements. Incorporating damage evolution to simulate debonding as well as matrix yielding, it is found that as HA volume fraction increases, modulus increases and tensile strength and strain to fracture decrease[36].

In addition to prediction of effective properties, computational models of reinforcement devices have been utilized to predict device performance. Braided carbon/epoxy bone plates (dimensions of standard Dynamic Compression Plate of AO Institute) are modeled utilizing three-dimensional elements and elasto-plastic properties validated with four-point flexure tests[37]. In this study, simulation of bone plate fixed to fractured bone in bending is conducted, incorporating contact surfaces between bone and bone plate. It is found that the resulting strain in bone of composite model is higher than that of a stainless steel plate reinforced bone.

In another separate study, three-dimensional FEA models created of poly(L-lactide-co-DL-lactide) plates and screws reinforcing mandibular angle fracture is created[38]. Non-degraded linear elastic material properties are used and stresses and bone interfragmentary displacements resulting from applied bite and muscle forces compared to model incorporating titanium devices. It is found that polymer yield strength is not exceeded and fracture stability is adequately maintained.

1.3 Overview of the Study

In pursuit of the research objective stated in Section 1.1, a bioresorbable material system is created for study of degradation mechanisms and dissolution rates. Here, carbon foam is infiltrated with a HA/PDLGA system. The constituent materials, processing methods, and characterization are described in Section 2. Morphological investigations are undertaken to determine the distribution of HA particles in the PDLGA phase, the presence of defects as a result of infiltration, and the effects of infiltration on the distribution of HA particles in the PDLGA phase. In addition, 24-hour cell studies are performed where rat calvarial osteoblasts are cultured on the material systems created to determine if the processing technique results in a material that elicits an abnormal cell reaction.

Section 3 describes the experimental efforts to characterize the degradation mechanisms and dissolution rate of the HA/PDLGA/Carbon foam (HA/P/C) material system. Here, *in vitro* degradation experiments are performed on thin specimens to determine the water uptake response as well as mass loss characteristics of the material. This data is used to determine the one-dimensional diffusion coefficient as well as dissolution rate of the material.

Section 4 describes the computational models used to predict the mechanical properties of HA/PDLGA and HA/P/C systems. First micromechanics averaging techniques are used to determine the effects of HA particles on the effective elastic modulus of the HA/PDLGA system. Finite element techniques are then employed to

evaluate the effects of carbon foam on the effective stiffness and strength of the HA/P/C system in addition to the change in load paths.

Finally, Section 5 describes the FE model of an internal fixation plate used to stabilize a human femur with a transverse diaphyseal fracture. The elastic stiffness of the HA/P/C as found in Section 4 as well as the dissolution rate determined in Section 3 are used to model the time-dependent properties of the HA/P/C plate. The load applied is a combined axial/moment load equivalent to loads seen from standing. Both the response of the fixation plate and the response of the fracture zone are investigated as healing progresses to ensure the plate is capable of maintaining fracture stability as the plate degrades.

2. MATERIAL PROCESSING AND CHARACTERIZATION

This section details the methods used in processing the material systems of interest and characterizing the reinforced bioresorbable polymer system as processed. As mentioned in the research objectives, the material system of interest is a 50:50 poly($_{D,L}$-lactide)-co-poly(glycolide) (PDLGA) reinforced with hydroxyapatite (HA) and carbon foam. Here, the constituent materials are described and the processing methods developed to create the material systems are detailed. Morphological investigations are performed using optical microscopy, scanning electron microscopy, and energy-dispersive spectroscopy to determine: the distribution of HA particles throughout the PDLGA phase; the presence of defects (voids, cracks, and interfacial debonds) caused by the infiltration process; and the effects of infiltration on the distribution of HA particles in the PDLGA phase. In addition, 24-hour cell studies are performed where rat calvarial osteoblasts are cultured on the material systems created to determine if the processing technique results in a material that elicits an abnormal cell reaction (at least within the first 24 hrs). Additionally, mechanical experiments are performed in an attempt to determine the initial (undegraded) mechanical properties of the material systems; those experiments and results are described.

The HA, PDLGA, and carbon foam systems used in this research are described in Section 2.1. Here, reasoning for the selection of the constituent materials is given in addition to the manufacturer's reported properties for the materials. The structure of the HA particles and the carbon foam as received is investigated and detailed as well. The processing techniques developed to create the material systems are then described in

Section 2.2. Here, the solution mixing technique is presented, where HA is distributed in a PDLGA/solvent solution and then the solvent is evaporated to form a HA/PDLGA film. The melt casting technique is then described in which the carbon foam is infiltrated by first cutting foam specimens and placing in a mold, and then the polymeric films are melted to infiltrate the foam.

Neat PDLGA, HA/PDLGA, and infiltrated foam specimens are created and characterized, and are described in Sections 2.3, 2.4, and 2.5, respectively. Section 2.3 contains the details of three-point flexure tests performed on PDLGA specimens as well as the details of the cell culture study performed on thin PDLGA specimens. Section 2.4 contains the specifics of the morphological studies of the HA/PDLGA specimens as well as the results of the cell culture study performed on HA/PDLGA specimens. Finally, Section 2.5 contains the characterization details of the PDLGA/Carbon Foam and HA/PDLGA/Carbon Foam specimens created. Here, cell studies are performed on PDLGA/Carbon Foam specimens.

It is noted that although degradation of the material systems can be considered characterization, this aspect of characterization is addressed in Section 3, where an entire section is dedicated to degradation because of the complexity involved.

2.1 Constituent Candidates and Selection

2.1.1 PDLGA

Two widely investigated bioresorbable polymers are poly (lactic acid) (PLA) and poly (glycolic acid) (PGA). Since PLA and PGA and their copolymers are currently the most extensively utilized synthetic bioresorbable polymers in medicine[15], it is desired to use a polymer in this group to avoid potential biocompatibility issues if an unproven bioresorbable polymer is used.

A PLA-PGA copolymer is chosen for this investigation; the system is a 50:50 poly(D,L-lactide)-co-poly(glycolide) (PDLGA) obtained from Lakeshore Biomaterials. This particular system is chosen for two reasons: first, the PDLGA system is amorphous which eliminates the crystallinity parameter in any subsequent processing and degradation experiments; secondly, the degradation time of a 50:50 PDLGA system is reported to be one to two months[9], which is advantageous in designing and performing the degradation experiments described in a later section in this dissertation.

The 50:50 PDLGA has a manufacturer reported inherent viscosity of 0.54 dL/g (~0.5% w/v in chloroform at 30 °C). A thermoplastic, the PDLGA has a reported glass transition temperature of 45-50 °C and a processing temperature of 140-160 °C. Additionally, the manufacturer reports the following mechanical properties for a 50:50 PDLGA: a modulus of 1305 MPa, a yield stress of 58 MPa, a 5.1 % strain at yield, and a 5.2 % strain at break. No information is known on the molecular weight (or inherent viscosity) of the material as tested as well as the processing conditions of the test specimens.

2.1.2 Hydroxyapatite

Hydroxyapatite (HA) has been the focus of much research for reinforcement of bioresorbable polymers. The advantages of utilizing a bioactive material such as HA include improved osteoconductivity and bone-bonding properties of the composite, enhanced biocompatibility, minimization of foreign body reactions due to buffering effects of resorption of the materials, and delayed degradation of the bioresorbable matrix[18].

The hydroxyapatite (calcium phosphate, $Ca_5(OH)(PO_4)_3$) particles used are reported to be approximately 5 μm in diameter and have a reported modulus of 80 GPa (Sigma Aldrich). Shown in Figure 2.1 are images of the HA particles taken with a violet laser confocal microscope (Keyence, VK-9710). The HA particles are received in a powder form, to take the images, the particles are dispersed in dichloromethane (1% wt HA/dichloromethane solution) and mixed using a magnetic stir bar. A drop of the supernatant is then placed on a glass slide and imaged after the solvent evaporates. Here it is seen that the particles are indeed spherical in shape and are approximately 5 μm in diameter.

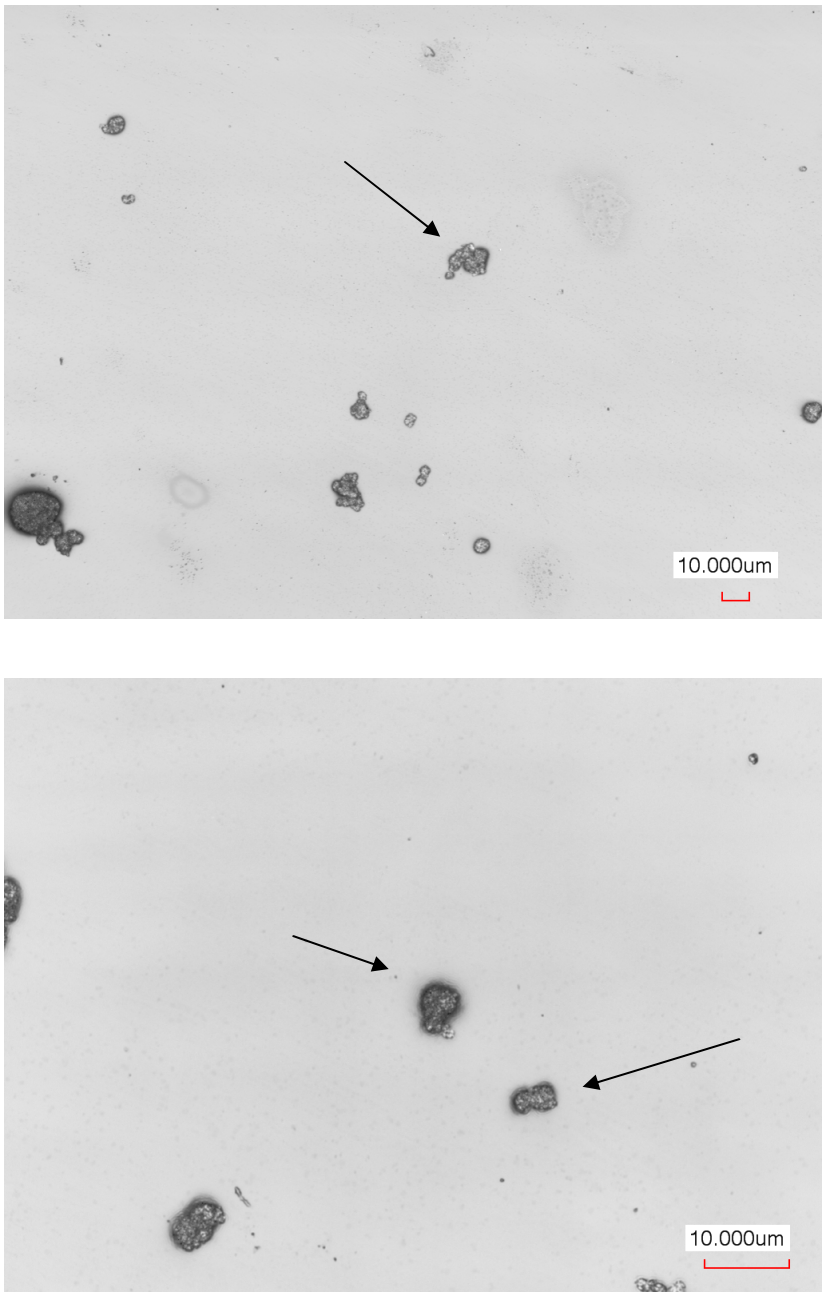

Figure 2.1. Image of representative HA particles as taken with a violet laser confocal microscope (top image 50x, bottom image 150x, 215 nm resolution). Note the larger particles are actually aggregates.

2.1.3 Carbon Foam

The carbon foam used in this study is a reticulated vitreous carbon (RVC) open-cell foam provided by Dr. Khalid Lafdi of the University of Dayton. The bulk density (ρ^*) of the foam is calculated from a block of foam by measuring the dimensions (10.85 x 4.85 x 2.69 cm^3) and mass (6.6155 g) of the block as received. The porosity of the foam is then given by Gibson and Ashby[39] as $\varphi = 1 - \rho^*/\rho_s$ (where ρ_s is the density of solid vitreous carbon, 1.6 g/cc) and is calculated to be 0.971, or 97.1%.

The ligament dimensions are measured using digital images taken with an optical microscope (Olympus SZX16). Twenty-four ligaments are imaged and pictured in Figure 2.2. The ligament lengths are measured using a 0.01 mm calibration slide to measure a distance/pixel and then the number of pixels is measured along the longitudinal axis of each ligament. In addition, the approximate thickness of each ligament is measured at the mid-span and quarter points along the length to calculate an average value for each ligament.

The average length of the ligaments is calculated to be 887 μm with a standard deviation of 385 μm and the average thickness is 265 μm with a standard deviation of 39 μm. As can be seen from the images in Figure 2.2, the pore shapes are inconsistently shaped, comprised of short, medium and long ligaments, thus explaining the large standard deviation in the length measurements. Comparatively, the ligament thicknesses are relatively similar regardless of the length.

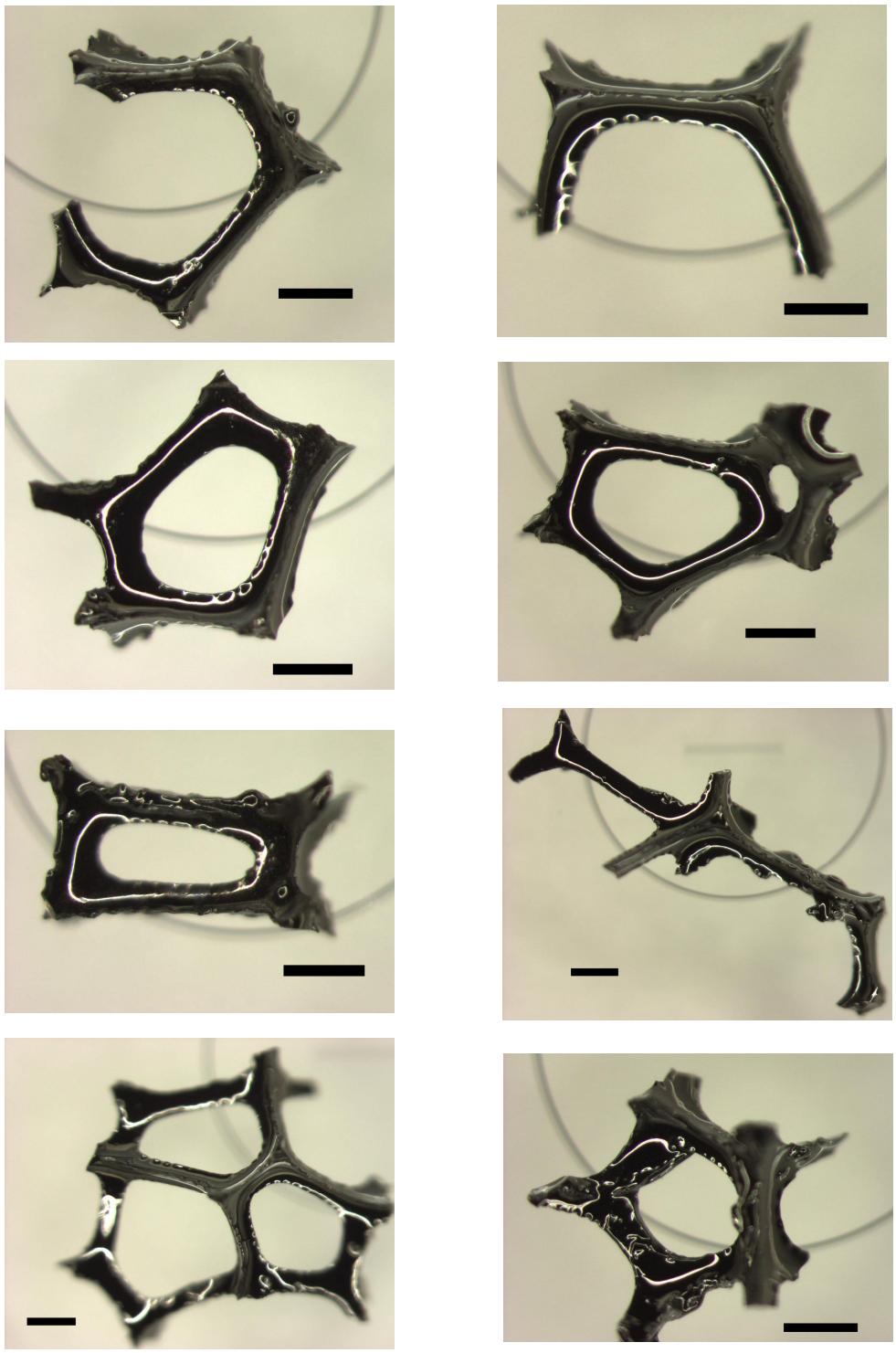

Figure 2.2. Images of individual carbon foam ligaments (all microbars are 500 μm).

Although it cannot be immediately distinguished from the images in Figure 2.2, the cross-section of the ligaments are plateau-shaped, characterized as a hypocycloid with three cusps. The ligament cross-section shape is a result of the processing method used to create the carbon foam[40-42], the details of which are not addressed here. An image of a typical ligament cross-section is presented in Figure 2.3.

It is of interest to determine the curvature of each side of the ligament cross-section. For a typical 3-cusp hypocycloid as shown in Figure 2.4, the total area can be calculated as $2/9\ \pi a^2$. In addition, the area can also be calculated as $(\sqrt{3} - \pi/2)r_o^2$. If the dimension t is known, a can be calculated using straightforward geometry. With a known, r_o can then be calculated using the equivalent area formulas.

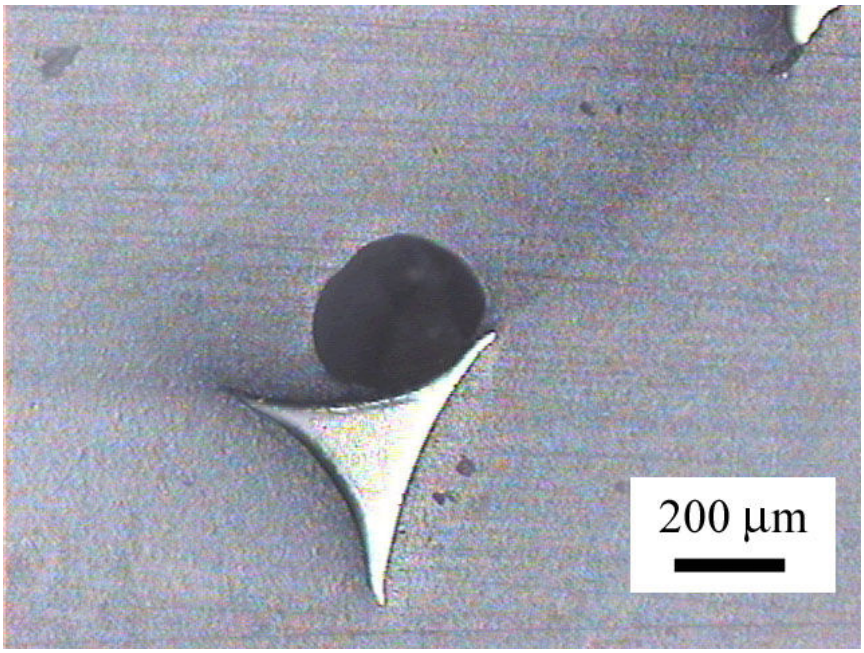

Figure 2.3. Cross-sectional image of a typical carbon foam ligament depicting the characteristic plateau-shape, taken with OM.

Although the average thickness measurement of 265 μm found by OM is not the dimension t in Figure 2.4, that measurement does serve as an upper bound for t. As such, the upper bound of a is calculated to be 153 μm, the area to be 0.01634 mm^2, and r_o to be 318 μm.

To serve as a check for r_o, we can use the following empirical relationship for relative density (ρ^*/ρ_s) and ligament dimensions (r_o and length, l) for an open-cell foam with plateau cross-section[43]:

$$\frac{\rho^*}{\rho} = k\left(\frac{r_o}{l}\right)^n.$$

In this case where the ligament cross-section varies along the length, the constants k and n are 0.1803 and 1.7392, respectively. Using the calculated r_o of 318 μm results in a calculated relative density of 0.0302, which is similar to the value of 0.029 calculated by mass and volume measurements of the bulk foam.

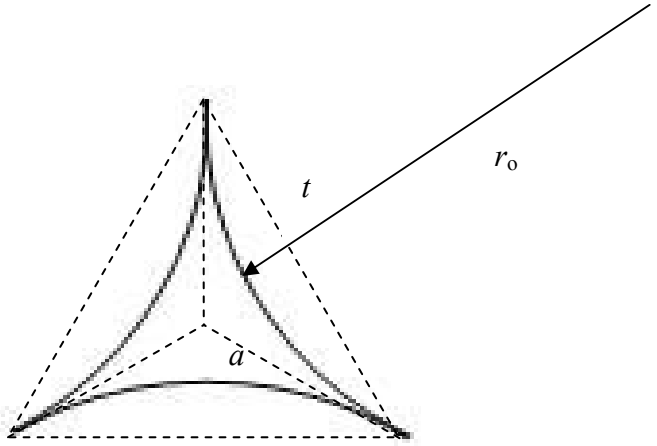

Figure 2.4. Geometry of a 3-cusp hypocycloid.

2.2 Processing

In an effort to create a feasible heterogeneous material system for orthopedic reinforcement devices, HA and carbon foam is used to reinforce the 50:50 PDLGA. Solution mixing is used to disperse the HA reinforcement in PDLGA. Films are cast to evaporate solvent from the solution, and the films are then consolidated into bulk specimens by melt casting the films in an aluminum mold.

2.2.1 Solution Mixing

In the solution mixing process, PDLGA is dissolved with dichloromethane (methylene chloride) and HA is dispersed in the polymer solution using a magnetic stir bar. Based on the densities of PDLGA and HA (1.3 g/cc and 3.1 g/cc, respectively, as provided by manufacturers), each material is added to a 20 ml glass vial in the amounts corresponding to the volume fractions found in Table 2.1. The remainder of the vial is filled with dichloromethane and stirred for 24 hrs. The HA/PDLGA solution is then sonicated for 30 mins to ensure dispersion, to improve interfacial properties, and to remove air bubbles. It should be noted that chloroform solvent was initially used but was abandoned because PDLGA did not dissolve in its entirety in the chloroform.

After mixing, the polymer solution is poured into a 100 mm diameter glass Petri dish, and the solvent is evaporated for 24 hr in a vent hood. The cast film is then placed in a vacuum at room temperature for 12 hr to further facilitate solvent evaporation. It is noted that although neat PDLGA specimens do not need to undergo solution mixing since there is no reinforcement to disperse, this step is still included for sake of consistency.

TABLE 2.1. Amounts of PDLGA, HA, and DCM used for corresponding HA volume fractions.

Volume fraction (v_f)	PDLGA (g)	HA (g)	Solvent (mL)
0	3.25	-	~17.5
15 %	2.7625	1.1625	~17.5
25 %	2.4375	1.9375	~17.5

2.2.2 Melt Casting

Upon evaporation of the solvent, the polymer films are cut into small pieces and melt cast in the aluminum mold to create bulk specimens. The mold, pictured in Figure 2.5, is coated with a mold release agent (Frekote 44-NC, Loctite) using Kimwipes and placed in a vent hood for 15 minutes to allow the mold release to dry before the next coat is applied. When the final of four coats is applied, the mold is placed in a convection oven at 150 °C for 15 minutes for final curing of the mold release agent.

For processing of bulk PDLGA and HA/PDLGA samples, the mold is heated to 200 °C in a convection oven (Blue M, Stabil-Therm) and the pieces of PDLGA film are placed in the mold and melted for approximately 30 minutes. Although no thermogravimetric analysis (TGA) is performed on this particular polymer system to ensure the processing temperature does not result in thermal degradation, there does exist some data in the literature. Sivalingam and Madras[44] studied thermal degradation of poly($_{D,L}$-lactide) (PDLA) and poly(glycolide) (PGA) using TGA under isothermal holding. Presented in Figure 2.6 are plots of the polymer mass variation over

time for several holding temperatures. As can be seen, about 96% of the initial mass of PDLA is retained after 40 minutes at 180 ^{o}C, and about 96% of the initial mass of PGA is retained after 40 minutes at 260 ^{o}C. No isothermal data is presented for a 50:50 PDLGA co-polymer, however D'Antone et al.[45] present non-isothermal TGA data for a PDLA system and a 50:50 PDLGA system. Here, polymer mass is measured as the sample is heated from room temperature to 650 ^{o}C at 20 ^{o}C/min in an air atmosphere. Although this non-isothermal study cannot be directly applied to our isothermal processing technique, it is useful in providing a relative comparison of the thermal stability[46] of PDLA and PDLGA. The temperature at the inflection point (T_i) of the TGA trace of the PDLA studied is reported to be 350 ^{o}C and the T_i of the 50:50 PDLGA is reported to be 375 ^{o}C. Thus the co-polymerization of PGA with PDLA results in increased thermal stability when compared to that of PDLA. With this in mind and the isothermal data presented in Figure 2.6, it is believed that processing the 50:50 PDLGA at 190 ^{o}C for 30 minutes should not result in detrimental thermal degradation.

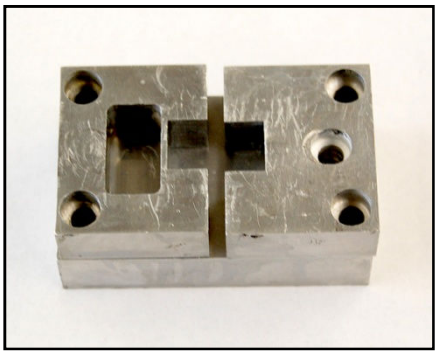

Figure 2.5. Aluminum mold with cavity dimensions of 16mm x 10mm x 10mm.

It should be noted that after 30 minutes in the convection oven, the mold is removed and the sample is cooled at room temperature to avoid prolonged time at elevated temperature. After cool-down, the mold is then heated to ~40 ^{o}C (near T_g) for two hours to reduce any residual stress arising from the previous rapid cool-down.

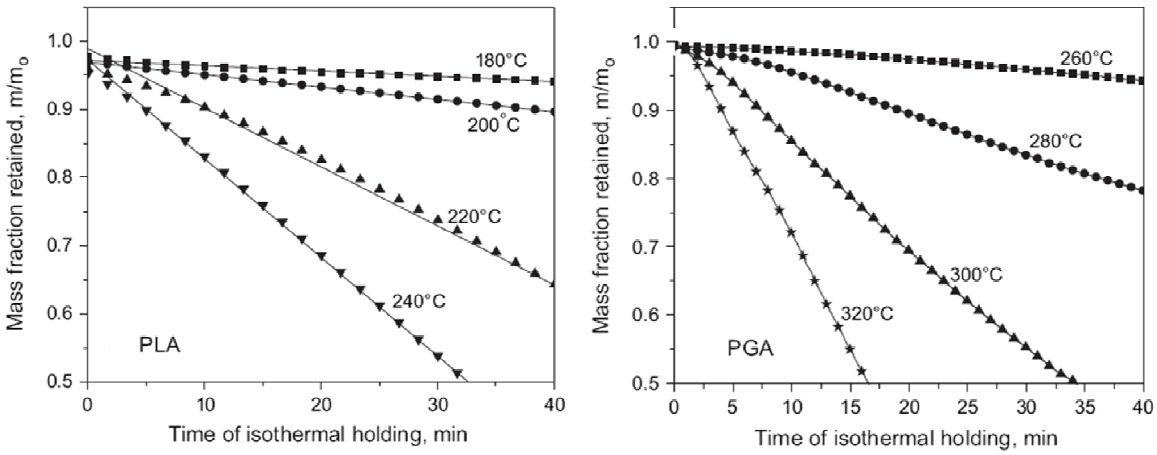

Figure 2.6. Polymer mass variation of PDLA and PGA under isothermal holding [44].

The viscosity of the PDLGA film at 190 °C is such that the polymer flows easily and conforms to the shape of the mold. The HA/PDLGA film, however, is more viscous at 200 °C because of the addition of the HA particles, which requires that the melt be pressed into the mold. This is achieved by manually pressing the melt into the mold using an aluminum bar with a 15.75 mm x 9.75 mm cross-section.

To create PDLGA/Carbon foam specimens, carbon foam is cut to approximate size of the mold using a band saw, rinsed with acetone, and placed in the mold. The PDLGA film is then placed on the carbon foam, heated to 190 °C in a vacuum oven (NAPCO, Model 5051), and the chamber is evacuated until a vacuum of 30 mm Hg is reached. The vacuum is then released to 5 mm Hg, held for 5 minutes, and pulled once again to 30 mm Hg. In this manner of pulling and releasing vacuum several times, the foam is infiltrated with PDLGA. On the other hand, vacuum cannot be used to infiltrated the foam with HA/PDLGA because of the material's high viscosity at 190 °C. Instead, the foam is placed in the mold, the pieces of HA/PDLGA film are placed on top on the foam, heated to 190 °C, and pressed into the foam to create the HA/PDLGA/Carbon foam specimens.

2.3 Neat PDLGA Specimens

Neat PDLGA specimens are created to characterize the mechanical properties of the PDLGA material as well as determine if creating polymer solutions with DCM elicits any negative reactions of rat bone cells in a 24-hour cell culture study.

Three-point flexure tests are performed on five PDLGA specimens, which are created by melt-casting the PDLGA pellets into a glass mold to create a plate. Specimens are then cut from the plate and tested at room temperature.

Biocompatibility studies are performed on thin PDLGA specimens that are cut from the bulk specimens created using the mold pictured in Figure 2.5. The PDLGA is first mixed with solvent (DCM) and then poured in a petri dish to create a polymer film after the solvent evaporates. The film is then melted in the mold to form the bulk specimen. Although the polymer pellets could be directly melted into the mold without addition of solvent, it is of interest to determine if processing PDLGA with solvent elicits any negative reactions of rat calvarial osteoblasts.

2.3.1 Mechanical Characterization via Three-point Flexure Tests

2.3.1.1 Specimen Preparation

PDLGA specimens are made by first melting PDLGA into a glass mold such as the one pictured in Figure 2.7. The mold is made by clamping 2 mm spacer bars between two glass plates that have been coated with a mold release agent (Frekote 44-NC). A silicone tube serves as a seal to ensure the polymer melt does not leak. The PDLGA pellets are added to the preheated mold (190 °C) and the mold/polymer is then returned to the oven in an upright position for an additional 30 minutes. The mold is

then removed and cooled to room temperature at which point the mold/polymer is then heated to ~40 ^{o}C for two hours to anneal any residual stress arising from the rapid cool-down.

Five PDLGA specimens are cut from the plate and the edges polished before testing; a typical specimen is pictured in Figure 2.8. The average cross-sectional dimensions of the five specimens are 5.97 mm (0.24) x 1.88 mm (0.07), as measured with a digital micrometer (value in parenthesis is one standard deviation). The length of all specimens is approximately 25 mm.

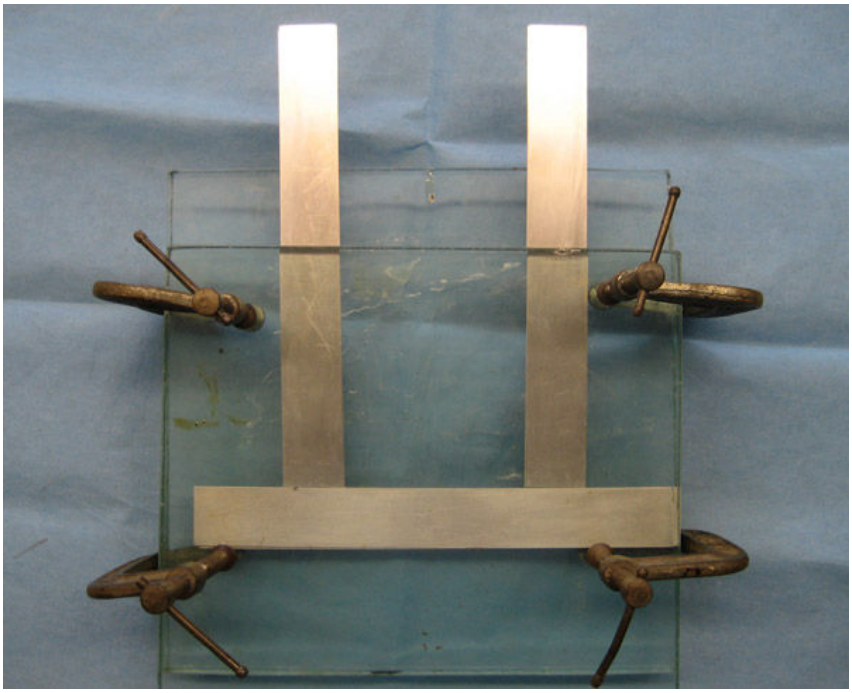

Figure 2.7. Picture of glass mold used to create PDLGA plate.

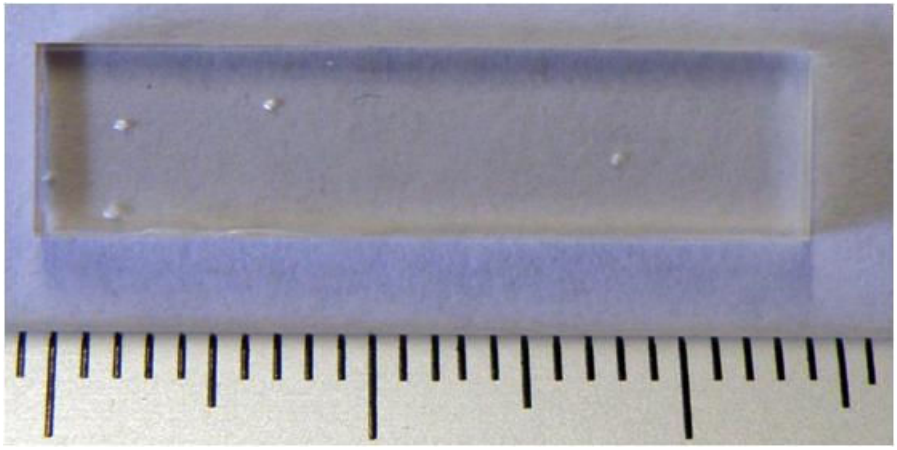

Figure 2.8. Photograph of a typical PDLGA specimen used in three-point flexure test. Note the voids as a result of processing (scale is mm).

2.3.1.2 Three-point Flexure Test

Pictured in Figure 2.9 is the Fullam tensile stage used to perform the three-point flexure test per ASTM D 790-03[47]. The testing stage comes equipped with a 1000 lb (4400 N) load cell and a LVDT to measure crosshead displacement. The fixtures used in this experiment have a support span of 17.0 mm while the loading nose is located at the mid-point of the support span. Per the standards, the modulus E of the specimens is calculated as

$$E = \frac{L^3 m}{4bd^3} \quad \textbf{(2.1)}$$

where L, b, and d are support span, width of beam, and depth of beam, respectively, and where m is the initial slope of the load-deflection curve. In addition, the stress in the outer fiber at the specimen midpoint (σ_f) is calculated as

$$\sigma_f = \frac{3PL}{2bd^2} \tag{2.2}$$

where P is the load at a point on the linear portion of the load-deflection curve. The strain in the outer fiber at the specimen midpoint (ε_f) is calculated as

$$\epsilon_f = \frac{6Dd}{L^2} \tag{2.3}$$

where D is the displacement within the linear range.

The testing is performed under stroke-controlled conditions with a load rate of 0.025 mm/s (1.5 mm/min). Based on the dimensions of the specimens, this load rate results in a strain rate at the outer fiber of 0.06 mm/mm/min, calculated using

$$Z = \frac{6dR}{L^2} \tag{2.4}$$

where Z is the strain rate at the outer fiber and R is the rate of crosshead displacement. Although the standards call for a Z value of 0.01 mm/mm/min, it is recognized that this faster strain rate may result in a more stiff material response if the PDLGA is strain-rate dependent.

In addition, it must be noted that while the standards dictate a support span to specimen depth ratio of 16, the ratio for the specimens as tested is approximately 9 (17 mm / 1.88 mm). Because of this, the relationship in Equation 2.1 may underestimate the modulus since shear deflections are neglected in the formulation.

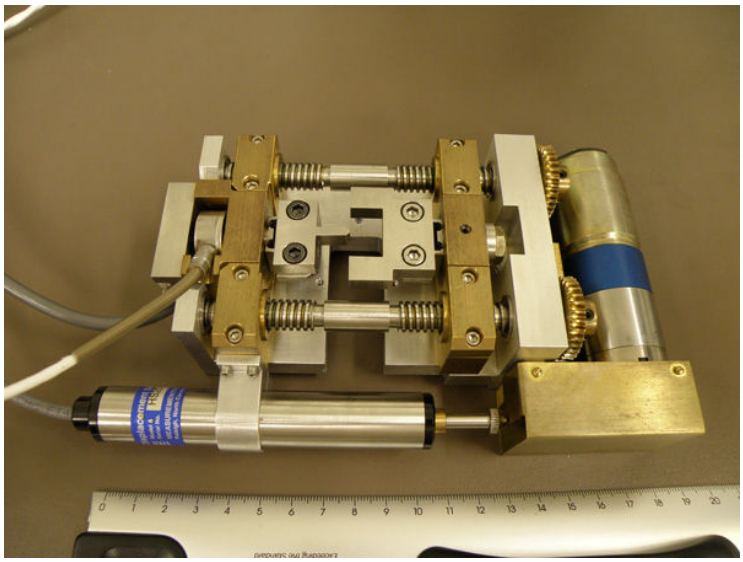

Figure 2.9. Photograph of the test stage used in the three-point flexure tests.

2.3.1.3 Results and Discussion

The load-deflection curves for all specimens are given in Figure 2.10. The curves of all specimens are considered to be linear throughout the loading range until failure, where the specimens fractured and the load dropped immediately. The slope *m* of each curve is found and modulus *E* of each specimen is then calculated according to Equation 2.1 and given in Table 2.2. Also given in the table are the strengths and failure strains of the specimens that are calculated using Equations 2.2 and 2.3, where the loads and displacements at failure are used.

Though there are voids present in the test specimens, the average modulus is found to be 1568 MPa (219 Std Dev), whereas the manufacturer reports a modulus of 1305 MPa. Even though there is a relatively large standard deviation of the experimental

values (14%), the lowest specimen value of 1328 MPa is still slightly higher than the reported value. Again it should be noted the molecular weight of the PDLGA reported values are unknown, so this may account for the difference. Although the modulus is found to be higher than the reported value, both the strength of 19 MPa and the strain at failure of 1.2% is lower than the reported values of 58 MPa and 5.1%. This major difference (a factor of 3 for the strength, a factor of 4 for the strain) is attributed to the presence of voids in these test specimens. Although the voids should not impact modulus much because of the low void volume fraction, they will impact the stress and strain at failure because of localized concentrations generated in those areas. Thus, the presence of voids in the specimens explains the low strength and strain at failure values.

Although the load-deflection curves presented in Figure 2.10 are relatively consistent, it must be noted the maximum peak load of all specimens is 18 N. This translates to a load range that is 0.4% of the load cell maximum (4400 N). This being well within the error range of a load cell, the mechanical properties determined in this experiment cannot be reported with confidence. To determine mechanical properties with confidence, further experiments must be performed with either a much smaller load cell (100 N would be ideal), or on a different testing stage with much larger specimens. Since limited materials were available for these experiments, no further mechanical experiments of the PDLGA were undertaken. Because of the lack of confidence in the above experimental values, it is deemed that the manufacturer's reported values will be used in future mechanical analyses.

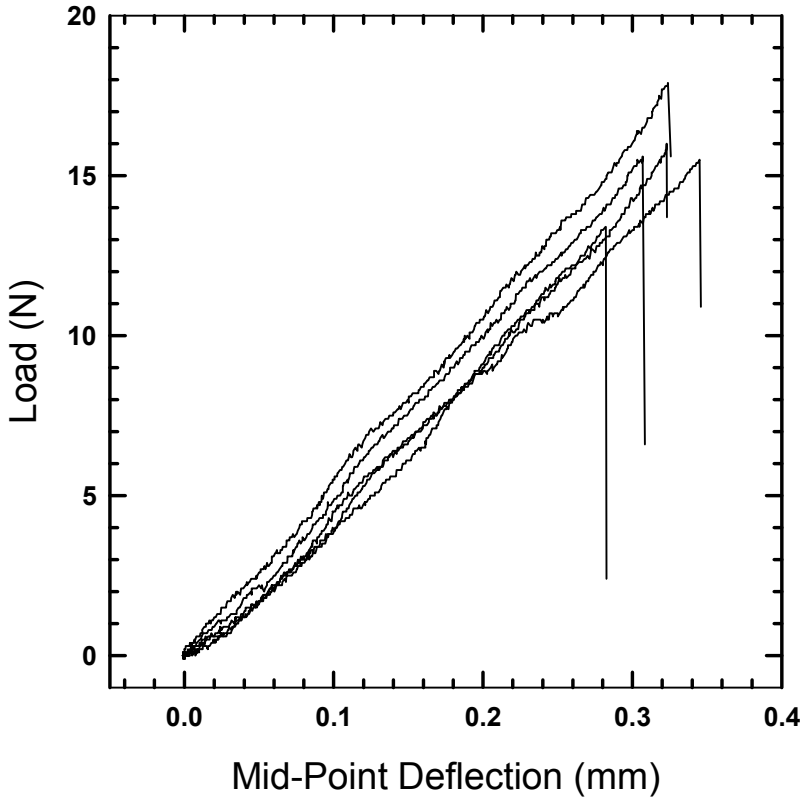

Figure 2.10. Load-deflection curves of the five specimens tested in three-point flexure.

Table 2.2. Load-deflection slope, modulus, strength and strain at failure values.

Specimen	Slope, *m* (N/mm)	*E* (MPa)	Strength (MPa)	Strain at Failure (mm/mm)
1	47.09	1448	18.5	0.0133
2	51.58	1569	18.6	0.0120
3	48.89	1581	18.6	0.0108
4	52.84	1328	18.7	0.0134
5	51.55	1913	22.4	0.0121
Average		1568	18.9	0.0124
Std Dev		219	2.1	0.0011

2.3.2 Characterization of Biocompatibility

Although there is extensive work in the literature on the biocompatibility of PLLA, PGA, HA, and numerous HA/biopolymer systems [13, 28, 29, 31, 32, 48], it is necessary to ensure that this unique material system of HA/PDLGA/Carbon foam is biocompatible. In an effort to determine biocompatibility of the created material systems, an initial cell study is performed where rat calvarial osteoblast cells (bone-forming cells) are cultured on neat PDLGA, HA/PDLGA, and PDLGA/Carbon foam specimens for 24 hrs. Because the intended applications of these material systems are in orthopedics, it is important to determine osteoblast activity/reactivity to the materials. Here, the experimental procedure and results are presented for a 24 hr osteoblast study of PDLGA specimens, as processed under the conditions presented in Section 2.2.

2.3.2.1 Specimen Preparation

Biocompatibility studies are performed on thin PDLGA specimens that are cut from the bulk specimens created using the mold pictured in Figure 2.5. The PDLGA is first mixed with solvent (DCM) and then poured in a petri dish to create a polymer film

after the solvent evaporates. The film is then melted in the mold to form the bulk specimen. Again, although the polymer pellets could be directly melted into the mold without addition of solvent, it is of interest to determine if processing PDLGA with solvent elicits any negative reactions of rat calvarial osteoblasts.

After the PDLGA bulk samples are made, cross-sections approximately 1 mm in thickness are cut using a wet-diamond saw and then polished. The resulting specimens for the cell study are 10 mm x 8 mm x 1 mm in dimension. Immediately prior to the cell study, the specimens are UV sterilized for 1 hr.

2.3.2.2 24-hour Osteoblast Cell Culture

It is of interest to determine if the processing of PDLGA with solvents elicits any negative reaction of osteoblasts that are cultured on the processed PDLGA. In this effort, osteoblasts are cultured on the PDLGA specimens for 24 hrs where it is investigated if the cells attached to the surface. If cells do attach to the material, it is deemed the material processing with solvents does not introduce bioincompatibilities.

After the PDLGA specimens are created and sterilized, they are placed in a 24-well cell-culture plate and teflon rings are inserted to ensure the specimens remain on the bottom surface of the well. Working in a sterilized bio-hood, approximately 1 ml of cell culture media (DMEM, 10% fetal bovine serum, Sigma Aldrich) is added with various antibiotics not detailed here and 10,000 cells/cm^2 of rat calvarial osteoblasts (Dominion Pharmakine) are added to each well [49]. The well plate is then placed in an incubator (Heraeus Hemacell 250) at 37 °C, 5% CO_2, and 95% humidity. After 3 hrs, the well plate is removed, specimens are briefly examined using an optical microscope (Zeiss Axiovert), and the well plate is returned to the incubator. After 24 hrs, the specimens are again imaged *in situ* and the cell study is subsequently ended.

2.3.2.3 Results

Typical OM images of the surfaces of the PDLGA specimens after 3 hrs and 24 hrs of cell-culture are shown in Figure 2.11. As can be seen, the osteoblasts are attached to the surface of the PDLGA, indicating that the cells are alive after 3 hrs of incubation. In addition, some of the cells in Figure 2.11a appear to be larger than the surrounding cells. These are cells that are attached to the surface and beginning to spread/flatten, thus the larger appearance in a two-dimensional image.

The image after 24 hrs of culture again shows cells that are attached and spreading. Additionally, it appears that some osteoblasts are beginning to spread into a finger-like morphology, which is behavior of a normal phenotype. The images at 24 hrs are low in quality compared to the 3 hr images, most likely because the absorption of water by the PDLGA material interferes with imaging process.

Here, the osteoblasts are observed to be attached to the PDLGA surface and are spreading into a finger-like structure. Since the osteoblasts observed in all cultures displayed behavior of a normal phenotype, the PDLGA as processed does not inhibit cell attachment and spreading.

2.4 HA/PDLGA System

Before the carbon foam is infiltrated with the HA/PDLGA system, PDLGA must first be loaded with HA. This section describes the results of the films created using the solution mixing technique described in Section 2.2.1 to create the HA/PDLGA system. In addition, the morphology of bulk HA/PDLGA specimens created using the melt

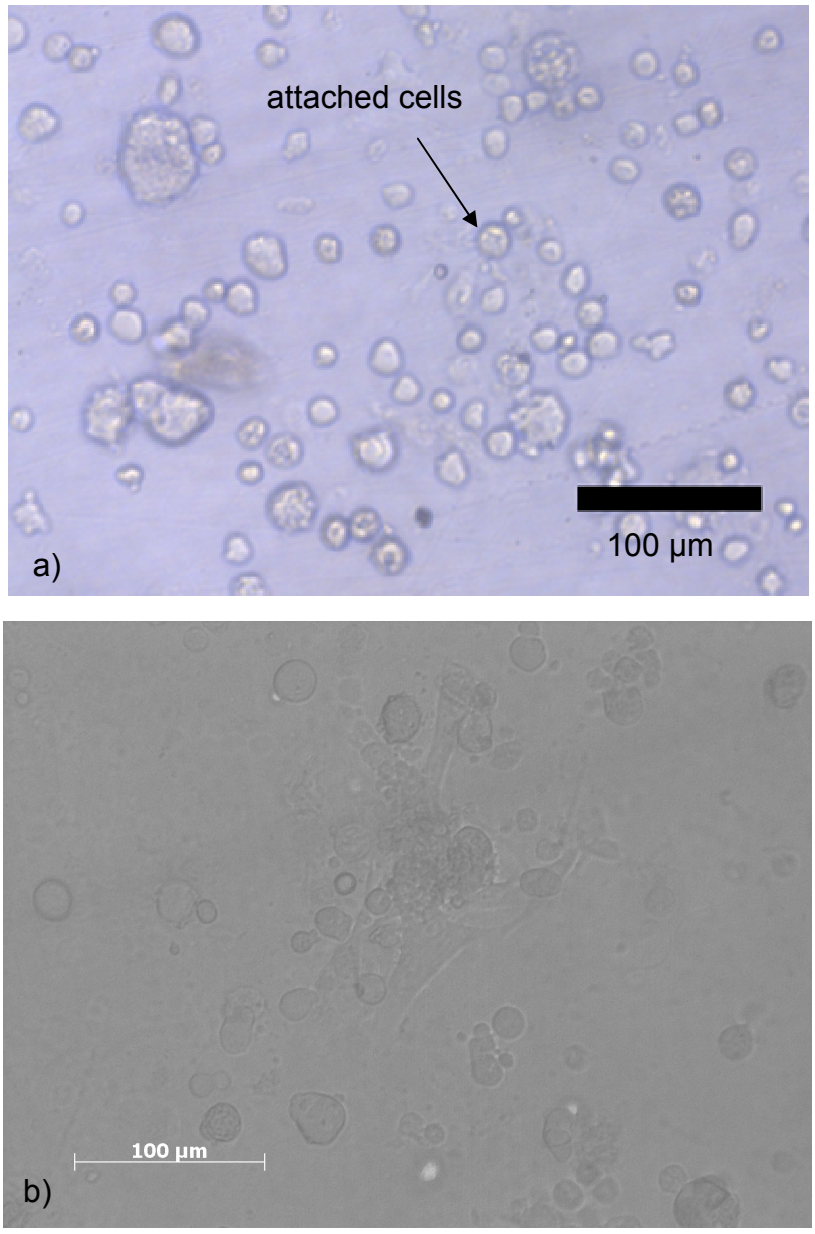

Figure 2.11. OM images of rat calvarial osteoblasts attached to PDLGA specimens after a) 3 hrs and b) 24 hrs of cell culture. What appears to be larger cells are actually the cells beginning to spread/flatten once attached to the surface.

casting technique described in Section 2.2.2 is investigated to get a baseline to compare HA/PDLGA/Carbon foam specimens as processed. Furthermore, a 24-hr cell study is conducted on the HA/PDLGA specimens to determine if the introduction of HA results in a change of cell response observed from the PDLGA study.

2.4.1 Sample Preparation

Using the process described in Section 2.2.1, HA/PDLGA polymer solutions are made with HA volume fractions of 0%, 15%, and 25%, and are then cast to create films about 0.5 mm thick, as pictured in Figure 2.12. Although the neat polymer is transparent, the addition of HA to PDLGA results in opaque materials.

As previously noted when melt casting the films, the viscosity of the PDLGA film at 190 °C is such that the polymer flows easily and conforms to the shape of the mold. The HA/PDLGA film, however, is more viscous at 190 °C because of the addition of the HA particles, which requires that the melt be pressed into the mold. When melt casting the 15% HA/PDLGA film, pressing the melt did not completely eliminate voids present in the melt (the voids are most likely caused by stacking the pieces of film). An OM image of a bulk sample cross-section is shown in Figure 2.13 where these voids are evident.

When melt casting the 25% HA/PDLGA film, the high particulate content of the material system resulted in large-scale HA consolidated. Because of this consolidation, the bulk specimens resulted in what can best be described as crumbling upon removal from the mold. It is presumed that the high loading content of HA prevented the particles from adequately dispersing throughout the polymer matrix, resulting in

inhomogeneities and thus local areas of weakness. Since processing of the 25% HA/PDLGA bulk specimens was unsuccessful, all future references to HA/PDLGA refers to the 15% v_f HA/PDLGA system.

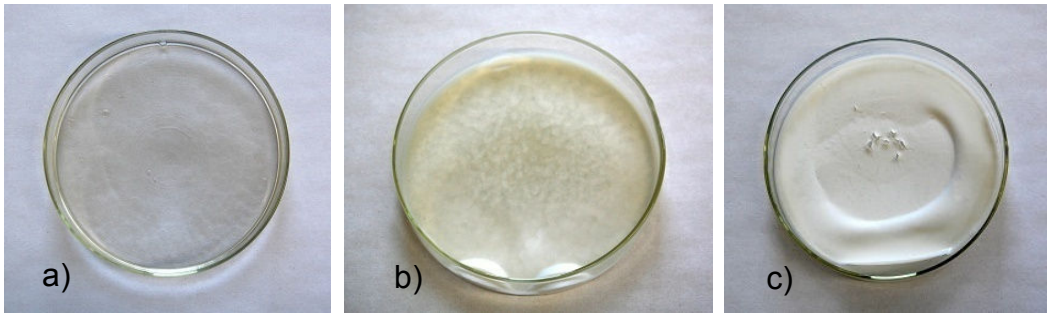

Figure 2.12. Films of a) neat PDLGA, b) 15% v_f HA/PDLGA, and c) 25% v_f HA/PDLGA.

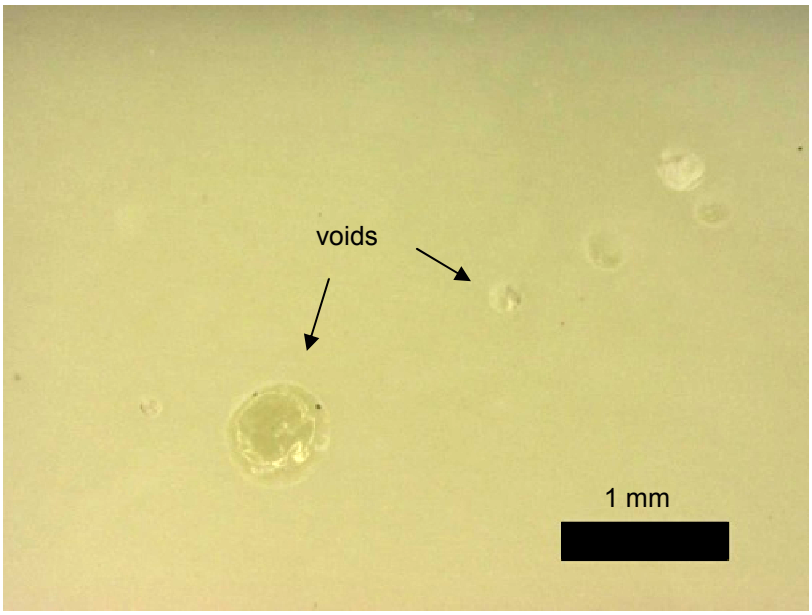

Figure 2.13. OM image of polished surface of bulk HA/PDLGA specimen (15% v_f). Whereas the HA/PDLGA is white in color, the brightness/contrast of the image is adjusted to highlight the voids, resulting in the yellowish hue.

2.4.2 Specimen Morphology

Optical microscopy (OM), scanning electron microscopy (SEM), and energy-dispersive spectroscopy (EDS) are used to characterize the morphology of the HA/PDLGA specimens. The imaging techniques are used to observe the presence of any cracks and voids resulting from processing, as well as to determine the degree of dispersion of HA throughout the PDLGA matrix.

2.4.2.1 Imaging Preparation

OM (Olympus BX60) and SEM (JEOL JSM-6400) are used in this morphological examination. In addition, an EDS (PGT) coupled with the SEM is used to determine the dispersion of HA particles throughout the bulk specimens. Cross-sections as well as fractured surfaces of bulk specimens are examined. Cross-sections with approximate dimensions of 10mm x 8mm x 1mm are cut with a wet-diamond saw and subsequently wet-polished with grades of sandpaper from 500-4000 grit. Alternatively, fractured surfaces are created by immersing specimens in liquid nitrogen and initiating a crack by tapping the specimen with a hammer and a razor blade.

To prepare specimens for SEM, specimens are mounted on stubs, vapor-coated with ruthenium tetroxide, sputter-coated with carbon, and a thin bead of carbon dag (Electrodag 502) is applied around the specimen perimeter to improve electrical conductivity. Ruthenium vapor-coating is achieved by placing the specimen in a vapor chamber and adding 1 ml of 10% (wt/vol) sodium hypochlorite to 0.02 g of ruthenium chloride in a plastic bottle cap in the chamber [50, 51]. After vapor-coating for 10 mins,

a 40 nm thick layer of carbon is sputter-coated on the surface. The carbon dag is then applied around the specimen perimeter and is dried overnight in a desiccator.

2.4.2.2 Results and Discussion

A SEM image of a fractured surface of a HA/PDLGA specimen is shown in Figure 2.14a; a void is captured in this image for reference purposes in the EDS analysis. An EDS mapping of this same region is shown in Figures 2.14b-c, where the presence of calcium and phosphorous elements are identified by green and yellow, respectively. Since calcium and phosphorous are observed to be homogenously distributed throughout the HA/PDLGA phase, it is assumed that the HA particles ($Ca_5(OH)(PO_4)_3$) are also homogenously distributed throughout the polymeric matrix.

It is difficult to identify HA particles in the SEM images solely by visual inspection because of the surface texture of the specimens investigated. In this case, EDS is used to confirm a potential sighting of a HA particle by plotting the elemental peaks in a particular scan. For example, a SEM image of a HA particle approximately 5 μm in diameter in a HA/PDLGA bulk specimen is shown in Figure 2.15a. An EDS plot

of the area surrounding the particle is shown in Figure 2.15b, where carbon, phosphorous, and calcium peaks are easily identified. The source of the carbon peak is attributed to the carbon sputter-coating as well as the carbon present in the PDLGA constituent, whereas the calcium and phosphorous peaks are attributed to the HA particles. When an EDS analysis is performed solely on the HA particle at high magnification, the elemental spectrum in Figure 2.15c is observed. In this plot, it is observed that the carbon peak has a lower intensity when compared to the plot shown in Figure 2.15b. Though there is still carbon present, most likely from the carbon sputter-coating, the relative high intensity of calcium and phosphorous elements confirm that the particle is indeed HA.

Still, the visual identification of HA particles (dispersed or otherwise) in the SEM images is difficult, so it cannot be stated with certainty that the HA particles are well-dispersed in the matrix. The only data that can be relied on is the EDS elemental mapping in Figure 2.14, where no aggregates of calcium or phosphorous are observed, thus leading to the conclusion that the HA particles are well-dispersed.

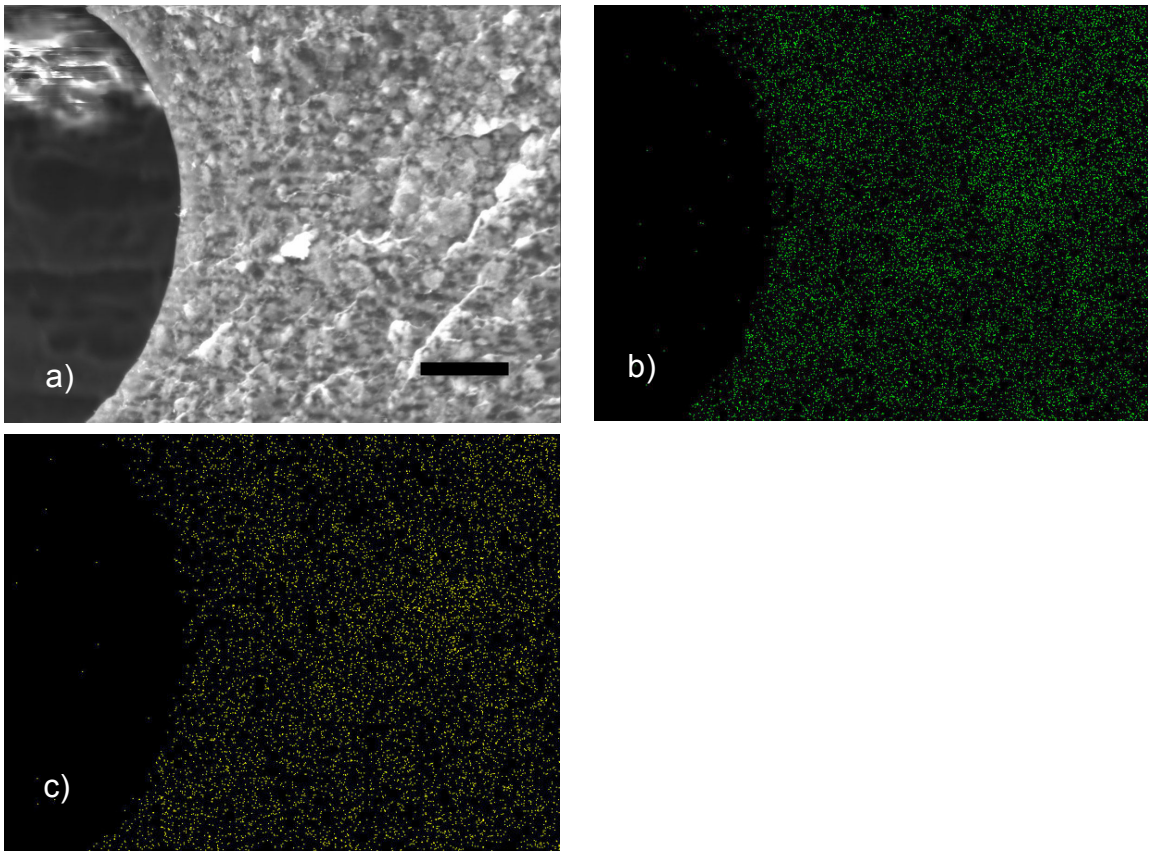

Figure 2.14. a) SEM image of fractured surface of HA/PDLGA specimen and corresponding EDS maps of b) calcium, c) phosphorous. The scale bar represents 20 μm.

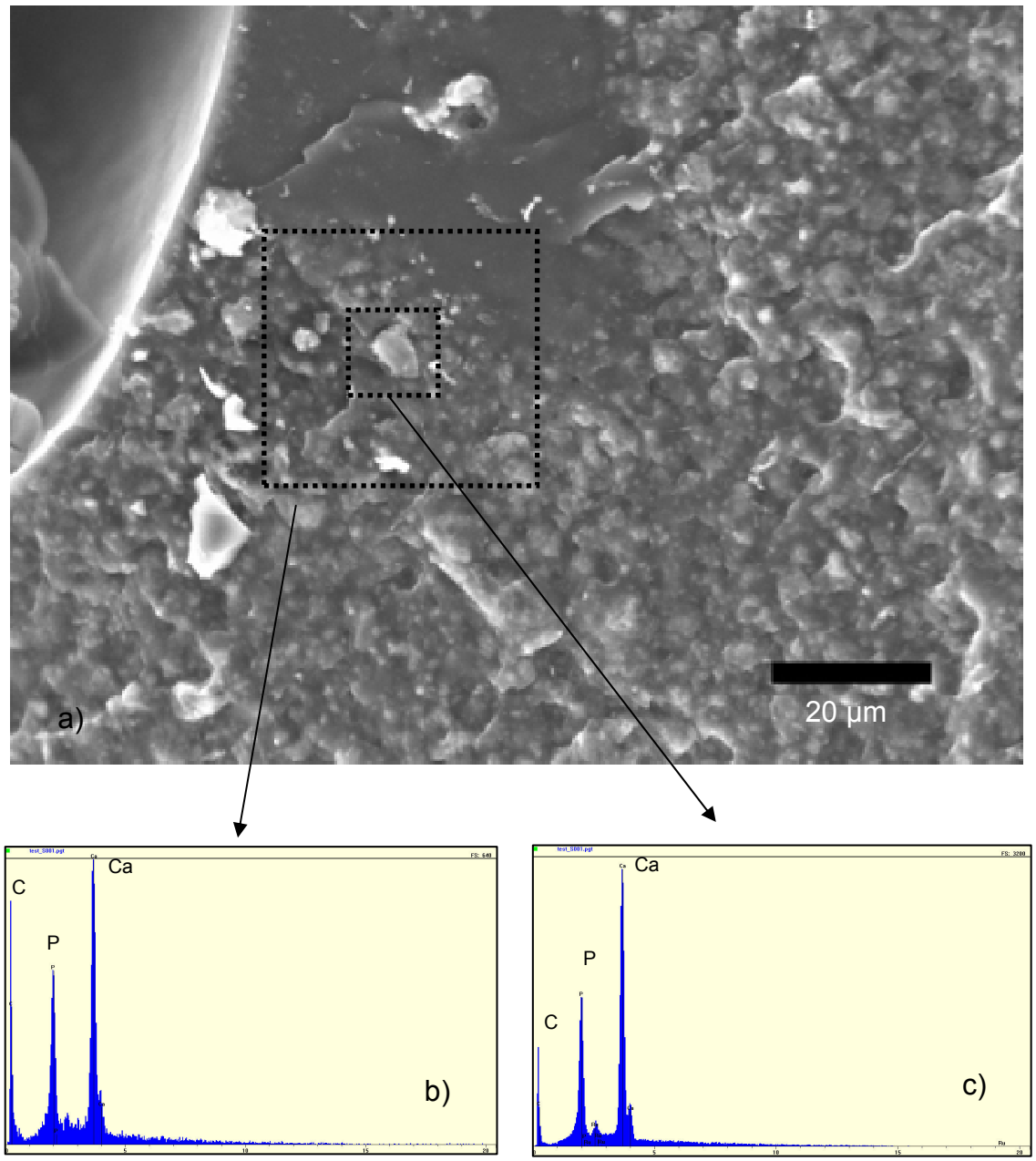

Figure 2.15. SEM image of HA particle in PDLGA and EDS plots of HA/PDLGA.

2.4.3 Characterization of Biocompatibility

A 24-hr cell study similar to that described in Section 2.3.2 is performed on the HA/PDLGA specimens to determine if the introduction of HA results in a change of cell response observed from the PDLGA study. Here, the specimens are HA/PDLGA specimens are prepared in the same manner as the previous study, where the HA/PDLGA bulk samples are made and cross-sections approximately 1 mm in thickness are cut using a wet-diamond saw and then polished. The resulting specimens for the cell study are 10 mm x 8 mm x 1 mm in dimension. Again, immediately prior to the cell study, the specimens are UV sterilized for 1 hr.

2.4.3.1 24-hour Osteoblast Cell Study

The rat calvarial osteoblast culturing procedures described in Section 2.3.2.2 is followed in this study. In this study, however, *in situ* imaging of attached cells cannot be performed since the specimens are opaque. Instead, after 24 hrs of cell culture, the cells are fixed and specimens are prepared for SEM imaging.

2.4.3.2 Cell Fixation, Post-fixation, and Preparation for SEM Imaging

Cell fixation is undertaken to preserve the osteoblast cell structure with minimal change from its living state and to protect the specimen from alterations resulting from further processing. Here, fixation is achieved by adding 0.5 ml of 2.5% glutaraldehyde solution, diluted with phosphate buffered saline (PBS), at 37 °C to each well. After 20 min, another 0.5 ml of the glutaraldehyde solution is added. The solution is removed after 20 min and the specimens are rinsed with PBS.

Post-fixation of the cells is then used to stabilize and stain the cell membrane for improved SEM images. Post-fixation is performed by adding approximately 1 ml of a 1% osmium tetroxide solution, diluted with Hepes buffer, to each well. The specimens are then bio-microwaved (Pelco Biowave, max temp of 37 °C) for 1 min to accelerate post-fixation.

After fixation and post-fixation, the specimens are rinsed thoroughly with PBS and are then dehydrated via graded methanol baths. Here, specimens are placed in microporous specimen capsules (SPI, 30 μm pore size) and submerged in a 50 ml 5% methanol bath and placed in a bio-microwave for 1 min. The concentration of the bath is increased in increments of 5% until a 100% methanol bath is reached, with microwaving at each increment. The specimens are then dried in a critical point drying apparatus (Denton, DCP-1) for approximately 2 hrs. The specimens are then vapor-coated and sputter-coated for SEM as described in the Section 2.4.2.1.

2.4.3.3 Results and Discussion

Representative images of the HA/PDLGA specimen surface after 24 hrs of cell culture are shown in Figure 2.16. When compared to the OM images of the PDLGA specimens after 24 hrs (Figure 2.11b), it is more obvious in these images that the osteoblasts are indeed attached and spreading into a finger-like structure, indicative of a normal osteoblast phenotype.

In addition, there is evidence of dead cells in the images as indicated by the arrows in Figure 2.16, although the cause of death is unclear. Since there are cell fragments lying on cells already attached and spreading, it seems as though the cells died in solution and came to rest on the surface. It is unknown whether the cells died from a reaction to the specimens, or perhaps from a reaction to the fixation procedure, or from another unconsidered cause. Since there are numerous observations of cells attached and spreading on the specimens, it is considered unlikely that the cells that are observed to have died did so from a reaction to the specimens.

Since the osteoblasts are observed to be attached and spreading in all HA/PDLGA specimens after 24 hrs, the HA/PDLGA as processed does not inhibit cell attachment and spreading.

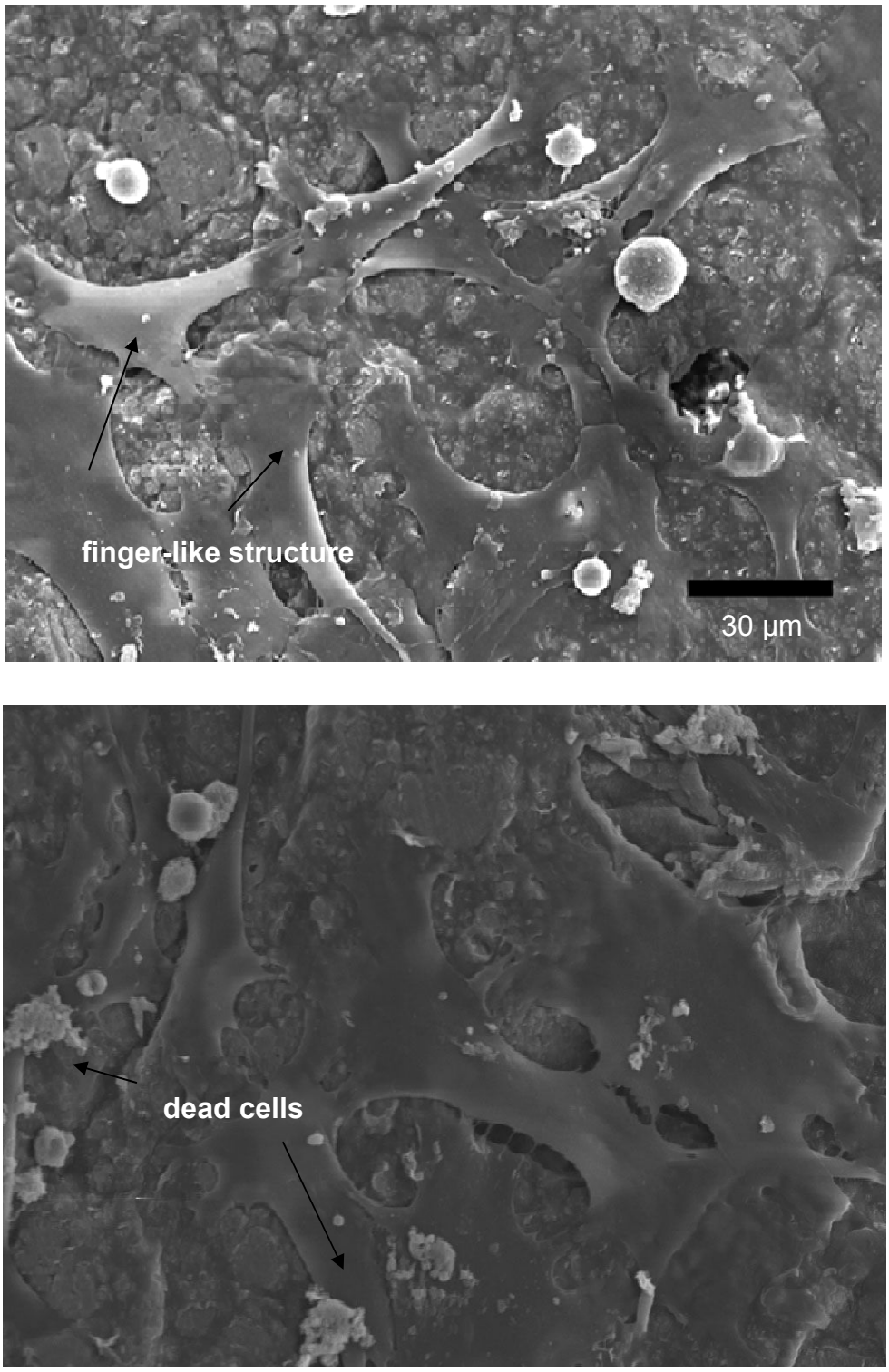

Figure 2.16. SEM image of osteoblasts attached and spreading on the surface of HA/PDLGA after 24 hrs.

2.5 Infiltrated Carbon Foam Systems

This section describes the PDLGA/Carbon Foam and HA/PDLGA/Carbon Foam material systems created and the morphology of the samples as processed. In this effort, OM and SEM techniques are used to observe any cracks, voids, and debonds present from processing, and EDS is used to investigate HA dispersion in the HA/PDLGA/C specimens. Lastly, the same 24-hr cell study performed previously is repeated on the PDLGA/Carbon Foam specimens. Although no cell studies are performed on the HA/P/C specimens (the processing technique for the HA/P/C was not refined at the time of the cell studies, thus no specimens available), the results for the HA/PDLGA specimens and the PDLGA/Carbon Foam specimens are extrapolated to the HA/P/C specimens.

2.5.1 PDLGA/Carbon Foam

2.5.1.1 Bulk Sample Preparation

As described in Section 2.2.2, the PDLGA/Carbon foam bulk samples are created by first cutting a carbon foam specimen is to the approximate size of the mold and then melting the PDLGA film on top of the foam in a vacuum oven. The foam is filled with the polymer melt by evacuating the vacuum oven chamber until a vacuum of 30 mm Hg is reached. In this process, there are still voids present in the foam/PDLGA melt, thus it is necessary to pull a vacuum, hold, and release vacuum several times to ensure the entire foam specimen is infiltrated completely. A picture of a typical PDLGA/Carbon foam specimen is presented in Figure 2.17a.

2.5.1.2 Morphology

OM images of cross-sections of PDLGA/Carbon foam specimens reveal the PDLGA phase to be relatively void-free. A typical foam ligament-PDLGA interface is shown in Figure 2.17b, where no debonding between PDLGA and carbon foam is observed as a result of cool-down from 190 °C to room temperature. In addition, no cracks are observed in the foam ligaments in the cross-sectional images.

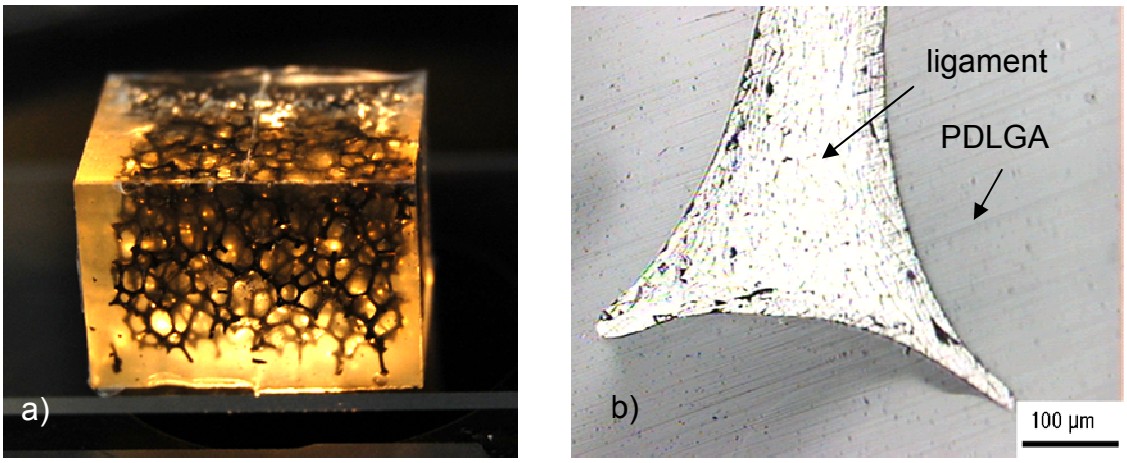

Figure 2.17. PDLGA/Carbon foam: a) bulk specimen (16mm x 10mm x 10mm), illuminated for photo, b) OM image of ligament cross-section in PDLGA.

2.5.2 HA/PDLGA/Carbon Foam

2.5.2.1 Bulk Sample Preparation

As stated in Section 2.2.2, the carbon foam cannot be infiltrated with the HA/PDLGA melt with the use of the vacuum oven because of the melt's high viscosity at 190 °C. Instead, the foam is placed in the mold, the pieces of HA/PDLGA film are placed on top on the foam, heated to 190 °C, and pressed into the foam to create the HA/PDLGA/Carbon foam specimens. An image of a typical HA/PDLGA/Carbon foam bulk sample is shown in Figure 2.18a.

Because the melt is physically pressed into the foam, there is the possibility that the foam can be crushed if care is not taken in the infiltration process. This in turn results in a possibility that the foam will not be completely infiltrated, leading to a potentially higher void content when compared to HA/PDLGA specimens created in the melt casting process. Thus it is necessary to inspect the morphology of the HA/PDLGA/Carbon Foam specimens for void content, damage to the foam microstructure, and debonds between the foam and HA/PDLGA phase. In addition, it is of interest to ensure the infiltration process did not affect the dispersion of HA particles throughout the PDLGA phase.

2.5.2.2 Morphology

As in Section 2.4.2, the morphology of the HA/PDLGA/C specimens is inspected using OM, SEM, and EDS techniques. The cross-sectioned and fractured specimens are prepared in the same manner as described in Section 2.4.2.

A typical OM image of a polished cross-section is shown in Figure 2.18b, where multiple voids are observed. The image is oriented such that the pressing direction is from the top to bottom, so the small voids at the bottom of the image are located towards the bottom of the specimen. Although this particular image is from the middle of a bulk sample specimen, cross-sectional images throughout the length of the bulk sample are similar.

It should be noted that most voids occur in the middle of a foam pore, that is, no voids are observed to be adjacent to a foam ligament. This indicates the foam microstructure does not inhibit the HA/PDLGA melt flow in the infiltration process. Additionally, no debonds are observed at the foam-HA/PDLGA interface and no ligament cracks or ligament fragments are observed in the HA/PDLGA phase, indicating the foam microstructure was not damaged in the infiltration process.

The void content of the specimens is calculated based on density measurements of the final specimen. The theoretical density is calculated for the given densities of the constituents and volume fractions, and the difference between the measured density and theoretical density is attributed to void content. The average void content for the specimens is ~5%.

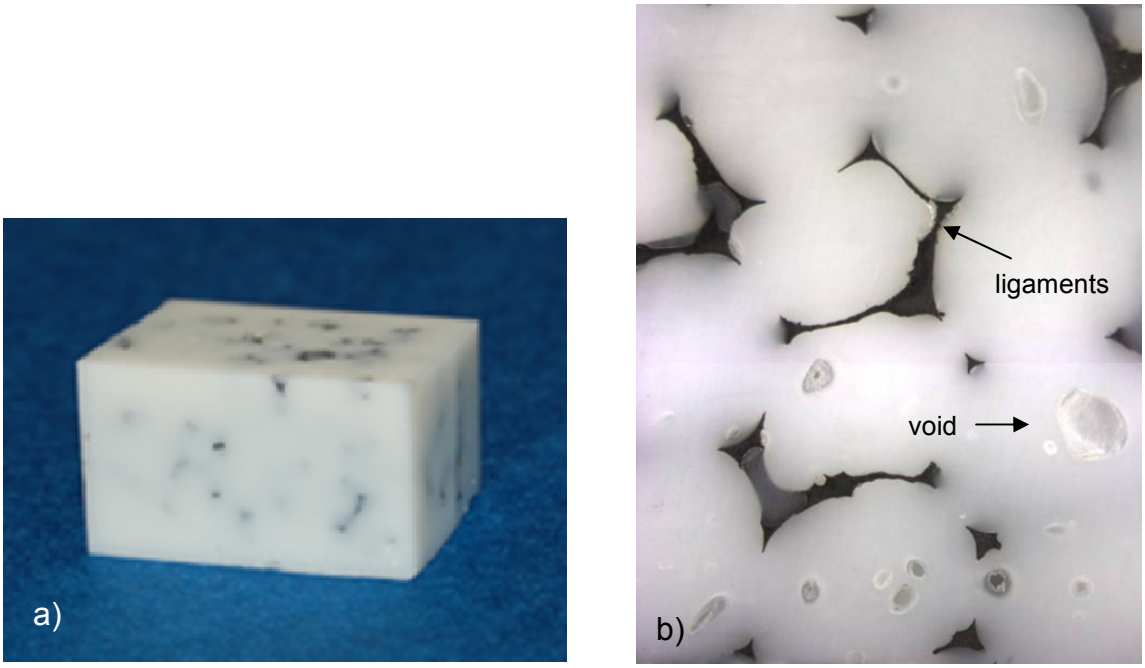

Figure 2.18. HA/PDLGA infiltrated carbon foam: a) bulk specimen (16mm x 10mm x 8mm), b) SEM image of cross-section.

The EDS analysis coupled with SEM is used to determine dispersion of HA particles in the PDLGA phase of HA/PDLGA/Carbon foam. A SEM image of a fractured surface of a carbon ligament and surrounding HA/PDLGA is shown in Figure 2.19a. An EDS mapping of this same region is shown in Figures 2.19b-d, where carbon, calcium, and phosphorous elements are identified. Note that in Figure 2.19b, the carbon mapping is more dense where the ligament is located, which is to be expected since the ligament is comprised of carbon. There is also carbon present in the surrounding matrix, which is attributed to the elemental carbon present in PDLGA as well as the carbon sputter-coating. In Figures 2.19c and 2.19d, calcium and phosphorous elements are observed in the areas neighboring the ligament, which are from the HA ($Ca_5(OH)(PO_4)_3$)

particles. In addition, the calcium and phosphorous element maps indicate a homogenous distribution of HA particles in PDLGA, both near and far from the carbon foam ligament, indicating the foam microstructure does not affect the HA distribution in the PDLGA.

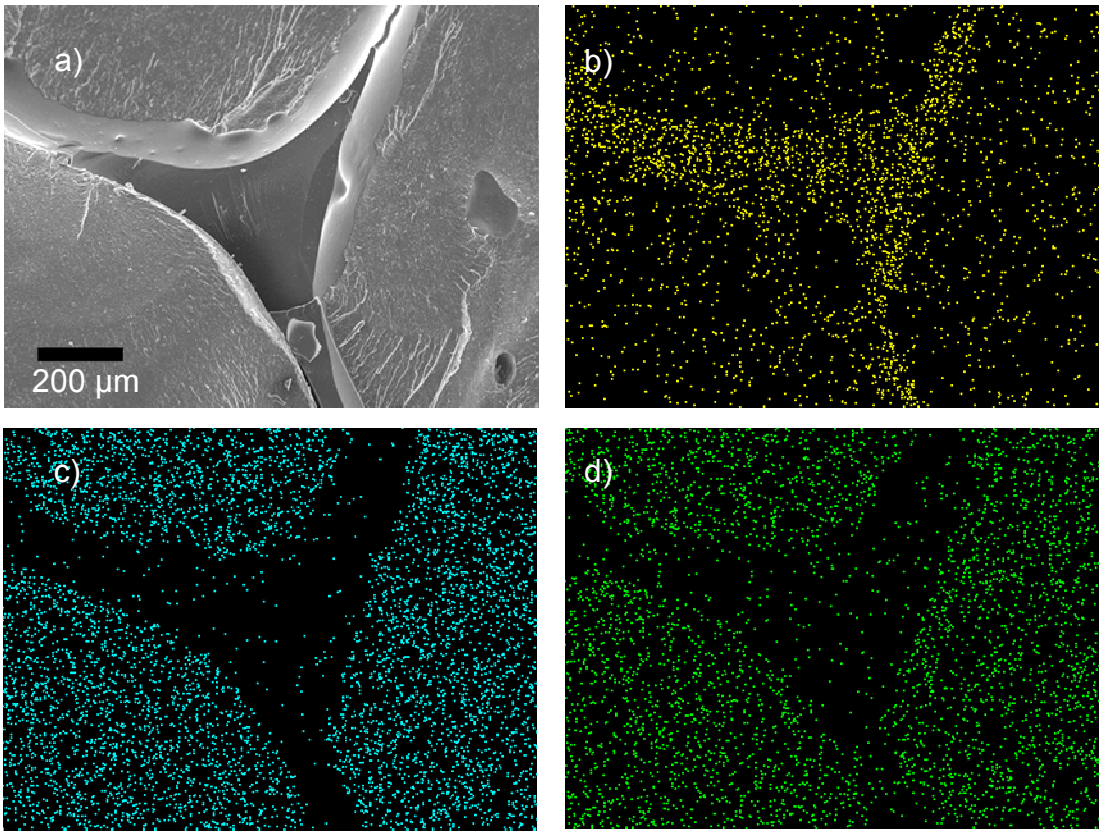

Figure 2.19. a) SEM image of fractured surface of HA/PDLGA/Carbon foam and corresponding EDS maps of b) carbon, c) calcium, and d) phosphorous.

2.5.3 Biocompatibility

The same 24-hour osteoblast study previously performed is carried out on the PDLGA/Carbon foam samples. A typical OM image of the surfaces of the PDLGA/Carbon foam specimen after 3 hrs of cell-culture is shown in Figure 2.20. This image shows attached osteoblasts to the surface of the PDLGA phase of the specimen.

No study was performed on the HA/PDLGA/Carbon foam because that processing technique was not refined at the time of the cell study. However, since no abnormal cell reactions are observed in the HA/PDLGA study and the PDLGA/Carbon foam study, is assumed the results will be similar for the HA/PDLGA/Carbon foam specimens.

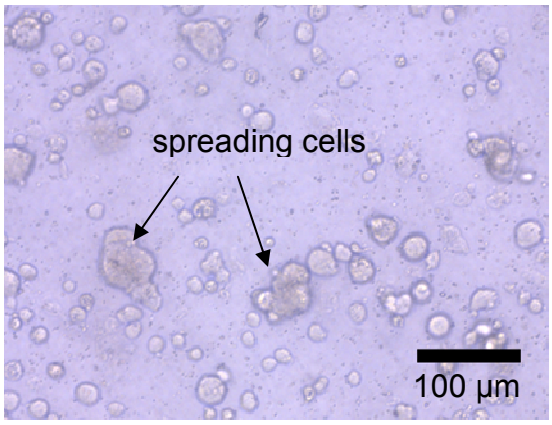

Figure 2.20. OM images taken 3 hrs after rat calvarial osteoblasts cultured on polymer phase of PDLGA/Carbon foam.

2.6 Remarks

As shown in Figures 2.14 and 2.19, it is seen that the HA particles are distributed homogenously throughout the PDLGA using the processing technique described in Section 2.2. In addition, no debonds are observed between the polymer/carbon foam interface and no ligament damage is observed in the as-processed specimens. It is seen, however, that voids tend to form in the bulk specimens as a result of the pressing technique used in the melt casting process. These investigations reveal that there is a trade-off in infiltrating the carbon foam: care must be taken when pressing the HA/PDLGA melt through the carbon foam so as not to damage the foam ligaments; however voids occur in the HA/PDLGA phase when too little force is applied in the infiltration process.

Furthermore, the 24-hr cell studies with rat calvarial osteoblasts reveal that the processing technique used to create the material systems results in no abnormal cell behavior over the testing period.

3. INVESTIGATION OF MATERIAL DEGRADATION

3.1 Overview

This section describes the details of the experimental efforts to characterize the degradation mechanisms of the material systems under investigation. Since degradation of the material system and the resulting change in mechanical properties is the crux of this research, special care is taken in the design and development of these experiments.

Recalling that in polymers that hydrolytically degrade, water molecules are first absorbed by the polymer and they then cleave the polymer molecules through chain-scission mechanisms. As the polymer is exposed or immersed in water over long-term time periods, chain-scission proceeds until the polymer chains are short enough to be shed from the remaining bulk polymer. Throughout this degradation process, several events contribute to a change in polymer mechanical properties. First, the addition of water into the polymer through the water uptake process results in a material that can be thought of as a composite material consisting of a polymer phase and a water phase. The resulting properties of this composite material are a function of water content. Adding complexity to this situation is the fact that the water content varies spatially throughout the bulk polymer and is dependent on the polymer specimen geometry and also on the time of immersion.

The second mechanism that results in a change of mechanical properties in the polymer is the change of polymer molecular weight as degradation occurs. This is due to a polymer's property dependence on molecular weight, the relationship of which is typically determined experimentally. Again, this mechanism is complex since the

molecular weight of the polymer is related to water content and therefore varies spatially in the polymer specimen as well as varies with time.

The last mechanism that results in a change of mechanical properties is the physical dissolution of the polymer as the polymer chains becomes short enough to be shed from the bulk polymer. This dissolution leads to a physical change of dimensions of the polymer, affecting the subsequent stiffness/strength of any device that is composed of the material.

Because of the influence of water content on the change in mechanical properties, it is of interest to determine the water concentration throughout the polymer as a function of time. To this end, water is assumed to diffuse into the material following Fick's law and experiments are designed and conducted to determine a coefficient of water diffusion for the HA/PDLGA/Carbon foam (HA/P/C) material system created. The governing equations for one-dimensional diffusion are developed and given in Section 3.2.

Section 3.3 and 3.4 describe the degradation experiments that are performed to determine the degradation characteristics, including characteristics of diffusion-driven water uptake as well as characteristics of dissolution of material over time. *In vitro* degradation testing of specimens is performed by incubation in a simulated physiological environment over the course of three to four weeks. Thin specimens are chosen for the experiments in an attempt to restrict diffusion to one dimension to reduce the complexity of the degradation problem. The time-line of three to four weeks is chosen because it is of interest to determine the degradation characteristics of the material systems in relation

to the healing rate of bone. As potential applications for this material are orthopedic fixation devices, a critical part of the healing time-line is in the early stages of the healing process where the fracture is bridged with low-modulus and low-strength tissue.

Specimens are immersed in phosphate buffered saline and change in mass over time is measured. After an initial period of water uptake into the specimens, the polymer phase begins to degrade and subsequently dissolves. Additionally, a rate of dissolution is found for the material systems based on the experimental data. An initial mass gain study of PDLGA, HA/PDLGA (HA/P), and HA/P/C specimens is described in Section 3.3 and results presented; finally a more comprehensive mass gain and mass loss study of HA/P and HA/P/C is given in Section 3.4 where this data is used to determine the diffusion coefficient and dissolution rate.

3.2 Diffusion

The degradation process of the bioresorbable polymer consists of the polymer absorbing moisture through diffusion driven by concentration gradient, resulting in polymer chains hydrolytically cleaving until eventually the chains dissolve into the surrounding fluid. As such, it is of interest to gain knowledge of the process of water diffusion into the polymer. In order to design an experiment to determine diffusion coefficients it is necessary to take a deeper look at the governing equations of diffusion.

3.2.1 Governing Equations

The governing equations are developed by first assuming diffusion adheres to Fick's 1st law which is of the form

$$J = -D\frac{\partial C}{\partial x} \tag{3.1}$$

where J is diffusion flux, D is diffusion coefficient and C is concentration. From conservation of mass in one dimension

$$\frac{\partial C}{\partial t} = -\frac{\partial}{\partial x}J \tag{3.2}$$

Substituting Equation 3.1 into Equation 3.2 results in

$$\frac{\partial C}{\partial t} = -\frac{\partial}{\partial x}\left(-D\frac{\partial C}{\partial x}\right) \tag{3.3}$$

If it is now assumed D is constant throughout the material and is independent of concentration, Equation 3.3 can be reduced to

$$\frac{\partial C}{\partial t} = D\frac{\partial^2 C}{\partial x^2} \tag{3.4}$$

otherwise recognized as Fick's 2nd law.

3.2.2 Solution for Immersion of Thin Specimens

If experiments are designed such that the specimens are sufficiently thin so diffusion is restricted to through-the-thickness, the diffusion response is one-dimensional and Equation 3.4 can be employed. The dimensional criteria for one-dimensional diffusion is sometimes taken as $A^{1/2} >> 2l$, where A is specimen cross-sectional area and l is specimen half-thickness[52]. If a specimen is exposed to some solution or gas where

the concentration of the solution does not change, the initial conditions are as shown in Figure 3.1. In this scenario, C_O is the initial internal concentration at $t = 0$ and C_1 is the concentration of the conditions at which the specimen is exposed to for $t \geq 0$. Applying these initial and boundary conditions to Equation 3.4 results in the solution presented by Crank[53] as

$$\frac{C - C_O}{C_1 - C_O} = 1 - \frac{4}{\pi}\sum_{n=0}^{\infty}\frac{(-1)^n}{2n+1}\cos\frac{(2n+1)\pi x}{2l}exp\left[\frac{-D(2n+1)^2\pi^2 t}{4l^2}\right] \qquad \textbf{(3.5)}$$

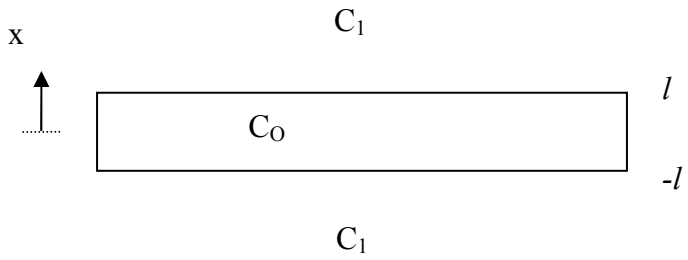

$C = C_O$ at $-l < x < l$ for $t = 0$

$C = C_1$ at $x = -l$, $x = l$ for $t \geq 0$

Figure 3.1. Initial and boundary conditions on a thin specimen with *l* half-thickness.

As Jost notes, the solution given in Equation 3.5 is for localized concentration whereas experimental methods typically measure total amount of substance absorbed. As such, letting M_t denote the total moisture content at time t and M_∞ denote total moisture content at time ∞, M_t is found by integrating Equation 3.5 over the specimen thickness

$$M_t = \int_{-l}^{l} C(x,t)\, dx \tag{3.6}$$

This operation is performed for the case where C_O is 0 (no initial moisture content), the details of which are found in Appendix A. Carrying out the integration results in

$$M_t = 2C_1 l - 2C_1 l \sum_{n=0}^{\infty} \frac{8}{(2n+1)^2\pi^2} exp\left[\frac{-D(2n+1)^2\pi^2 t}{4l^2}\right] \tag{3.7}$$

At $t = \infty$ it is seen that the exponential function is 0, thus

$$M_\infty = 2C_1 l \tag{3.8}$$

Finally dividing Equation 3.7 by Equation 3.8 results in the form presented by Crank[53]

$$\frac{M_t}{M_\infty} = 1 - \sum_{n=0}^{\infty} \frac{8}{(2n+1)^2\pi^2} exp\left[\frac{-D(2n+1)^2\pi^2 t}{4l^2}\right] \tag{3.9}$$

The above form can be used with experimental results to measure the diffusion coefficient D of a given material. Noting that M_∞ is typically taken as moisture content at fully saturated conditions, the diffusion coefficient D can be calculated from an experiment where a specimen of known l is immersed in a solution and moisture content is measured over time via mass measurements. Often large-time assumptions are used to simplify Equation 3.9 by taking only the first term in the series[52, 53]. Here, no such assumption is made and the full series is used.

3.3 Initial Mass Gain Study of PDLGA, HA/P, and HA/P/C

A diffusion study is undertaken to determine diffusion coefficients of PDLGA, HA/P, and HA/P/C specimens. In this experiment thin cross-sections are cut from bulk specimens in an attempt to limit diffusion to one dimension. Specimens are then immersed in phosphate buffered saline and placed in an incubator at 37 ^{o}C, 5 % CO_2, and 95% relative humidity. The mass of the specimens are taken at periodic intervals to calculate the water uptake values.

3.3.1 Specimens

Cross-sections are cut from bulk specimens using a precision diamond saw (Secotom-10, Struers). The dimensions of the PDLGA, HA/P, and HA/P/C specimens are given in Table 3.1. Average thicknesses for the HA/P/C, HA/P, and PDLGA specimens are 0.57, 0.51, 0.54 mm, respectively. In attempting to cut the PDLGA specimens, care is undertaken not to fracture the specimens while mounting them in the fixture of the diamond saw. It should be noted that thin cross-sections are difficult to cut from the HA/P/C specimens because of the tendency of the thin sections to curl while being cut. Thus, the average thickness of the HA/P/C specimens in this study is larger than the HA/P and PDLGA specimens.

Table 3.1. Specimen dimensions.

	Sample	Width (mm)	Length (mm)	Thickness, 2*l* (mm)
HA/P/C				
	# 1	7.5	9.8	0.57
	# 2	7.5	9.5	0.54
	# 3	7.6	9.6	0.67
	# 4	7.5	9.7	0.56
	# 5	7.6	9.8	0.57
Average		**7.5**	**9.7**	**0.57**
HA/P				
	# 1	6.9	9.8	0.55
	# 2	6.8	9.9	0.52
	# 3	6.8	9.8	0.52
	# 4	6.7	9.8	0.52
	# 5	6.8	9.8	0.50
	# 6	6.8	9.8	0.48
	# 7	6.8	9.8	0.50
Average		**6.8**	**9.8**	**0.51**
PDLGA				
	# 1	7.4	9.9	0.51
	# 2	7.4	8.8	0.50
	# 3	7.4	9.9	0.66
	# 4	7.4	9.9	0.55
	# 5	7.4	9.9	0.50
	# 6	7.4	10.0	0.51
Average		**7.4**	**9.7**	**0.54**

3.3.2 In vitro Degradation

The mass of each specimen is measured and placed in a single well of a 12-well plate. The specimens are sterilized in a two step process to prevent bacterial or fungal growth: first the specimens are immersed in a 70% ethanol solution for 30 minutes, the specimens are then UV sterilized for 30 minutes per side. Working in a sterilized hood, individual specimens are placed in well-inserts which have a porous bottom allowing for

exposure to PBS solution on all specimen surfaces. The well-inserts are then added to 12-well trays and 2 mL of PBS with 1% PSA is added to each well. PBS is replaced every other day to ensure degradation by-products do not affect the degradation behavior. At specified time points, the mass of each specimen is measured with an electronic balance in a sterile bio-hood. Each specimen is removed from the well tray and surface moisture is dabbed with a KemWipe. Mass is measured and recorded and the specimens are then replaced in the well tray, the old PBS is removed via vacuuming and fresh PBS replaced, and then placed back in the incubator. The water uptake response of the specimens is characterized by calculating the percent mass gain by using the relationship

$$Percent\ Mass\ Gain = \frac{M_0 - M_{t,w}}{M_0} \times 100 \quad \textbf{(3.10)}$$

where M_0 is initial mass and $M_{t,w}$ is wet mass at time t. Specimens are weighed at 2, 4, 5, 7, 9, 11, 14, 16, 18, 21, and 23 days. At the conclusion of the experiments, the specimens are dried and a final dry mass is measured.

3.3.3 Mass Gain Results and Observations

The HA/P and HA/P/C specimens were maintained in the incubator for the entire 23 day testing period, whereas the PDLGA specimens were removed at day 14. At this time period, the PDLGA specimens were in a gel-like state and upon dabbing the specimens surface moisture, excess moisture was squeezed from the specimens. As a result, only data up to day 11 is deemed reliable for the PDLGA specimens. The

average percent mass gain for each set of specimens at each time point is plotted in Figure 3.2. The bars indicate one standard deviation for the set average.

The PDLGA specimens absorbed moisture at a slower rate over the first five days when compared to the HA/P and HA/P/C specimens. The rate of absorption then increases over the next 6 days so that at day 11 the average mass gain of the PDLGA is comparable to that of HA/P and HA/P/C (69.7% vs 70.4% and 78.7%, respectively). The PDLGA exhibited blistering on the surface beginning at day 9 and by day 11 the specimens have a wrinkled surface texture. One specimen fractured while being handled at day 4, while another specimen fractured at day 5. These two specimens were kept in the experiment where the total mass of the fractured pieces were measured and used for the mass gain calculations. Fickian diffusion cannot be used to describe the PDLGA mass gain response since the curve is not of the exponential form as shown in Equation 3.9.

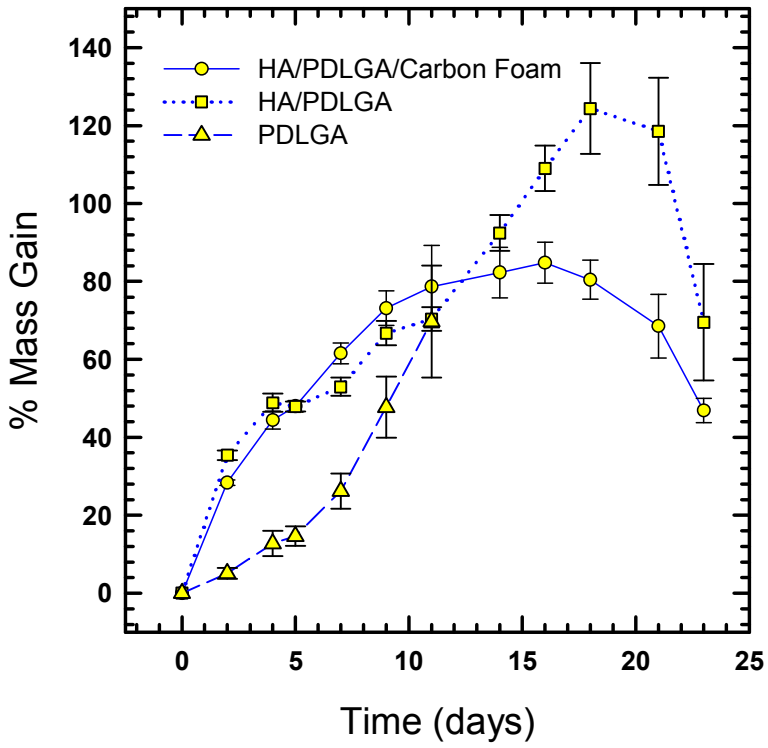

Figure 3.2. Percent mass gain as a function of time for PDLGA, HA/P, and HA/P/C specimens.

The HA/P specimens exhibited a Fickian-type mass gain response up until day 11 as shown in Figure 3.2. At day 14, however, the mass gain rate of the specimens increases again until it peaks at day 18 at a value of 123 % mass gain (10.8 Std Dev). Dissolution dominates the response thereafter as seen by the downturn in the mass gain curve. On the final day 23 measurement, the average mass gain for the HA/P specimens is 67% (11.3 Std Dev). When observing the surface texture over time, the specimens begin to exhibit surface blistering at day 11. Two specimens fractured from handling at day 11, with two more specimens fracturing at day 14. By day 16, four of the seven

specimens fractured while all seven specimens fractured by day 21. Again all fractured pieces were retained and total mass of the pieces were used for each measurement.

Like the HA/P specimens, a Fickian-type response is initially observed in the mass gain data. The mass gain response is observed to plateau at days 14 and 16 (82% and 85%, respectively) before the mass gain begins to decrease at day 18. On the final day 23 measurement the average mass gain for the HA/P/C specimens is 47% (3.1 Std Dev). Surface blisters are observed on HA/P/C specimens on day 11, similar to the HA/P specimens. One specimen fractured at day 14 and another fractured at day 18 while the other three specimens remained intact throughout the experiment.

Photographs of typical specimens immediately after removal from PBS at day 23 are shown in Figure 3.3. Note the pitted surface of the HA/P specimen as well as the HA/P phase in the HA/P/C specimen. Also note the yellowish hue of the HA/P/C specimens is an artifact of color adjustments in Photoshop to highlight the pitted features of the specimens. Since the specimens were always handled in the sterile bio-hood during the experiment, adequate photographs were not able to be taken during the experiment, thus no images are provided during degradation.

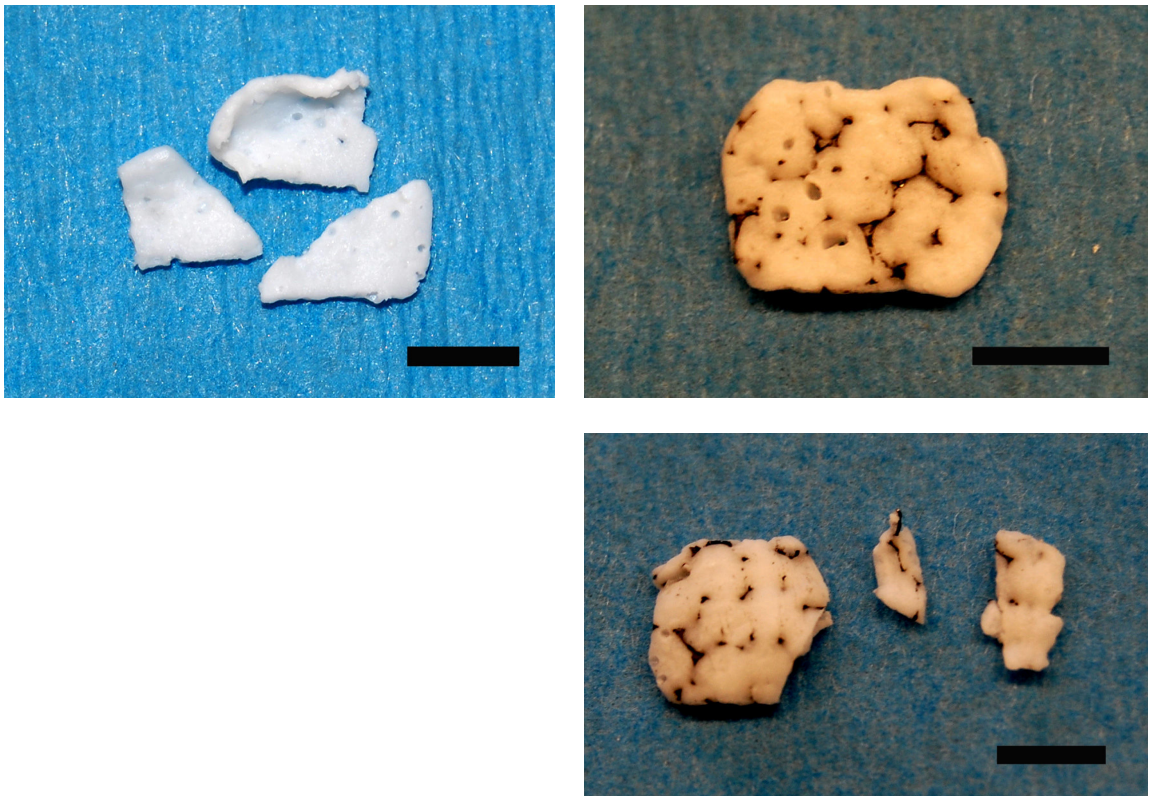

Figure 3.3. Photographs of HA/P and HA/P/C specimens at Day 23 (microbar = 5 mm).

3.3.4 Discussion

As mentioned previously the PDLGA specimens' absorption response shown in Figure 3.2 cannot be described using a Fickian diffusion model. Initial moisture absorption in the first five days results in an average mass gain of 15.4 % (2.7%) where thereafter absorption increases at a more rapid rate to an average mass gain of 69.7% (14.4 %) at day 11. One possible explanation for this faster rate of water uptake at later time period could be the material's diffusion dependence on moisture concentration. That is, at later time periods the presence of moisture in the PDLGA increases the

materials ability to absorb more moisture. This type of response is physically possible because as the polymer initially absorbs moisture, the entangled polymer network is enlarged due to the presence of water, allowing additional water to diffuse easier through the material.

When introducing HA particles to PDLGA, intuition would expect the water uptake of the HA/P specimens to be lower than that of the neat PDLGA specimens, since there is less PDLGA material to absorb the moisture. When looking at the mass gain response in Figure 3.2, however, the average mass gain of the HA/P and HA/P/C specimens are much greater, 47.9% (1.3%) and 48.0% (1.5%) at day 5, respectively, compared to 15.4 % (2.7%) for that of PDLGA. One possible explanation for this higher water uptake that results with the addition of HA relies on the interface of the HA and polymer. If the interface between the HA particles and polymer are imperfect, a less tortuous path for water to diffuse is introduced into the PDLGA phase, thus resulting in higher uptake rates for the HA/P specimens.

The addition of carbon foam to the HA/P material system results in similar initial water uptake response when comparing the HA/P and HA/P/C mass gain curves. Although the HA/P/C specimens are only 3% carbon foam by volume, however, the mass gain curves are markedly different from that of the HA/P specimens in the later phases of the experiment. In this stage of the experiment, dissolution is dominating the response, thus the mass gain begins to decrease as the polymer dissolves. The mass gain of the HA/P/C specimens reaches a plateau at days 14 and 16 (84%) and then begins to decline, whereas the HA/P specimens show a mass gain peak of 123% (10.8%) at day

18. It is difficult to assess the cause of the mass gain peak of the HA/P specimens in this experiment. It is uncertain whether the peak is a real material response or a result of the multiple fracturing of the HA/P specimens beginning at day 11. As the specimens fractured, new diffusion surfaces were introduced so the secondary increase in water uptake could possibly be attributed to this increase in surface area.

3.4 Mass Gain / Mass Loss Study

A second degradation experiment is performed because of the uncertainties of the water uptake response in the previous experiment caused by the fracturing of the specimens. This experiment is designed such that a set of HA/P and HA/P/C specimens are removed from the experiment at nine time points to prevent excessive handling of the specimens during the experiment. Again thin cross-sections are cut from bulk specimens and then immersed in PBS and placed in an incubator at 37 ^{o}C, 5 % CO_2, and 95% relative humidity. At each of the nine time points, three HA/P and three HA/P/C specimens are removed, the wet mass is measured and recorded, the specimens are dried and the dry mass is recorded. Because these specimens are thicker than the previous experimental specimens, the experiment is extended because it is expected that complete degradation will take longer.

3.4.1 Specimens

Cross-sections are cut from bulk specimens using a precision diamond saw (Secotom-10, Struers). The initial dimensions of the 27 HA/P and 27 HA/P/C specimens are given in Tables 3.2 and 3.3. Note that the thicknesses of the specimens on average are larger than those of the previous experiment, in an attempt to prevent specimen

fracture. Again, some specimens curled while being cut; these specimens retained their curved geometry throughout the experiment. The curved geometry also results in less than accurate length measurements; as such the values given in Tables 4.2 and 4.3 are rounded to the nearest tenth of a millimeter.

Table 3.2. Geometry and mass measurements for each of the HA/P specimens at each time point of the experiment.

	Day								
Sample	2	5	8	11	14	17	21	26	34
#1									
W (mm):	8.50	8.60	8.80	7.40	8.70	8.08	8.45	8.22	8.35
L (mm):	11.2	11.2	11.2	10.9	11.4	11.2	11.2	11.3	11.3
T (mm):	0.89	1.02	0.85	0.83	0.86	0.80	0.82	0.84	0.86
Mass (mg):	129.41	149.42	135.49	108.78	130.80	111.04	122.07	125.24	128.04
#2									
W (mm):	8.70	8.30	8.20	7.50	8.10	7.58	7.85	8.20	8.05
L (mm):	10.9	11.3	11.1	11.0	11.1	11.2	11.4	11.2	11.1
T (mm):	0.85	1.01	0.85	0.89	0.83	0.86	0.83	0.80	0.76
Mass (mg):	121.82	145.80	111.62	112.58	108.93	106.55	114.72	109.96	104.82
#3									
W (mm):	8.10	8.50	7.60	7.50	7.80	7.50	8.19	7.45	7.40
L (mm):	10.0	11.4	10.5	11.1	11.2	11.2	11.3	11.2	11.0
T (mm):	0.75	0.91	0.82	0.99	0.86	0.82	0.84	0.80	0.78
Mass (mg):	109.88	135.37	101.14	127.72	122.09	107.71	116.77	108.31	99.80
Avg T (mm):	0.83	0.98	0.84	0.90	0.85	0.83	0.83	0.81	0.80
Avg M (mg):	120.37	143.53	116.08	116.36	120.61	108.43	117.85	114.50	110.89

Table 3.3. Geometry and mass measurements for each of the HA/P/C specimens at each time point of the experiment.

	Day								
Sample	2	5	8	11	14	17	21	26	34
#1									
W (mm):	8.80	8.80	7.40	7.50	7.60	9.30	9.70	8.80	9.30
L (mm):	11.7	11.1	11.18	11.1	11.1	11.3	11.3	11.1	11.4
T (mm):	0.82	0.75	0.81	0.99	0.81	0.78	0.76	0.73	0.95
Mass (mg):	125.49	112.80	101.75	122.73	100.52	133.56	140.53	117.05	160.09
#2									
W (mm):	8.80	8.80	7.45	8.30	7.50	9.90	9.50	9.25	9.50
L (mm):	11.5	10.9	11.20	11.1	11.2	11.2	11.3	10.6	11.3
T (mm):	0.92	0.78	0.81	0.98	0.81	0.84	0.76	0.72	0.92
Mass (mg):	142.72	125.52	102.74	138.31	100.84	145.30	135.56	126.36	148.12
#3									
W (mm):	8.80	8.80	8.25	8.40	8.30	9.20	8.90	9.00	9.70
L (mm):	11.1	10.5	10.8	11.0	11.3	11.4	11.3	11.2	11.3
T (mm):	0.82	0.78	0.75	0.82	0.75	0.83	0.77	0.73	0.97
Mass (mg):	125.82	119.93	106.68	113.36	104.43	135.88	122.09	121.12	164.32
Avg T (mm):	0.85	0.77	0.79	0.93	0.79	0.82	0.76	0.73	0.95
Avg M (mg):	131.34	119.42	103.72	124.80	101.93	138.25	132.73	121.51	157.51

3.4.2 In vitro Degradation

The degradation procedures described in Section 3.3.2 are followed in this experiment as well. In addition to the mass gain data measured using Equation 3.10, mass loss data is measured as using

$$Percent\ Mass\ Loss = \frac{M_0 - M_{t,d}}{M_0} \times 100\,, \tag{3.11}$$

where M_0 is initial mass and $M_{t,d}$ is dry mass at time t. As noted in Tables 3.2 and 3.3, each set of specimens are removed after 2, 5, 8, 11, 14, 17, 21, 26 and 34 days of degradation. Once the wet mass is measured immediately following removal, the

specimens are placed in a vacuum oven for 48 hrs, and then placed in a desiccator until the dry mass measurements reach a stable value.

3.4.3 Wet Mass and Dry Mass Results and Observations

The HA/P and HA/P/C degradation experiment was maintained for the entire 34 day period without experiencing any specimen fractures during immersion. However, two of the three day 34 HA/P specimens fractured upon removal from the well-tray, and the third specimen was in a gel-like state and could not be removed. At this time point, the mass gain measurements only include the values of the two fractured specimens. The average mass gain and average mass loss values of the specimens for each time period is presented in Figure 3.4. The bars for each data point plotted indicate one standard deviation for the average of the three specimens of each type.

Similar to the response of the HA/P specimens of the initial experiment shown in Figure 3.2, the HA/P here exhibited a Fickian-type mass gain response up until day 11, as shown in Figure 3.4. At day 14, however, the mass gain rate of the specimens increases again until it peaks at day 17 at a value of 84.0% mass gain (9.57 Std Dev). At the final day 34 measurement for the HA/P experiment, the two remaining specimens had an average percent mass gain of -1.5% (2.30 Std Dev). Although a negative value for mass gain may seem counterintuitive, recall the mass gain is a measurement of the specimen mass plus water content relative to the mass of the initial specimen, as given in Equation 3.10. As such, a negative value indicates that the remaining specimen mass and water content are less than the initial mass of the specimen.

Looking at the mass loss data of the dry specimens presented in Figure 3.4, the average mass of the HA/P specimens after 5 days of immersion is 97.4% (0.29 Std Dev) of the initial mass. At 11 days of immersion, the average dry mass to initial mass ratio is 96.1% (0.22 Std Dev). At day 17, the average value begins to decrease more rapidly, from a value of 89.6% (2.13 Std Dev) at day 17 to a value of 64.6% (3.25 Std Dev) at day 26. Day 34 values are not presented for the HA/P because upon drying, the specimens further fragmented handling, making it difficult to collect all parts of each specimen.

The HA/P/C specimens again exhibited an initial Fickian-type response as observed in the mass gain plot in Figure 3.4a. The mass gain response is observed to plateau at days 11-21 at a value of about 54% and begins to decrease at day 26. Between days 26 and 34, the mass gain drops rapidly to a value of -7.0% (4.39 StdDev) at day 34.

Looking at the HA/P/C dry mass loss data presented in Figure 3.4b, the mass loss curve of the HA/P/C specimens is similar that of the HA/P specimens through day 14. At day 17 of degradation, the average dry mass to initial mass ratio is 93.3% (0.55 Std Dev). At day 21, the average value begins to decrease more rapidly, from a value of 89.8% (1.38 Std Dev) at day 21 to a value of 75.6% (1.10 Std Dev) at day 26. Although it may not be statistically significant since there are only three data points in each set of measurements, it is noteworthy that the standard deviation of each point in the mass gain data up to day 11 (Figure 3.4) is relatively smaller compared to the data points following this time point. This same observation can be made with respect to the mass loss data as well.

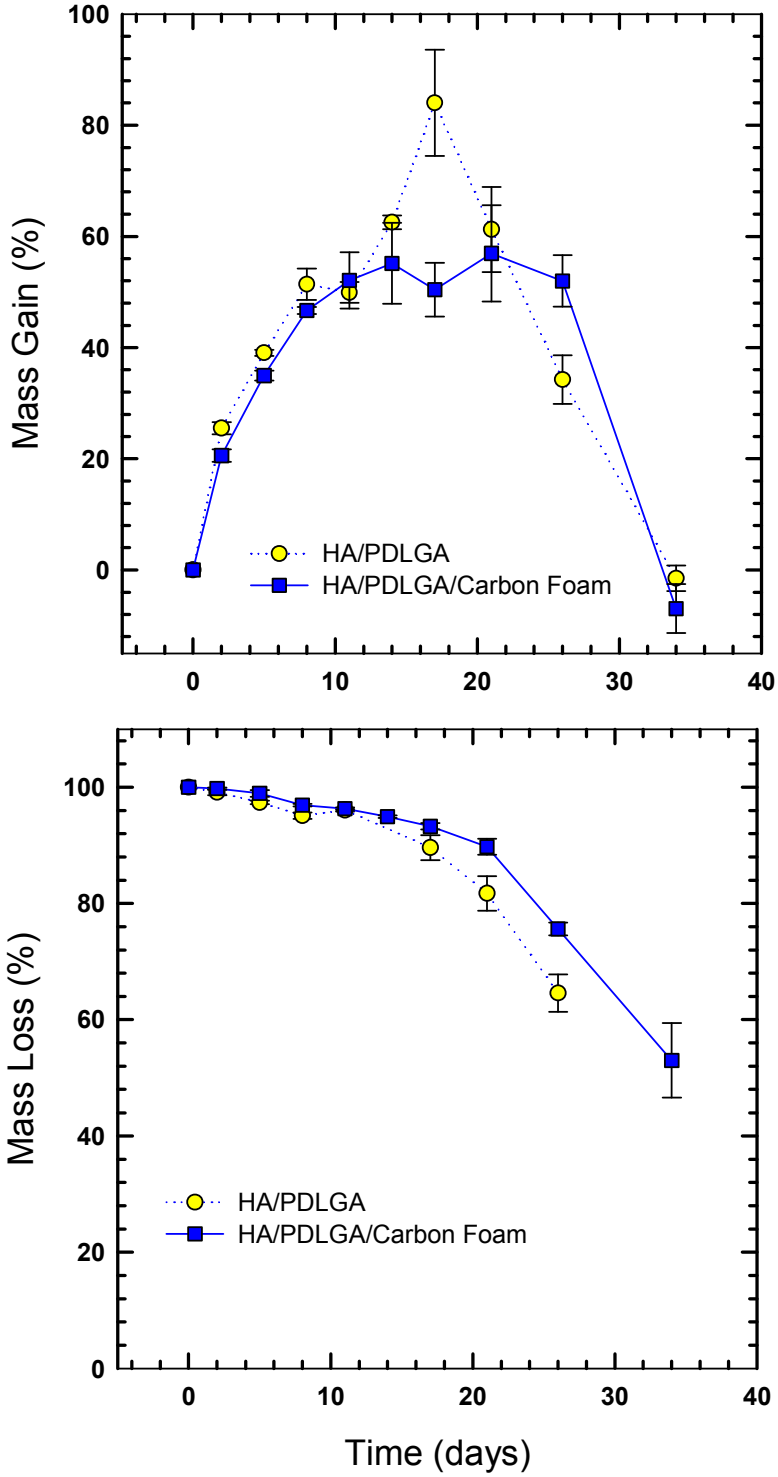

Figure 3.4. Percent mass gain and percent mass loss for the HA/P and HA/P/C specimens.

Photographs of HA/P specimens after 8, 14, 17, 26, and 34 days of degradation are shown in Figures 3.5 and 3.6. The photographs labeled as "wet specimens" were taken immediately after removal from the experiment and mass measurements are recorded while the images labeled as "dry specimens" were taken after the drying process. When comparing the progression of degradation between specimens, first note in Figure 3.5 that the day 8 specimen still has a relatively smooth surface texture with the exception of what appears to be a blister forming where the arrow indicates. The surface texture of the day 14 specimen has a somewhat rougher appearance in addition to two blisters that are slightly larger than that at day 8.

After 17 days of immersion, the HA/P specimens have large-scale blisters, as evident from the wet specimen images in Figure 3.5. The profile of the largest blister observed is shown, where the thickness of the blister is approximately 3-4 times that of the specimen. When looking at the dry specimen images, it seems as though the blisters collapsed, as indicated by the arrow. In addition, the surface of the specimens has a wrinkled appearance.

The wet and dry images of a day 26 HA/P specimen and two day 34 specimens are shown in Figure 3.6. Here it is seen that the specimens exhibit the same pitted surface observed in the prior experiment, as indicated by arrows. As previously noted, the day 34 HA/P specimens were fractured upon an attempted removal from the well-tray insert. The specimens at this time period had a tendency to slightly adhere to the insert surface, thus making removal difficult. It is also noteworthy that the third specimen at day 34 resulted in a gum-like material that was not intact.

Day 8 – Dry Specimens

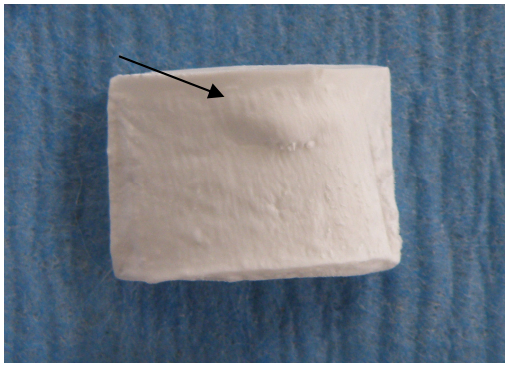

Day 14 – Dry Specimens

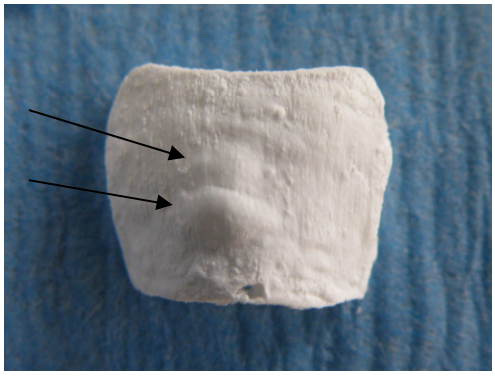

Day 17

Wet Specimens

Dry Specimens

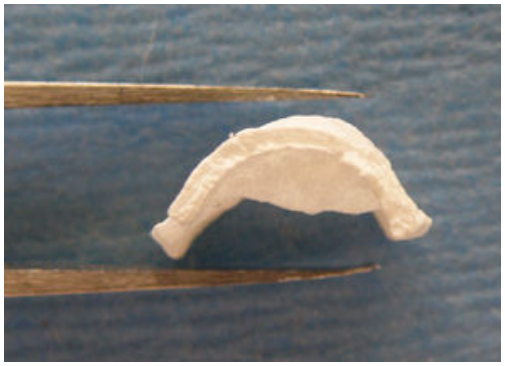

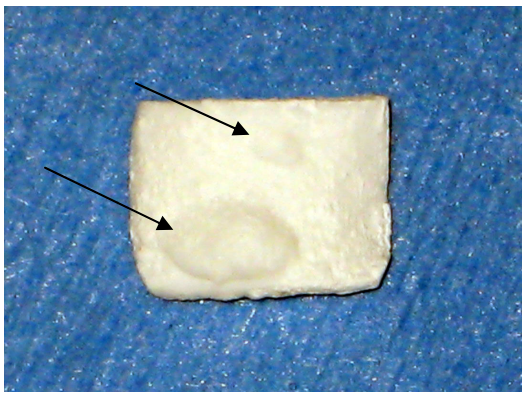

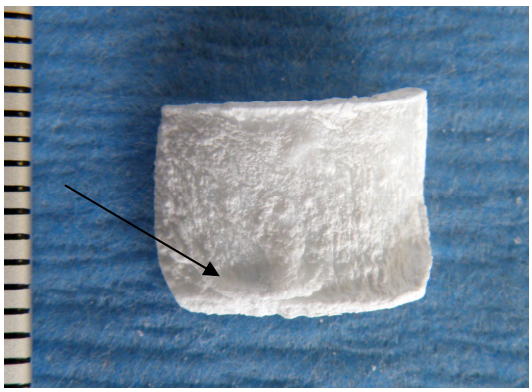

Figure 3.5. Photographs of dry HA/P specimens at days 8 and 14, and two day 17 specimens in the wet and dry states.

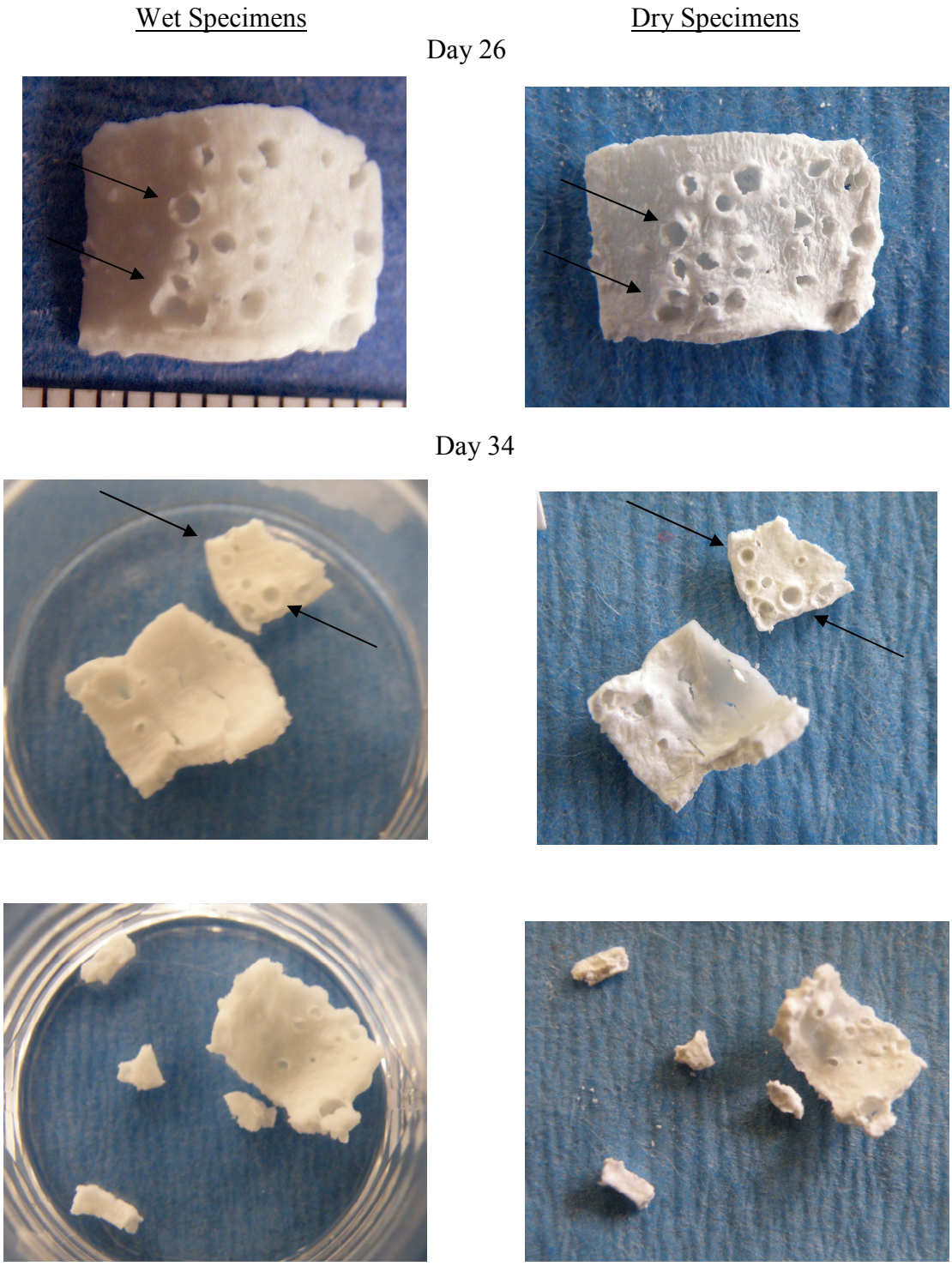

Figure 3.6. Photographs of wet and dry HA/P specimens at days 26 and 34 of degradation.

Photographs of dry HA/P/C specimens are shown in Figure 3.7 and photographs of HA/P/C specimens in the wet and dry states are shown in Figure 3.8. In looking at the degradation progression of the dry specimens in Figure 3.7, it is first seen that there are no large-scale blisters or collapsed blisters such as those observed in the HA/P specimens. The day 8 image shows a relatively smooth surface texture, whereas some surface roughness is observed in the day 11 image. In the day 11 and 14 specimens, the texture of the HA/P phase is rougher in appearance near the ligaments in comparison to areas further from the ligaments. The surface becomes gradually rougher in texture as degradation progresses until surface pits are observed in the day 26 specimens. Cracks in the HA/P phase of all three day 34 specimens are observed in addition to debonding of the HA/P from the carbon foam ligaments.

When looking at a comparison of the wet images and dry images of the HA/P/C specimens in Figure 3.8, it is first noted at day 11 there is non-uniform swelling of the HA/P phase throughout the cross-section, which is attributed to the localized constraint

of the foam ligaments. In addition, this particular day 11 specimen has what appear to be small surface pits as indicated by the arrows. No other specimens exhibited a pitted surface until day 26, so these features in the day 11 specimen may be the location of voids that were present on the specimen. Since no images of the specimens were taken before the experiment began, this cannot be proved and is only speculation.

On inspection of the day 26 HA/P/C specimens shown in Figure 3.6, the surface pits seem to be smaller and less frequent in occurrence than those found on the day 26 HA/P specimens as shown in Figure 3.6. The pits in the HA/P/C specimens appear in both the foam cavities as well as in areas that encompass the ligaments.

There are numerous cracks observed in the day 34 wet specimen that appear to be hairline cracks, as highlighted by the arrows in Figure 3.8. When looking at the same specimen after drying, however, there appears to be a significant gap in the cracks, indicating a significant state of swelling in the wet condition.

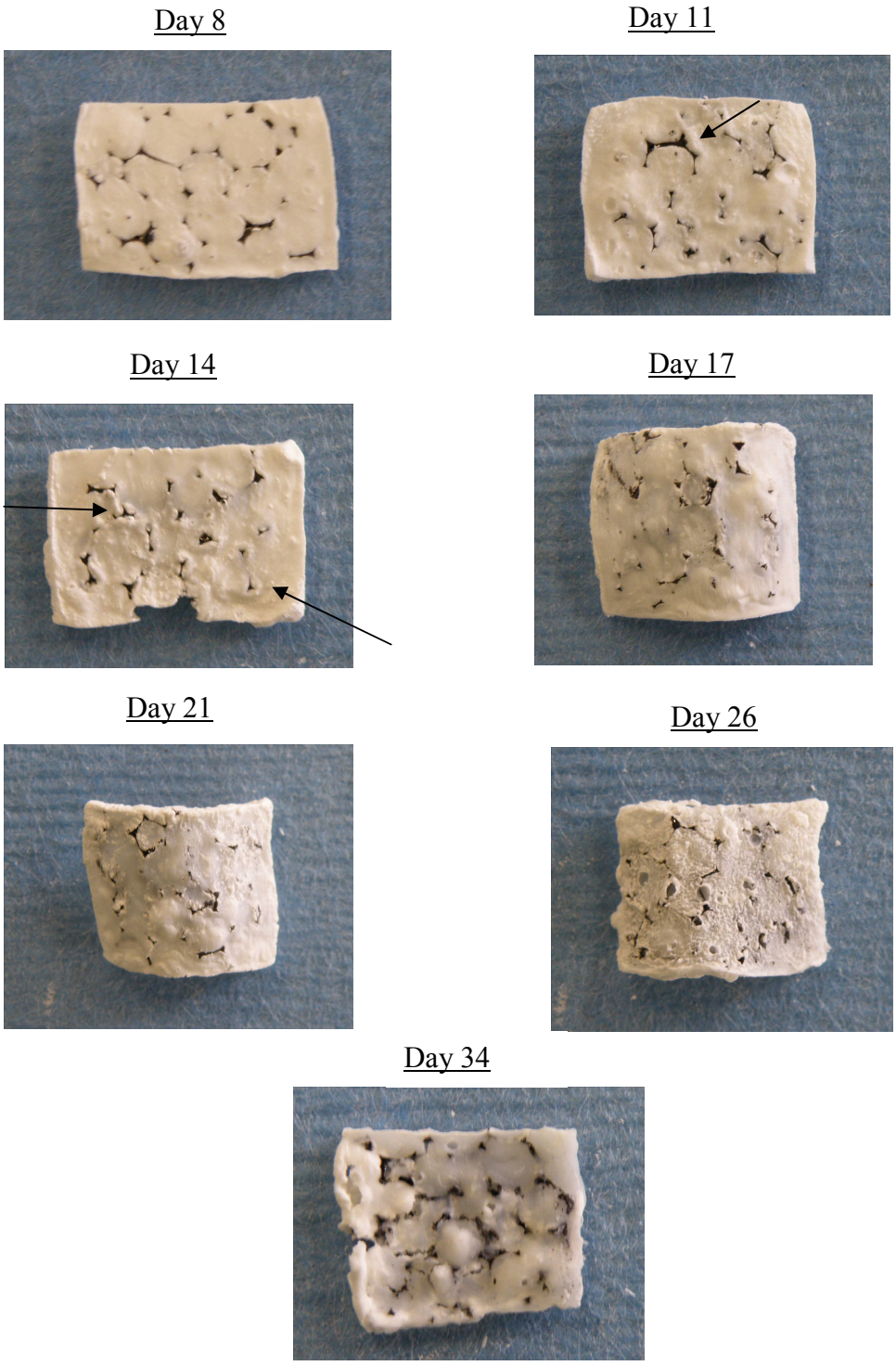

Figure 3.7. Photographs of dry HA/P/C specimens after 8, 11, 14, 17, 21, 26, and 34 days of degradation.

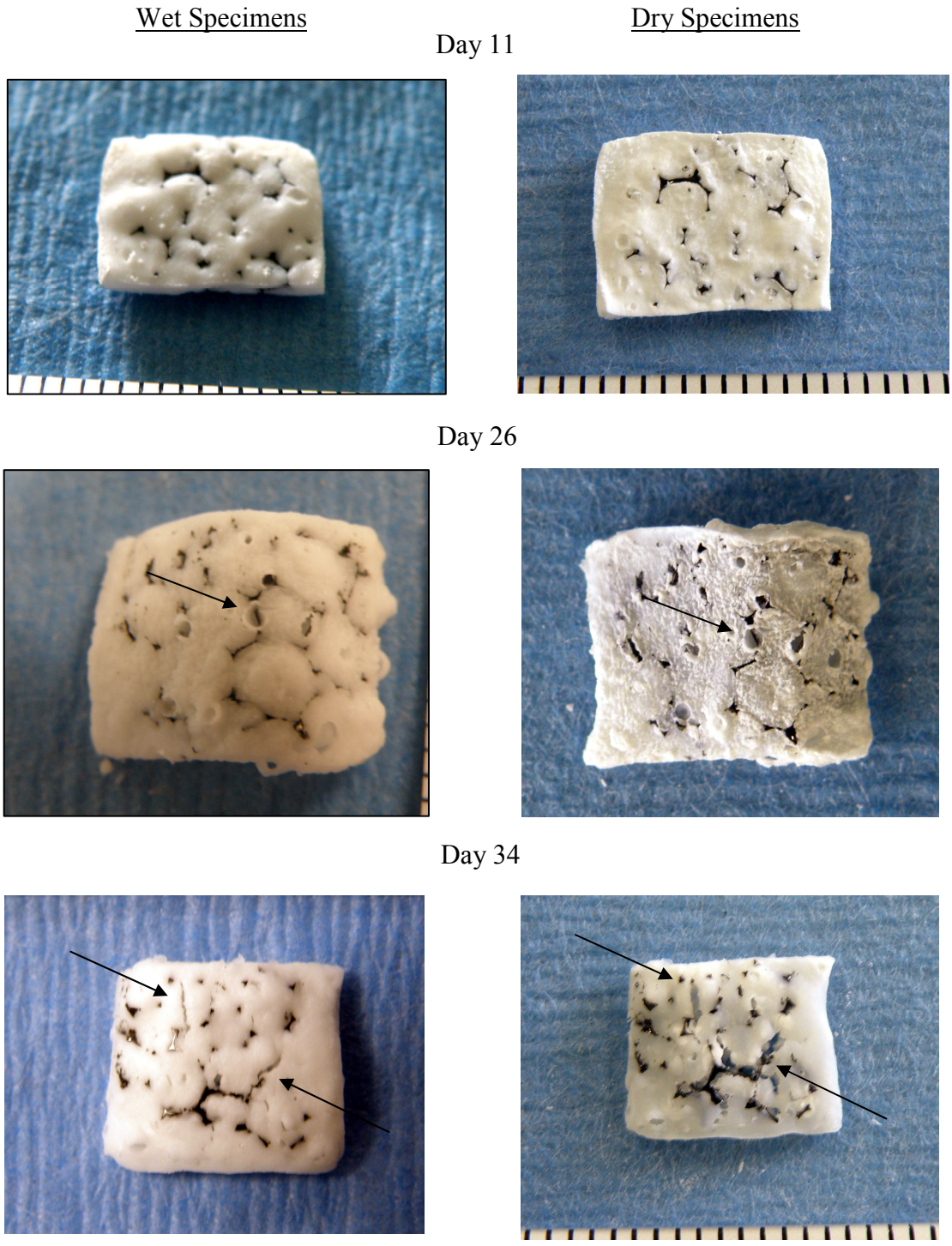

Figure 3.8. Photographs of wet and dry HA/P/C specimens at days 11, 26, and 34 of degradation.

3.4.4 Discussion of Experimental Observations

One of the unknown explanations in the previous degradation experiment described in Section 3.3 is the source of the mass gain peak of the HA/P specimens seen in Figure 3.2. Because the HA/P specimens in that experiment began fracturing at day 11, it is uncertain whether the peak is a real material response or a result of the increase in surface area from fracturing. No specimen fracturing occurred during immersion in this experiment, however, yet the peak in percent mass gain is again observed in the HA/P specimens. As such, it is concluded that the peak in percent mass gain is a real material response in the HA/P specimens.

One possible explanation for the secondary water uptake peak stems from the observation of the relatively large blisters present on the HA/P specimens at day 17, the day the peak in the data occurs. Since no blisters of that scale are observed on the HA/P/C specimens at any time, it is surmised that these blisters are the source of the peak. It is then of interest to understand why the HA/P specimens exhibit large scale blistering while the HA/P/C specimens do not.

It is postulated that the large scale blisters in the HA/P specimens are attributed to the chain-scission occurring in the polymer phase. As others have theorized in the study of PLGA membranes that have displayed similar characteristics of localized blistering and pinhole ruptures, the ruptures are caused by a secondary localized swelling occurring from a “decrease in chain retractive forces and tensile strength” due to hydrolysis[54, 55]. This is thought to be the underlying cause of the blisters in this experiment. As the polymer chains cleave from hydrolysis, localized areas of weaker

material lead to localized swelling in these areas. In the case of the HA/P specimens, there is nothing to constrain the swelling and thus the blisters can form on a large scale.

As the blisters increase to the size of those shown in Figure 3.5, it is theorized that the blisters are acting as a water reservoir. If this is the case, it is a possible explanation for the jump in mass gain from a value of 62% at day 14 to 84% at day 17. This reservoir concept also accounts for the relatively large standard deviation (~10%) of the day 17 average mass gain, since the size and formation of the blisters are inconsistent between specimens. Additionally, this concept is a possible explanation for the numerous pits present in the HA/P specimens at later stages in the degradation process. It is thought that the pits are caused by the formation of local reservoirs until degradation proceeds to the point where the blisters rupture, leaving behind the pitted surface.

With regard to the HA/P/C specimens, although the carbon foam only occupies about 3% of the total volume of the specimens, it is thought the ligaments serve to constrain the HA/P phase from large-scale swelling, thus the reason no large-scale blisters are observed. In addition, this constraint could also prevent the build-up of the smaller reservoirs at later stages of degradation, thus accounting for the less frequent occurrence of the pits observed in the degraded specimens.

3.4.5 Determination of Diffusion Coefficient

Since the presence of carbon foam changes the water uptake and degradation characteristics of the HA/P, and HA/P/C is the ultimate material system of interest, the water uptake data for the HA/P/C specimens is used in the determination of the diffusion coefficient. Though the water uptake over this initial period of two-three weeks is expected to take place mainly in the PDLGA phase of the material, this analysis assumes the water uptake occurs uniformly across the surface. In this sense, the diffusion coefficient attained is then a homogenized property for the HA/P/C material. Repeating for convenience, Equation 3.9 as derived in Section 3.2 is used to determine the one-dimensional diffusion coefficient D of the material from the experimental mass gain data:

$$\frac{M_t}{M_\infty} = 1 - \sum_{n=0}^{\infty} \frac{8}{(2n+1)^2\pi^2} exp\left[\frac{-D(2n+1)^2\pi^2 t}{4l^2}\right] \qquad \textbf{(3.9)}$$

where t is time, l is specimen half-thickness, M_t is water content at time t, and M_∞ is the water content at fully saturated conditions. A problem that arises in using the above relationship is the determination of M_∞ in bioresorbable polymer systems. In non-degradable polymers that exhibit Fickian water uptake, experiments are run at long-term time periods and the saturated water content (M_∞) is taken to be the value at which absorption plateaus. In bioresorbable polymers, the polymer may begin to dissolve and lose polymer mass before saturation is achieved, thus the saturated water content cannot be determined.

Looking at the mass gain curve for the HA/P/C specimens in Figure 3.4, it is seen that the curve begins to plateau at day 11 and continues to plateau through day 17. The average increase in mass due to water uptake during this time period is 54%. To ensure that this value can be taken to be the saturated water content, M_∞, it is necessary to investigate the mass loss values for this same period. Looking at the mass loss curve for HA/P/C in Figure 3.4, the average ratio of dry mass to initial mass for days 11-17 is 95% (1.4 Std Dev). So over this time period, the specimens lost 5% of their initial mass. Since relatively little dissolution occurred in this time period, it is assumed that the value at which the mass gain curve plateaus is the saturated water content, and thus M_∞ is 0.54 M_o.

Taking M_o to be the average initial mass of all HA/P/C specimens for day 11, 14, and 17, M_o is 122.9 mg and thus M_∞ is 66.4 mg. Since the diffusion coefficient is determined for the early portion of the curve where water uptake dominates, the average half-thickness l of all specimens up to day 17 is 0.41 mm (0.035 Std Dev). Using Excel 2007 to expand Equation 3.9 using 15 terms of n in the summation series, a diffusion coefficient D of 0.015 mm^2/day is found to best represent the experimental data. It should be noted that at a time of 1 day, the 15^{th} term of Equation 3.9 is 1.4e-187, so it is decided that no further terms are necessary. Additionally, as time increases, the series reaches zero faster, so 15 terms is suitable for this analysis. The mass gain curve using the above D is plotted and compared to the HA/P/C experimental data in Figure 3.9.

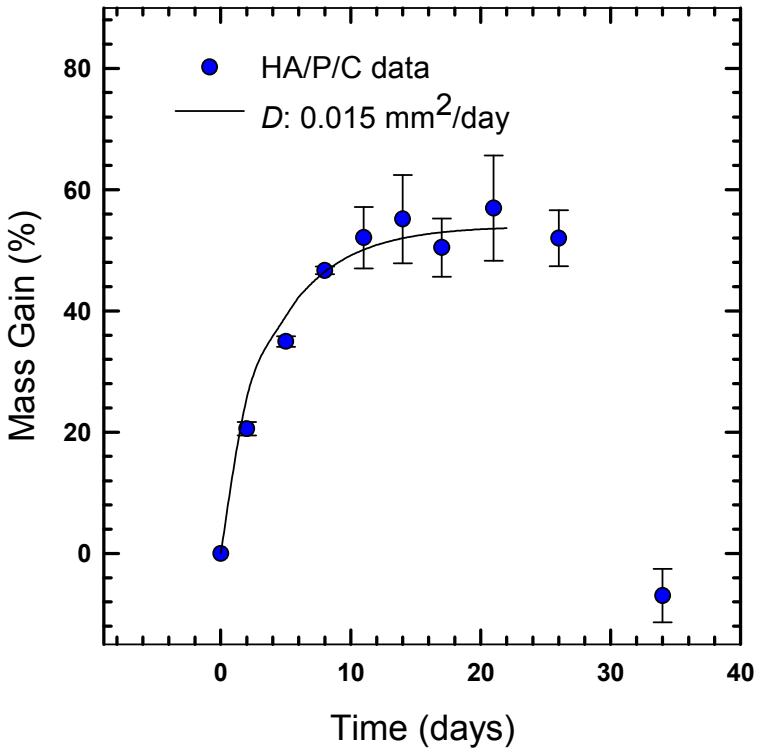

Figure 3.9. Comparison of HA/P/C mass gain data to diffusion equation for water content with D of 0.015 mm^2/day.

3.4.6 Determination of Dissolution Rate

It is of interest to determine the rate at which the cleaved polymer chains are shed from the bulk polymer, referred to here as the dissolution rate. Again, the HA/P/C specimen data is used to determine the dissolution rate since that is the material system of interest. Here, the dissolution rate is calculated and reported as a 1-dimensional change in specimen thickness. Although changes in specimen dimensions were not measured in the experiment, the change in dry mass over time is used to calculate the change in dimensions. In this analysis, it is first assumed that dissolution occurs only through-the-thickness of the specimens. In addition, it is assumed that dissolution occurs uniformly on the exposed surface area. Although the photographs shown in Figure 3.8 show that there are local pinhole areas, it is not known if these pits are a result of non-uniform dissolution or if they are a result of small-scale blisters that ruptured. Lastly, it is assumed that the density of the remaining HA/P/C specimen after degradation and drying is the same as the initial density.

The change in thickness over time is calculated by relating the volume of the dry specimens after degradation to the initial volume of the specimens. Since mass measurements are taken, the volume of the specimens is found by using the density relationship:

$$M = \rho(W \times L \times T) \tag{3.12}$$

Now assuming the density of the dry specimens remain the same before and after degradation and also assuming dissolution only occurs through-the-thickness, Equation 3.12 is rewritten as

$$T_t = \frac{M_{t,d}}{\rho(W \times L)} \quad \textbf{(3.13)}$$

Where T_t is specimen thickness at time t, $M_{t,d}$ is the dry mass at time t, and ρ, W, and L are the initial material density, specimen width and specimen length, respectively.

As noted in Section 3.4.1, some specimens curled in the cutting process, thus care was taken in calculating the density of the HA/P/C specimens. Using the dimensions of two specimens that were not curled from slicing (specimens #1 and #2 from day 8, Table 3.3), the HA/P/C density is calculated to be 1.52 mg/mm^3 (0.001 Std Dev). Since the specimen length measurements given in Table 3.3 are approximations because of the curled geometry in that dimension, it would not be appropriate to apply Equation 3.13 to each individual specimen. Instead, the average mass loss results for which time period is applied to a fictitious specimen that has the average thickness of all specimens and comparable cross-sectional dimensions.

The average half-thickness (l) of all specimens is 0.41 mm (0.04 StdDev), thus the initial thickness of the fictitious specimen is 0.82 mm. The average width and length dimensions are 8.72 mm and 11.2 mm, respectively, and are used in Equation 3.13 to calculate the change in thickness from dissolution at the various time points. Using the density of 1.52 mg/mm^3, the mass of a specimen that is 8.72 mm x 11.2 mm x 0.82 mm is calculated to be 121.73 mg. The mass loss data presented in Figure 3.4 as a dry mass to initial mass ratio is then applied to the fictitious specimen at each time period. The values of the average dry mass/initial mass data for each time period is repeated in Table 3.4. The mass loss data is then used to calculated the mass remaining at time t, $M_{t,d}$ (i.e.

the mass remaining at Day 2 is $M_{2,d}$ = 0.9976 M_i, which is 0.9976*121.7 mg, or 121.44 mg). These values of $M_{t,d}$ are then used in Equation 3.13 to find the resulting thickness T_t (i.e. T_2 is 121.44 mg / (1.52 mg/mm^3 * 11.2 mm * 8.72 mm), or 0.818 mm). Since it is assumed that dissolution is occurring on both faces of the cross-section, the dissolution depth at time t is then taken to be (T_i - T_t) / 2 (i.e dissolution depth at day 2 is (0.82 mm – 0.818 mm)/2, or 0.001 mm). The above is repeated for each time period and

Table 3.4. Data used in determination of dissolution depth at each time period.

	Day								
	2	5	8	11	14	17	21	26	*34*
Average Dry Mass/Initial Mass	99.76	98.94	96.93	96.32	94.95	93.27	89.78	75.60	*53.01*
Dry Mass Remaining $M_{t,d}$ (mg)	121.44	120.44	117.99	117.25	115.58	113.54	109.29	92.03	*64.53*
Resulting Thickness T_t (mm)	0.818	0.811	0.795	0.790	0.779	0.765	0.736	0.620	*0.435*
Dissolution Depth (mm)	0.0010	0.0044	0.0126	0.0151	0.0207	0.0276	0.0419	0.1000	*0.1927*

the corresponding $M_{t,d}$, T_t, and dissolution depths are given in Table 3.4. The dissolution depths up to day 26 as given in Table 3.4 are plotted below in Figure 3.10. The values in Table 3.4 for day 34 are listed in italics to highlight that those values are not used in the determination of the dissolution rate below. This is chosen because at day 34, it is determined that the foam network is the only thing preventing the HA/P from complete break-up, as indicated by the images of the HA/P/C specimens.

It is of interest to determine a 1-dimensional dissolution rate based on this data that can be applied to specimens of other dimensions. As such, it is assumed the dissolution rate is of the exponential form $y = ae^{bt}$, where a and b are determined from experimental data. Using the statistical software SigmaPlot, an a of 0.00135 mm and b of 0.1673 day^{-1} are found to be a best fit (R^2 is 0.9985) for the data. This empirical dissolution rate is plotted for comparison to the experimental data in Figure 3.10.

Although the constants a and b are found only using the data up to day 26, it is interesting to note that the extrapolated dissolution depth at day 34 is 0.399 mm. This indicates that a slab specimen that is 0.798 mm in total thickness would theoretically dissolve entirely. This result is in-line with the assumption that at 34 days, the HA/P/C specimens with 0.82 mm thickness are essentially in a dissolved state.

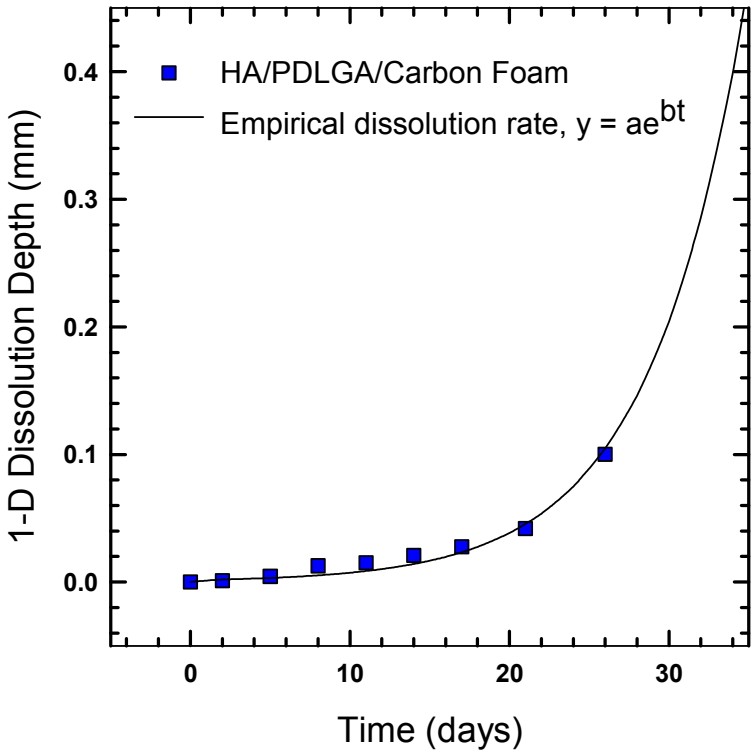

Figure 3.10. Plot of HA/P/C experimental dissolution depth and empirical dissolution rate equation with *a* of 0.00135 mm and *b* of 0.1673 day^{-1}.

3.5 Remarks

The degradation experiments performed in this study demonstrate that the addition of HA to PDLGA significantly alters the water uptake response of the material, as illustrated in Figure 3.2. Whereas the HA/PDLGA material initially exhibits a Fickian water uptake response, the neat PDLGA exhibits a non-Fickian response as well as becomes a gel-like material after 10 days of immersion. The HA/PDLGA material does not exhibit this gel-like state initially, but there was one observed instance after 34 days of degradation where the material did exhibit this quality. Although the HA/PDLGA specimens in the second degradation experiment maintained structural integrity without fracturing, the remaining two day 34 specimens were delicate enough to be fractured upon removal from the experiment.

The addition of carbon foam to the HA/PDLGA material results in a similar initial Fickian water uptake response as the HA/PDLGA material as shown in Figure 3.2 and Figure 3.4a, but the response then deviates once an apparent plateau is reached. While the HA/P/C specimens maintain a relatively stable water uptake level until dissolution begins to dominate the response, the HA/P specimens display a secondary peak in their uptake response in both experiments conducted. This response is explained by the presence of large-scale surface blisters on the HA/P specimens which are hypothesized to act as water reservoirs, resulting in higher water uptake values corresponding to the time points the peaks in the data are observed. These large-scale blisters are not observed on the HA/P/C specimens presumably due to the geometric constraint the foam ligaments cause, preventing the formation of the large blisters.

While the HA/P specimens after 34 days of degradation are delicate enough to be fractured upon handling, the HA/P/C specimens maintained their structure after 34 days. Still, cracks in the HA/P phase are observed in the wet HA/P/C specimens which become more obvious when looking at the specimens after the drying process. It is concluded that although the HA/P/C specimens remained intact at this time point, the state of the HA/P material is such that the network of carbon foam is the only thing preventing the HA/P phase from complete breakup.

A dissolution rate of the HA/P phase in the HA/P/C material system is developed based on mass loss data. In this analysis, dissolution is assumed to occur only through-the-thickness as well as to occur uniformly across the cross-section. This uniformity of dissolution assumption seems to be in-line with what is observed in the images of the degraded HA/P/C specimens. Although the small-scale blisters and subsequent surface pits observed in the HA/P/C specimens violate this assumption in the strictest sense, the scale of these features in comparison to the cross-section is deemed to be small enough to support the assumption.

A diffusion coefficient is also determined for the HA/P phase in the HA/P/C specimens. In this analysis, Fickian diffusion is assumed to occur in one-dimension since the specimens' cross-sectional dimensions are much greater than the thickness. Part of the derivation of the diffusion equations for this experiment involves the major assumption that the diffusion coefficient is constant as well as independent of water concentration. Although it is well-known that polymer swelling, especially on the scale that is observed in these experiments, can lead to a change in the polymer diffusion

coefficient, the water uptake data takes the form of the theoretical equations that are derived with these assumptions. It should be noted that this is not to say these assumptions are not violated since other unknown mechanisms could be occurring in the experiments and the effects of these could be cancelling each other, thus leading to the data that agrees with the assumptions.

With a known diffusion coefficient of the material, the water concentration at any point in the material as a function of time can be determined. Again, this determination is only valid up until the point where dissolution dominates the material response. Although the addition of water to the material system results in changes of mechanical properties, the experiments undertaken here did not investigate this relationship. Since no experiments are conducted to determine this relationship, only the dissolution rate is carried forward in determining the time-dependent properties of a device constructed of the HA/P/C material system.

4. COMPUTATIONAL MODELS TO PREDICT MECHANICAL PROPERTIES OF PROPOSED MATERIAL SYSTEMS

4.1 Overview

This section presents the computational models used to predict the effective mechanical properties of the material systems. First a micromechanics averaging technique, Mori-Tanaka, is used to determine the mechanical effects of the HA particles on the PDLGA polymer phase and is described in Section 4.2. The HA particle is assumed to be an ellipsoidal inclusion that is homogenously distributed in a PDLGA matrix. Results for effective modulus of the HA/PDLGA composite are obtained as a function of HA volume fraction as well as HA particle shape, where analyses are performed assuming the particle is both a perfect sphere and a prolate sphere. In addition, the effective modulus is determined as a function of void content to account for the HA/PDLGA porosity that results from the processing method. All micromechanics analyses are performed only to determine the extent of reinforcement of the HA on the un-degraded, initial elastic PDLGA phase.

Next, finite element (FE) models are created to evaluate the effective mechanical properties of the HA/PDLGA/Carbon Foam material system. The FE models are used to quantify the change in stiffness, predict the strength of the composite system, and study

the changes in load paths resulting from the infiltration of the carbon foam with the HA/PDLGA phase.

In the development of the HA/PDLGA/Carbon Foam FE models, a FE model of carbon foam is first created and is described in Section 4.3. The microstructure of the foam is simulated by modeling the foam ligaments with beam elements in an arrangement of multiple tetrakaidecahedra unit cells to create a Representative Volume Element (RVE) that has a periodic geometry. Ligament geometry, as determined in Section 2.1, is assigned to the beam elements and compressive loads are applied to the RVE under periodic boundary conditions to determine bulk foam stiffness and strength.

This carbon foam FE model is then used as a skeleton for the HA/PDLGA/Carbon Foam FE model, as described in Section 4.4. Here, the infiltrated foam is simulated by embedding the carbon foam RVE in a cube of solid elements that are assigned linear elastic properties of HA/PDLGA as predicted by the micromechanics analysis in Section 4.2. Again, compressive loads and periodic boundary conditions are applied to the FE model to determine the effective stiffness and strength of the HA/PDLGA/Carbon Foam material system.

4.2 Computational Assessment of HA/PDLGA

In addition to the increase in mechanical stiffness, the addition of HA to the bioresorbable polymer results in increased bioactivity resulting in improved osteoconductivity and bone-bonding properties of the composite, enhanced biocompatibility, and delayed degradation of the bioresorbable matrix as previously mentioned. Here the HA/PDLGA composition is based on the mechanical reinforcement aspects that the HA provides. Micromechanics techniques are used to predict the effective stiffness of HA/PDLGA materials based on HA volume fraction.

4.2.1 Micromechanics Analysis for Initial Effective Modulus

Utilizing micromechanics techniques to predict effective stiffness of HA/PDLGA, the material is considered to be a two-phase composite consisting of ellipsoidal particles embedded in a polymer matrix. Although a simple elasticity solution of concentric spheres can be used to predict the effective modulus of the material, this analysis is only valid if the HA particles are perfectly spherical. However, the Mori-Tanaka averaging scheme is used, which allows for the use of ellipsoidal shaped particles. Based on Eshelby's solution of an inclusion embedded in an infinite medium and following the work of Beneviste, the Mori-Tanaka formulation for effective stiffness of a two-phase composite reduces to the following form[56-58]:

$$L = L_m + c_i (L_i - L_m)\underline{A} \tag{4.1}$$

where

$$\underline{A} = \overline{A}\left[c_m I + c_i \overline{A}\right]^{-1} \tag{4.2}$$

and

$$\overline{A} = \left[I + S_m L_m^{-1} \left(L_i - L_m \right) \right]^{-1} \tag{4.3}$$

In this formulation, L is the effective stiffness, and L_m and L_i are the matrix stiffness and inclusion stiffness, respectively. The matrix and inclusion volume fraction is taken into account through the c_m and c_i terms. Additionally, the Eshelby tensor, S_m, is dependent upon the matrix properties (PDLGA) as well as the shape of the inclusion.

In applying the Mori-Tanaka averaging method to determine the effective modulus of HA/PDGLA, it is assumed that there is a perfect between the HA particle and PDLGA matrix, and there is a homogenous distribution of HA particles throughout the PDLGA phase. In addition, it is noted that although the Mori-Tanaka method is formulated for a polydisperse suspension of ellipsoidal inclusions in a matrix, the method provides accurate comparisons to mono-disperse particles at lower volume fractions[59, 60].

Following the work of Entchev and Lagoudas[61], randomly oriented ellipsoids are represented throughout the matrix. In their work, the tensor $\overline{A}$ is found in the local coordinates of the inclusion (as shown in Figure 4.1) and transformed to the global coordinates using the following relation:

$$\overline{A}_{global_{ijkl}} = Q_{mi} Q_{nj} \overline{A}_{local_{mnpq}} Q_{pk} Q_{ql} \tag{4.4}$$

In the above, Q is the rotation tensor relating the local and global coordinate systems and is expanded as:

$$Q = \begin{bmatrix} \sin\theta\cos\varphi & -\cos\theta\cos\varphi & \sin\varphi \\ \sin\theta\sin\varphi & -\cos\theta\sin\varphi & -\cos\varphi \\ \cos\theta & \sin\theta & 0 \end{bmatrix} \tag{4.5}$$

The random orientation of the ellipsoid inclusions is then achieved through the following:

$$\left\{\left\{\overline{A}\right\}\right\} = \frac{c_i}{4\pi}\int_0^{\pi}\int_0^{2\pi} \overline{A}_{global} \sin\vartheta d\varphi d\vartheta \,. \tag{4.6}$$

The relationship for effective stiffness in Equation 4.1 is then rewritten as:

$$L = L_m + \left(L_i - L_m\right)\left\{\left\{\overline{A}\right\}\right\}\left[c_m I + \left\{\left\{\overline{A}\right\}\right\}\right]^{-1} . \tag{4.7}$$

It should be noted that special attention is required in defining the local coordinate system as well as expanding and contracting the tensor $\overline{A}$ from a 6x6 matrix to a 3x3x3x3 fourth order tensor and vice versa. In addition, due to the randomly oriented ellipsoidal inclusions, the effective properties become isotropic.

The ellipsoidal inclusion shape investigated is a prolated sphere where a_1=2a_2 and a_2=a_3. The modulus of the HA and PDLGA are assumed to those reported by the manufacturers, 80 GPa and 1.3 GPa, respectively. Additionally, the Poisson's ratio is assumed to be 0.25 for both HA and PDLGA. All micromechanics computations are implemented in MATLAB V.6.5.

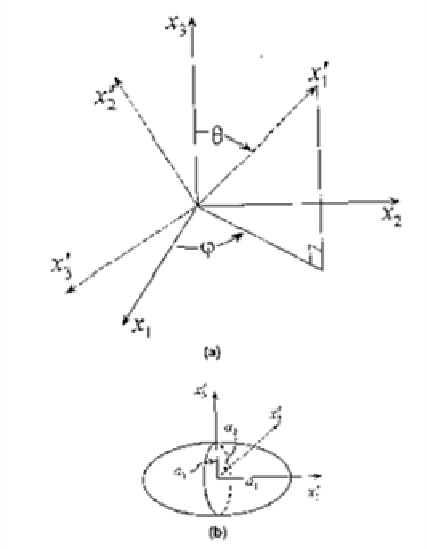

Figure 4.1. a) Relation between global and local coordinate system b) Ellipsoidal inhomogeneity with principal axis in the local coordinate system (as scanned from Entchev and Lagoudas[61]).

Additionally, the impact of void content on effective modulus of the HA/PDLGA system is investigated. The voids are assumed to be spherical inclusions that are randomly distributed throughout a HA/PDLGA matrix. The matrix properties assigned are those that are found in the HA/PDLGA analysis for a specific HA content and the voids are assigned zero mechanical properties.

4.2.2 Effective Modulus Results and Discussion

The effective modulus E^* for PDLGA filled with homogenously distributed HA particles is plotted in Figure 4.2 as a function of HA volume fraction. Results are plotted for analyses assuming the HA particles are spherical or ellipsoidal which are randomly distributed. In addition, analyses are performed assuming the modulus of PDLGA is 1.3 GPa as well as 3.0 GPa to determine the effect of matrix modulus on the effective stiffness.

First it is important to note that at zero HA volume fraction the effective moduli of the material systems are the moduli of the polymers, 1.3 GPa and 3.0 GPa. Similarly at 100% HA volume fraction, the effective moduli of the systems are those of HA, 80 GPa. The effective modulus in all analyses varies non-linearly with HA volume fraction, a vast departure from a simple rules-of-mixtures estimate, where the effective modulus is a linear combination of HA and PDLGA based on volume fraction. Also note that although results are plotted for particle volume fractions up to 1.0, the physical limit for monodisperse particles is approximately 0.70 dependent upon the packing arrangement.

In comparing the effective modulus results for randomly distributed ellipsoidal particles and spherical particles for the case where the modulus of PDLGA is 1.3 GPa, it is seen that the ellipsoidal analysis yields results 0.45% to 3.79% greater than that of the spherical analysis depending upon the HA volume fraction. For example, at a volume fraction of 0.20, the effective modulus is 1.9251 GPa for the spherical analysis, and 1.9561 GPa for the ellipsoidal analysis, a difference of 1.58%. The range of difference between the results of the spherical and ellipsoidal analyses for PDLGA of 3.0 GPa

modulus is 0.39% to 2.99%. At a HA volume fraction of 0.20, the percent difference is 1.36% (4.3687 GPa versus 4.4291 GPa for the spherical and ellipsoidal cases, respectively).

Since the relative difference between the effective modulus of spherical and random ellipsoidal analyses is small, especially at the lower end of the HA volume fraction spectrum, it is deemed that the spherical particle assumption is sufficient for future analyses. This assumption significantly reduces the level of computational complexity and time in the contraction, transformation and expansion of the fourth-order tensor $\overline{A}$ that is required for the ellipsoidal analysis, as given in Equations 4.4 - 4.7.

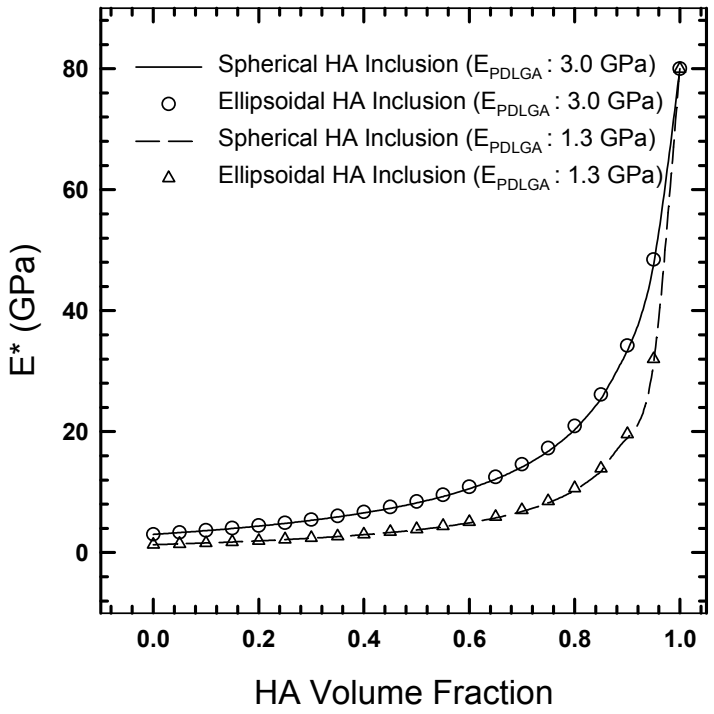

Figure 4.2. Effective modulus, *E**, for HA/PDLGA as a function of HA volume fraction.

The effective modulus of HA/PDLGA as a function of HA volume fraction is shown in Figure 4.3a for a spherical-inclusion analysis. In addition to the modulus of PDLGA taken to be the reported value of 1.3 GPa, the effects of moduli of 0.7 GPa, 2.0 GPa, and 3.0 GPa are studied. Plotted in Figure 4.3b are the results for a HA volume fraction range of 0.0 to 0.40 where the results are easier to discern. Table 4.1 contains values for the effective stiffness for each of the PDLGA moduli composites with HA volume fractions of 0.15 and 0.25.

At a volume fraction of 0.15, the systems with PDLGA modulus of 0.7, 1.3, 2.0, and 3.0 GPa are result in E^* of 0.94, 1.74, 2.67, and 3.97 GPa, respectively. These represent an increase of 34.6%, 34.0%, 33.7%, and 33.3% from the original PDLGA moduli. Note that as the mismatch in modulus between HA and PDLGA increases, the ratio of E_{PDLGA} to E^* increases as well. This is more evident at higher HA volume fractions, for example, at 0.25 the E^* are 1.16, 2.13, 3.25, and 4.82 GPa, an increase of 65.2%, 63.9%, 62.5%, and 60.5%, respectively.

Table 4.1. Effective stiffness of HA/PDLGA for HA volume fractions of 0.15 and 0.25. The effective stiffness is determined for systems where the modulus of PDLGA is 0.7, 1.3, 2.0 and 3.0 GPa.

E_{PDLGA} (GPA)	Effective Stiffness (GPa)			
	HA v_f: 0.15	% Increase Relative to E_{PDLGA}	HA v_f: 0.25	% Increase Relative to E_{PDLGA}
0.70	0.94	34.6 %	1.16	65.2 %
1.30	1.74	34.0 %	2.13	63.9 %
2.00	2.67	33.7 %	3.25	62.5 %
3.00	3.97	33.3 %	4.82	60.5 %

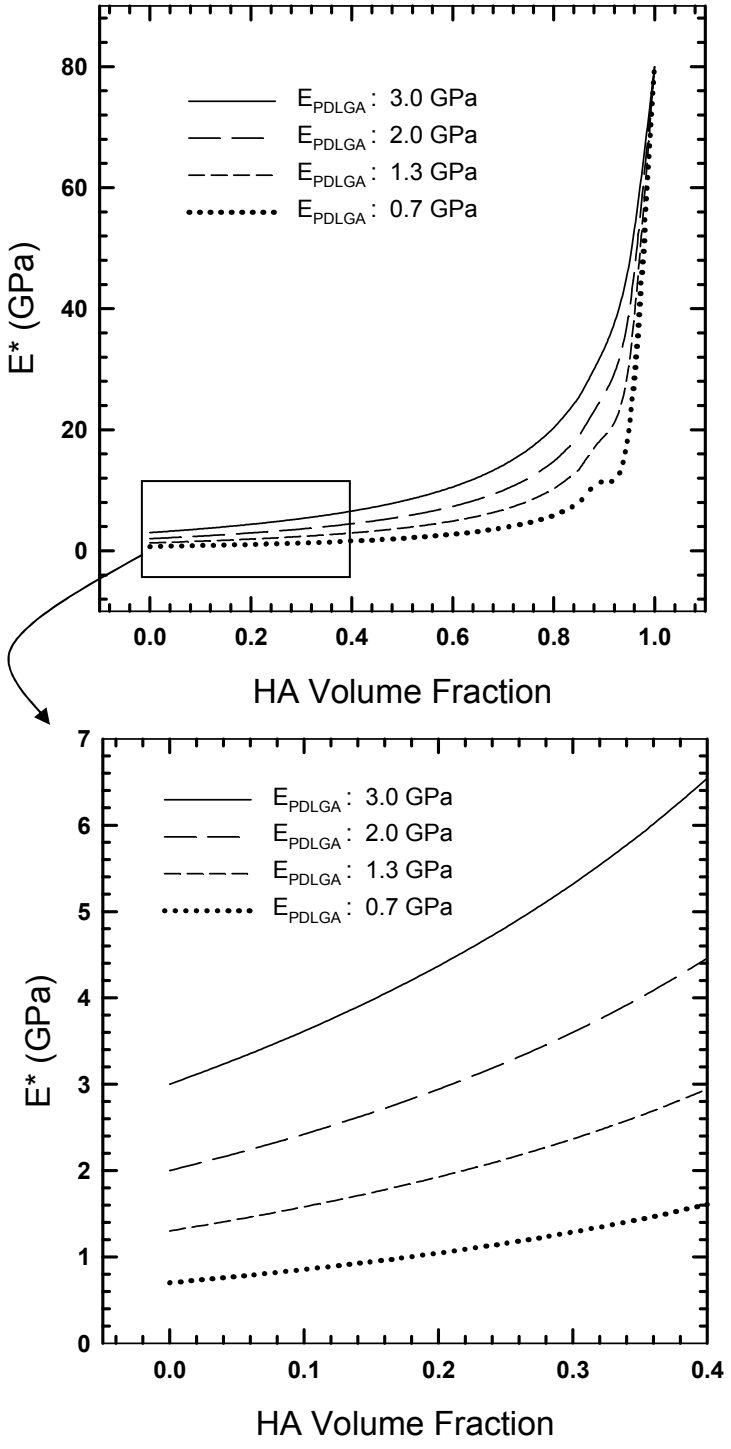

Figure 4.3. Effective modulus, *E**, of HA/PDLGA for polymers of various moduli: a) full HA volume fraction range, b) HA volume fraction range: 0.0 to 0.4.

Figure 4.4 shows the effect of void content on the effective modulus of the various HA/PDLGA systems with 15% HA volume fraction. First note that at zero void content, the various *E** are those shown in Figure 4.3b at a volume fraction of 0.15. Effective modulus decreases non-linearly with increasing void content, which is expected. The effective modulus of each system is reduced by 9.5% if the void content is 5%. For

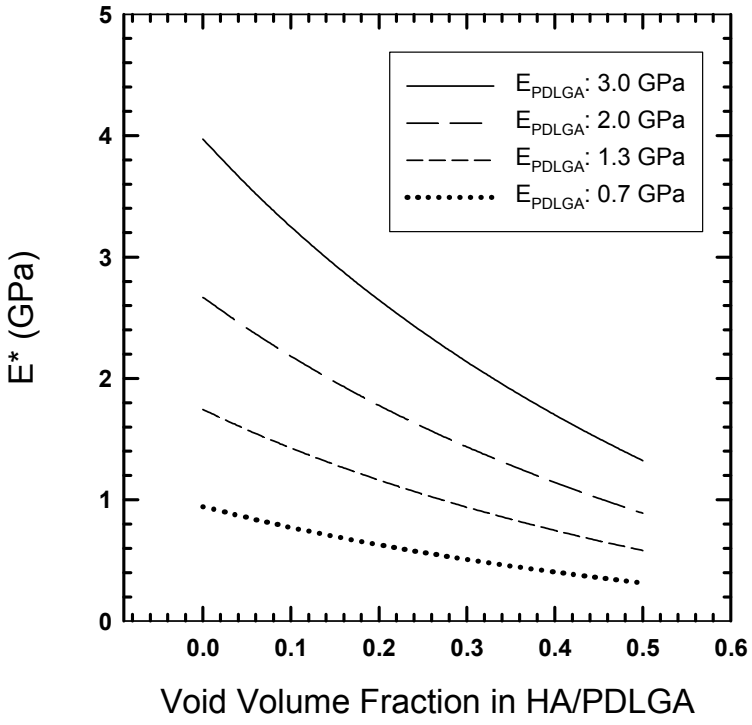

Figure 4.4. Effect of void content on a HA/PDLGA system with 15% HA volume fraction relative to PDLGA.

example the E^* of the HA/PDLGA (E_{PDLGA} = 1.3 GPa) system drops from 1.74 GPa at zero void content to 1.58 GPa at a void volume fraction of 0.05. If the void content of the HA/PDLGA systems increases to 10%, the effective modulus of each system further reduces to about 18.2 % of its original value.

4.2.3 Remarks

As shown the addition of HA particles in PDGLA results in an increase of effective modulus for the system. The improvement in HA/PDLGA modulus as compared to the original PDLGA moduli investigated is about 33-34% for a HA volume fraction of 15%, and 61-65% for a HA volume fraction of 25%. Again, the exact value for relative improvement is dependent on the initial starting value of the PDLGA modulus, thus the reason for a reported range of improvement. Using the reported value of E_{PDLGA} of 1.3 GPa and E_{HA} of 80 GPa, a HA/PDLGA system with 15% HA particles by volume is predicted to have an effective modulus of 1.74 GPa.

These above values of effective modulus of HA/PDGLA are as predicted assuming the HA particles are perfectly spherical particles. If the HA particles are slightly

elongated (prolated sphere: $a_1=2a_2$ and $a_2=a_3$) and randomly distributed, the effective modulus results are predicted to be slightly greater than the spherical particle analysis (~1.5% greater for the case E_{PDLGA} = 1.3 GPa and HA content of 15%). This result is physically intuitive because of the increase of aspect ratio as the particles become more elongated.

It is also shown that the presence of voids in the HA/PDLGA system reduces the effective modulus significantly (almost 10% for a material with 5% void content by volume). This finding is significant in that the processing technique developed for the HA/PDLGA system must ensure a minimum level of voids.

Additionally, it must be stated that all the values reported for effective modulus assume a perfect interface between HA particle and PDLGA matrix as well as homogenous distribution of HA particles. Any imperfections present would negatively impact both modulus and strength values for the material systems. In this case, the micromechanics averaging technique used is limited to perfect interfaces.

4.3 FE Simulation of Carbon Foam Microstructure

In designing the HA/PDLGA/Carbon foam material system, it is necessary to determine the effects of carbon foam structure on the overall response of the composite material. Although empirical formulas and closed-form solutions exist to predict the stiffness of open cell foams, there is no straight-forward solution to a foam infiltrated with another material. As such, finite element models are used to quantify the change in stiffness resulting from the addition of carbon foam. The models simulate a two-phase composite where the foam microstructure is modeled where the voids are filled with HA/PDLGA. The modeling approach is as follows: the foam microstructure is assumed to be tetrakaidecahedral and a representative volume element (RVE) is modeled with beam elements using the commercially available finite element package ABAQUS; an effective modulus of the RVE in uniaxial compression is compared to values in literature for model validation; the infiltrated foam is then simulated by embedding the RVE in solid elements with the properties of the HA/PDLGA composite.

4.3.1 Tetrakaidecahedra Unit Cell and RVE

The carbon foam microstructure is assumed to be comprised of periodic tetrakaidecahedra unit cells, as done elsewhere in the literature[43, 62-64]. The tetrakaidecahedra cell, informally known as the Kelvin cell, consists of 36 struts arranged in 6 planar quadrilateral faces and 8 hexagonal faces, as shown in Figure 4.5.

Although most work on FE models of foam takes advantage of periodicity conditions and only model a single unit with appropriate periodicity applied, an alternate approach is taken here. As done elsewhere[65], the RVE in this study consists of a cube

of 2x2x2 tetrakaidecahedrons with periodic conditions applied to shared boundaries. An illustration of the RVE is shown in Figure 4.5. Although this approach is more computationally expensive because of the increased number of ligaments in the model, it is chosen to avoid boundary condition effects on the ligaments' stress state.

4.3.2 Mesh Creation and Element Properties

The ligaments of the carbon foam are assumed to be arranged in a tetrakaidecahedral structure with a ligament length of 800 μm. A tetrakaidecahedral cell is created using the beam element B32, which is a quadratic element with three nodes and 17 integration points in the cross-section with the following degrees-of-freedom: u_x u_y u_z φ_x φ_y φ_z. A cube of foam is then modeled by creating a RVE of 2x2x2 tetrakaidecahedral cells, as shown in Figure 4.5. There are a total of 240 ligaments in the RVE; each ligament is comprised of 5 beam elements, for a total of 1200 B32 elements. A ligament length of 800 μm results in a RVE of 4.5248 mm x 4.5248 mm x 4.5248 mm.

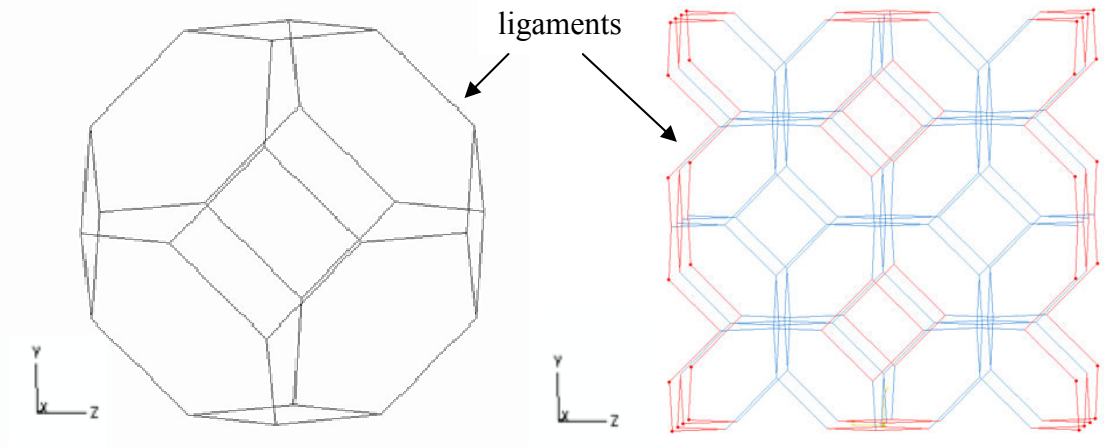

Figure 4.5. Illustration of tetrakaidecahedral cell and RVE composed of 2x2x2 cells. A ligament length of 800 μm results in a RVE that is $(4.5248 \text{ mm})^3$. Ligaments highlighted in red on the RVE represent the 96 ligaments shared with adjacent cells. Both of these illustrations are viewed from a slight angle from the normal of the y-z plane.

As shown in Figure 2.3 in the investigation of the carbon foam, the cross-section is plateau-shaped. Since this geometry is uncommon and therefore not a predefined shape in ABAQUS, the ligament cross-sectional geometric properties are directly assigned to the beam elements. The cross-sectional area A, moments of inertia about the local 2 and 3 axes (I_2 and I_3) and torsional rigidity J are calculated as shown in Figure 4.6 for ligaments with complete cross-sections.

Additionally, it is necessary to model specific elements in the RVE with half cross-sections because of the nature of the periodic RVE. In the RVE shown in Figure 4.5, the ligaments highlighted in red are on the ±x, ±y, and ± z surfaces and are shared with the adjacent cells that are not modeled. Including these ligaments with full cross-sections would result in an RVE with a higher relative density (ρ^*/ρ_s) and a higher

effective modulus than a unit cell with periodic boundary conditions. As such, those shared ligaments (96 of 240) are assigned a half cross-section where the properties are determined using the relationships given in Figure 4.6. In addition, the cross-sections are oriented such that the -2-direction of the local axis in Figure 4.6 aligns with the + y component of the axis in Figure 4.5.

Linear elastic and isotropic properties of carbon (E of 15610 MPa and ν of 0.33) are assigned to the ligaments. These properties are used elsewhere in the literature[66] with the reasoning that those values are similar to the transverse properties of a AS4 carbon fiber; that same approach is adopted.

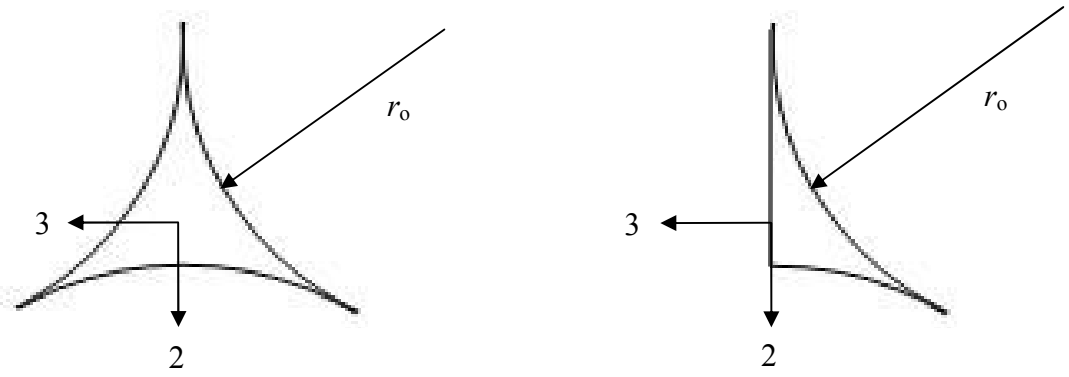

Full-Ligaments

$$A = \left(\sqrt{3} - \frac{\pi}{2}\right) r_o^2$$

$$I_2 = I_3 = \frac{1}{24}\left(20\sqrt{3} - 11\pi\right) r_o^4$$

$$J = 0.0021\, r_o^4$$

Half-Ligaments

$$A = \frac{1}{2}\left(\sqrt{3} - \frac{\pi}{2}\right) r_o^2$$

$$I_2 = I_3 = \frac{1}{48}\left(20\sqrt{3} - 11\pi\right) r_o^4$$

$$J = 0.00105\, r_o^4$$

Figure 4.6. Illustration of full- and half-ligament cross-sections and the corresponding geometric properties assigned to the beam elements.

4.3.3 Boundary and Loading Conditions

As illustrated in Figure 4.7, the nodes that are on –y plane of the RVE are constrained in the y-direction. A single point is also constrained in the x- and z-directions as well for computational stability. A displacement of 0.045248 mm (1% strain) is applied to all nodes on the +y surface as shown in Figure 4.7; they are displaced an equal magnitude in the negative y-direction.

Periodic boundary conditions are applied to the RVE by creating two opposing pairs of surface sets located on the ±z-planes and the ± x-planes (the planes of the RVE that are shared between adjacent RVEs). All nodes located on these surfaces are constrained to displace the same magnitude as the nodes on the opposing surface. This is accomplished in ABAQUS by creating four master nodes all at the same point (in this case, the origin) and using the *EQUATION option to equate the motion on opposite faces relative to the master node. If the displacements of the nodes on the + z-plane are $u_{3,+z}$ and the displacements on the – z-plane are $u_{3,-z}$, then the nodal constraints equations are written as:

$$u_{3,+z} - u_{ref,1} = 0$$
$$u_{3,-z} - u_{ref,2} = 0 \qquad \textbf{(4.8)}$$

where $u_{\text{ref},1}$ and $u_{\text{ref},2}$ are the displacements of the master nodes. Since the master nodes have the same displacements, $u_{\text{ref},1} = u_{\text{ref},2}$, then the magnitudes on both planes are equal.

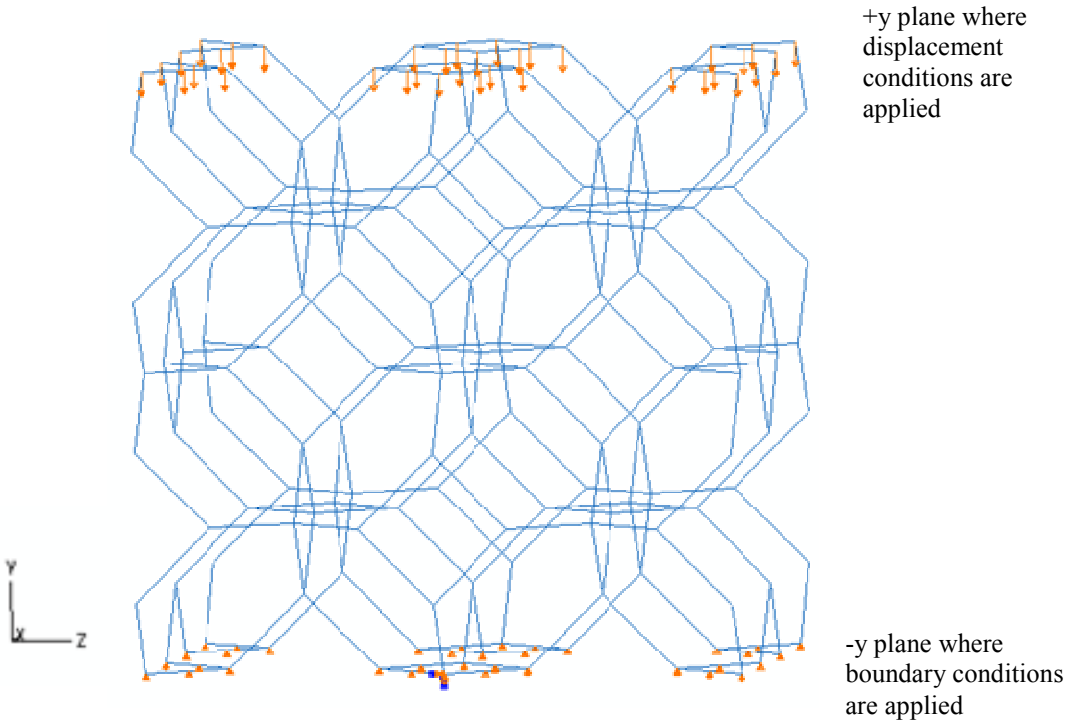

Figure 4.7. Illustration showing application of displacements and boundary conditions on the RVE.

4.3.4 Homogenization Technique to Compute Effective Modulus

The average strain theorem is utilized to calculate the effective modulus E_y^* as follows:

$$E_y^* = \frac{\bar{\sigma}_y}{\bar{\varepsilon}_y} = \frac{P^* L}{A\delta_y} \tag{4.9}$$

Here, the average strain $\bar{\varepsilon}_y$ is calculated using δ_y/L where δ_y is the prescribed boundary condition of 0.045248 mm and L is 4.5248 mm. The average stress $\bar{\sigma}_y$ resulting from the displacement boundary condition is found using a P^*/A relation where A is the cross-sectional area, and P^* is the sum of all nodal reaction forces.

4.3.5 Effective Modulus and Deformation Results

When applying a 1% strain to the RVE in the – y-direction, the summation of the resultant nodal reaction forces on the + y-surface leads to -7.50767 N. With a cross-sectional area of $(4.5248\ \text{mm})^2$ and an applied strain of 0.01, the homogenized modulus E_y^* is calculated to be *36.67 MPa* using Equation 4.9. The normalized effective modulus E_y^*/E is then 0.235% (36.67 MPa/15610 MPa).

The translation in the y-direction of the carbon foam model are shown in Figure 4.8. In this contour plot, the displacements are plotted on the deformed shape of the RVE; the deformations are 20x the actual value and are exaggerated to visually represent the deformation trend. First note that the displacement of the ligaments located on the +y-surface is -0.0045248 mm, which reflects the applied displacement. Also note that ligaments that are not in the z-x plane, such as those indicated by arrows in Figure 4.8, undergo bending deformations. This bending deformation is expected because of the bending moments in these ligaments arising from the yy-loading, as noted by others in the literature[62, 67].

The translations in the x- and z-directions are shown in Figure 4.9. Note the total expansion in the z-direction is 0.02 mm and occurs uniformly throughout a given x-y plane. The same total expansion of 0.02 mm occurs in the x-direction as well. These x- and z-expansion values are used to calculate the effective Poisson's ratios υ_{yx}^* and υ_{yz}^* using the relationships of $-\bar{\varepsilon}_y/\bar{\varepsilon}_x$ and $-\bar{\varepsilon}_y/\bar{\varepsilon}_z$, respectively, where average strains are used. The values of both υ_{yx}^* and υ_{yz}^* are calculated to be 0.44.

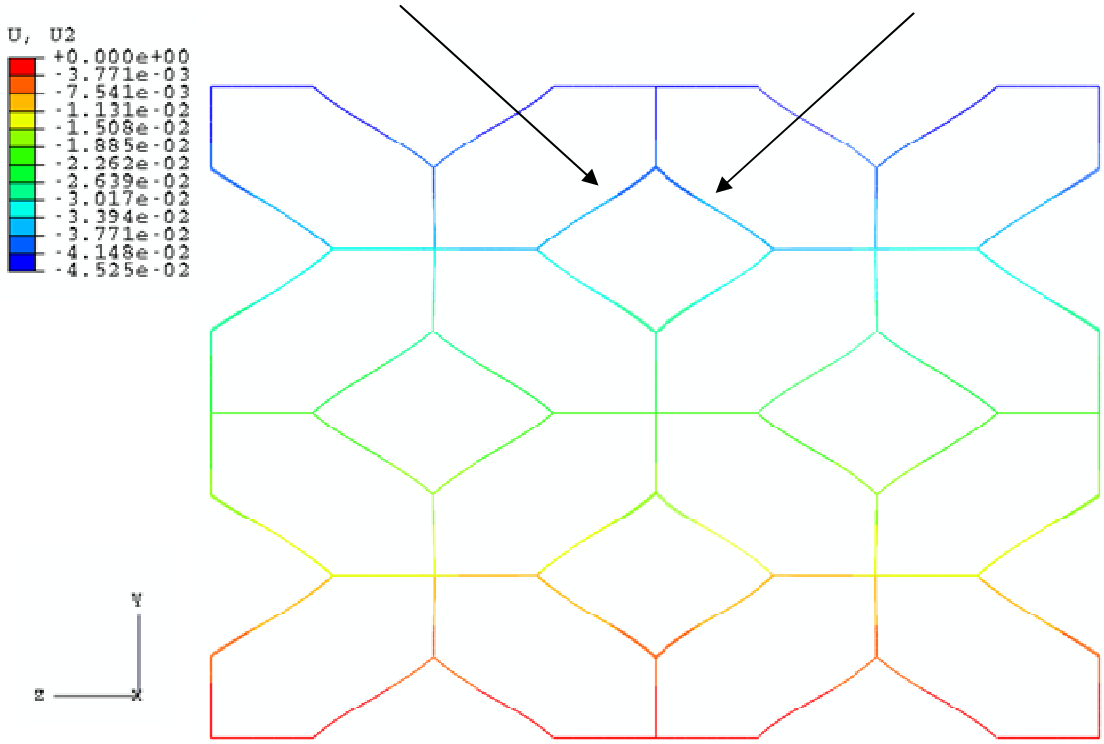

Figure 4.8. Displacements (mm) in the 2-direction (y-direction) shown on a deformed plot (20x actual deformation). Arrows indicate ligaments that undergo bending.

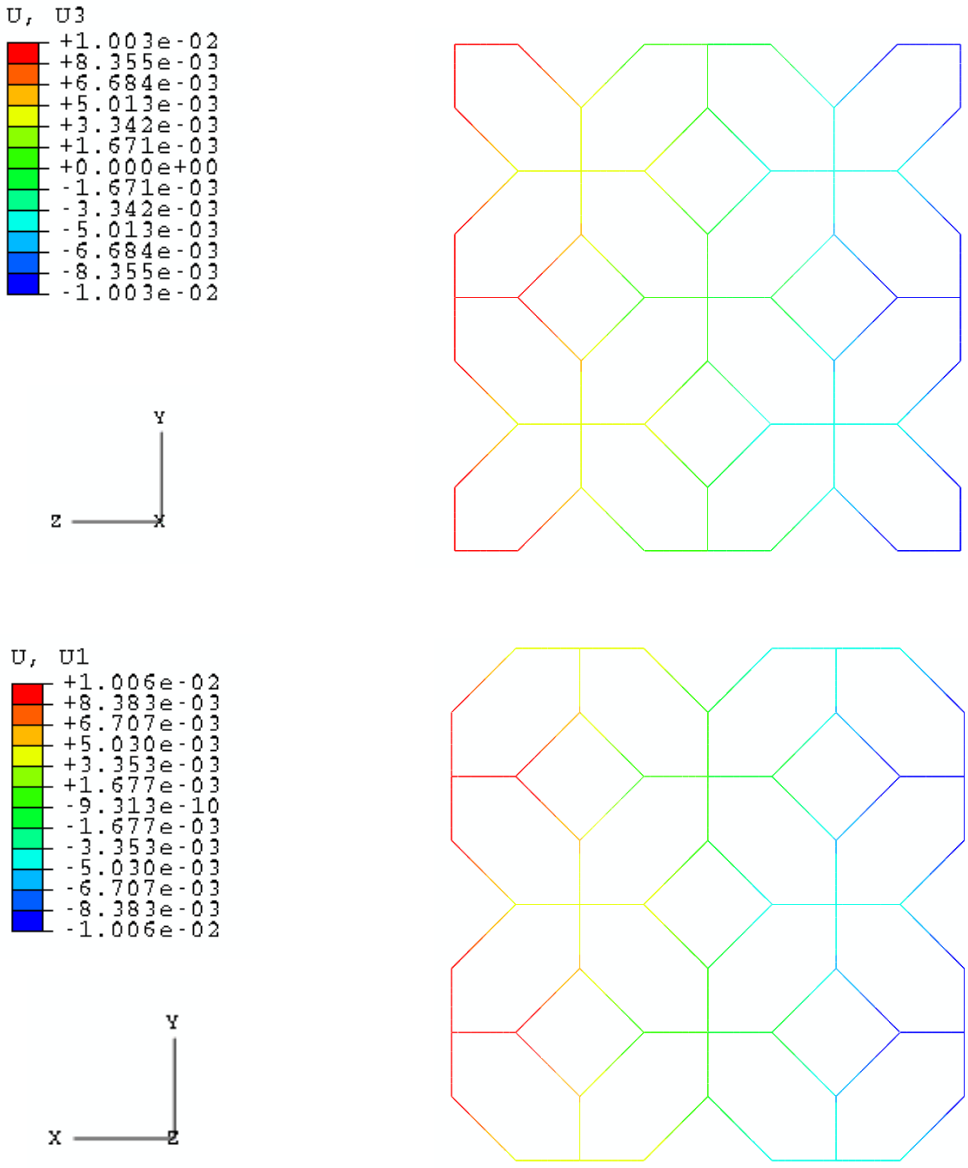

Figure 4.9. Contour plot of the x- and z-translations (mm). As can be seen, the total expansion values in the z- and x-directions are approximately the same, 0.02 mm.

4.3.6 Stress Distribution in Carbon Foam

The axial stress distribution at different points in the cross-sections of the beam elements are shown Figures 4.10-12. The contour plot shown in Figure 4.10 illustrates the stress distribution at the neutral axis of the cross-section; because these stresses occur at the neutral axis, the results reflect the P/A component of the axial stress. In this case, the maximum compressive stress of 11 MPa occurs in the ligaments that are aligned in the y-direction. This result is expected since global displacement is applied in the –y-direction. In addition, tensile stresses arise in the ligaments in the x-z plane as a result of Poisson's effects; the maximum tensile stress occurring is 1.3 MPa.

The contour plot in Figure 4.11 shows the axial stress distribution at the upper-most point in the cross-section; this location is shown in the inset in the figure. At this location, stresses from moments are contributing to the total value of axial stress, so both P/A and My/I components are reflected in the values. As highlighted by the arrows, the maximum stress values occur in the ligaments that are aligned with the loading direction. The maximum stresses are 192 MPa in tension and 214 MPa in compression. The difference in these two values is attributed to the P/A component in those ligaments (-11 MPa).

The contour plot in Figure 4.12 shows the axial stress distribution at the left-most point in the cross-section; this location is shown in the inset in the figure. Again the maximum values occur in the same ligaments where the previous maximums occur. The maximum tensile stress at this location in the cross-section is 221 MPa and the maximum compressive stress is 237 MPa.

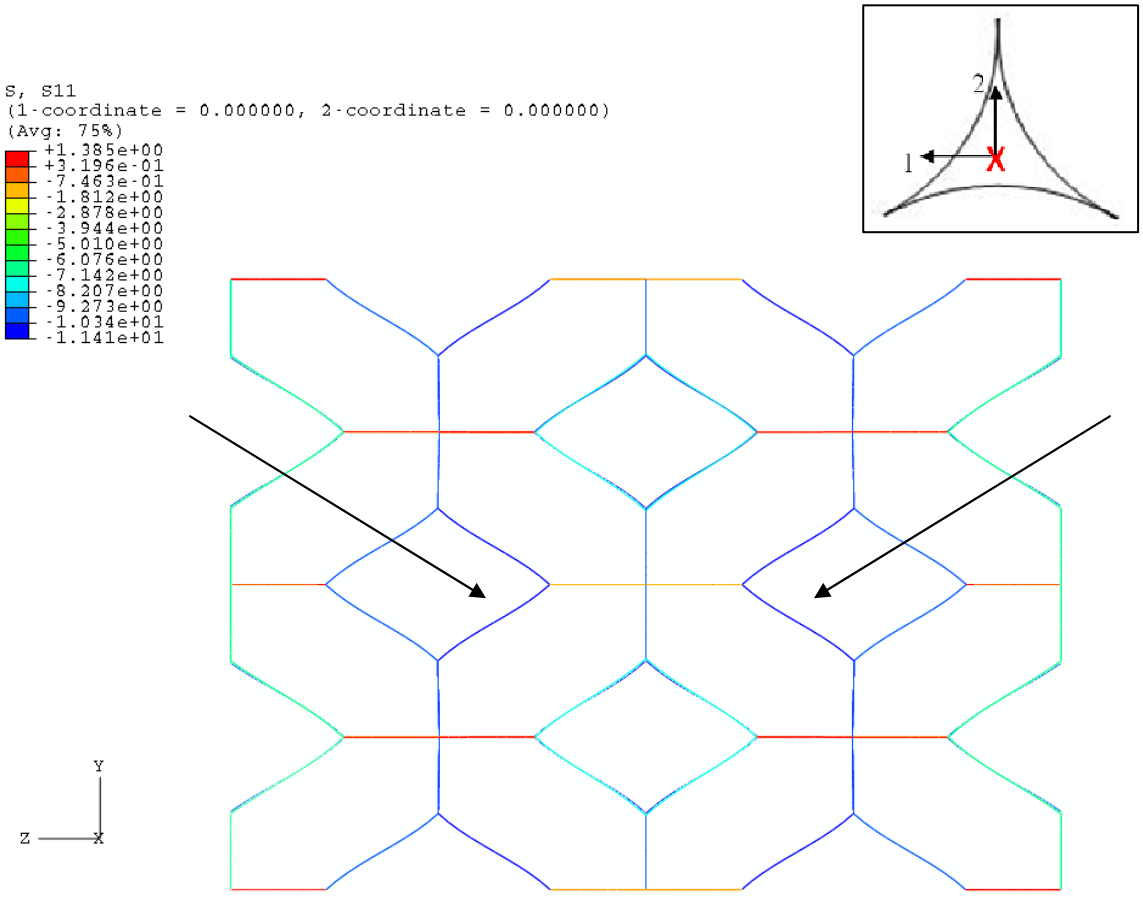

Figure 4.10. Contour plot of the axial stress (MPa) in the ligaments occurring at the neutral axis of the ligament cross-section (as shown in the inset). The maximum tensile stress is *1.4 MPa* whereas the maximum compressive stress is *11 MPa*, occurring in the ligaments highlighted by the arrows. (Contours are plotted on deformed shape with 20x scale).

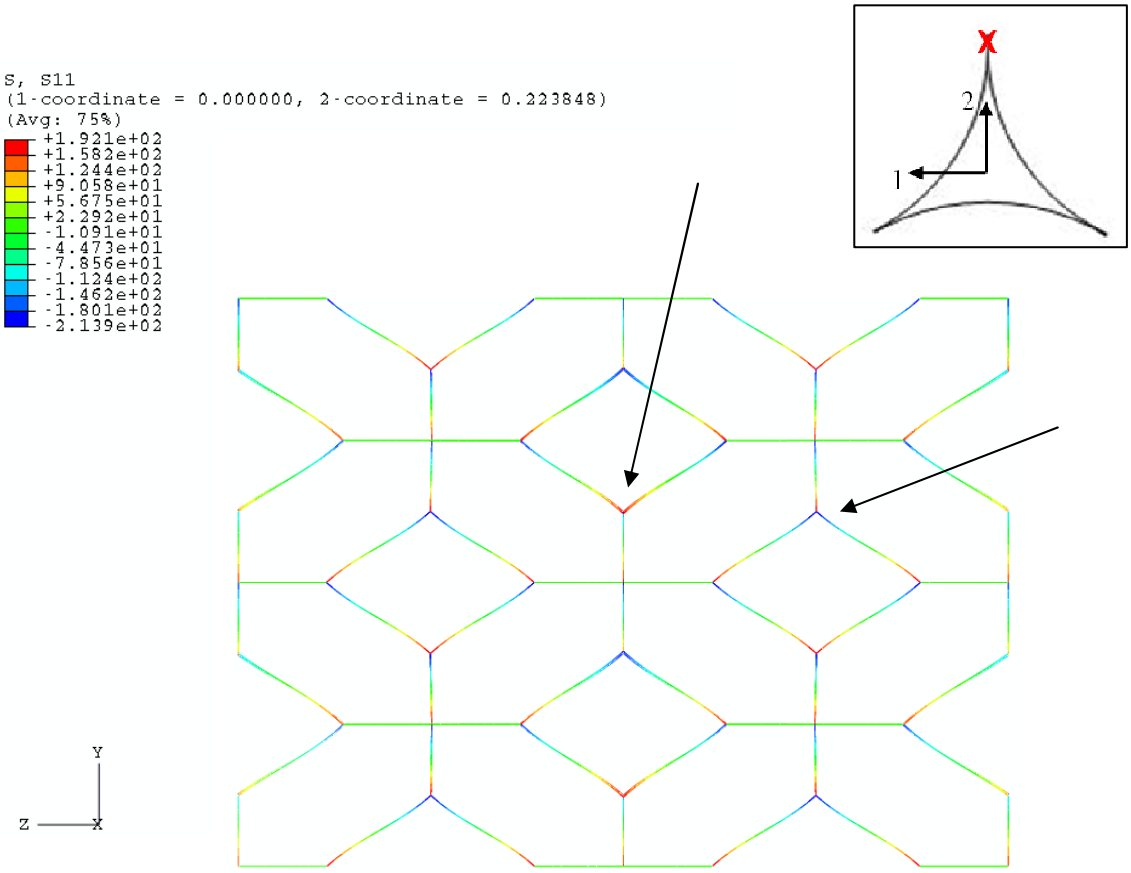

Figure 4.11. Contour plot of the axial stress (MPa) in the ligaments occurring at the point in the cross-section highlighted by the red x in the inset. The maximum tensile stress is *192 MPa* whereas the maximum compressive stress is *214 MPa*, occurring in the ligaments highlighted by the arrows. (Contours are plotted on deformed shape with 20x scale).

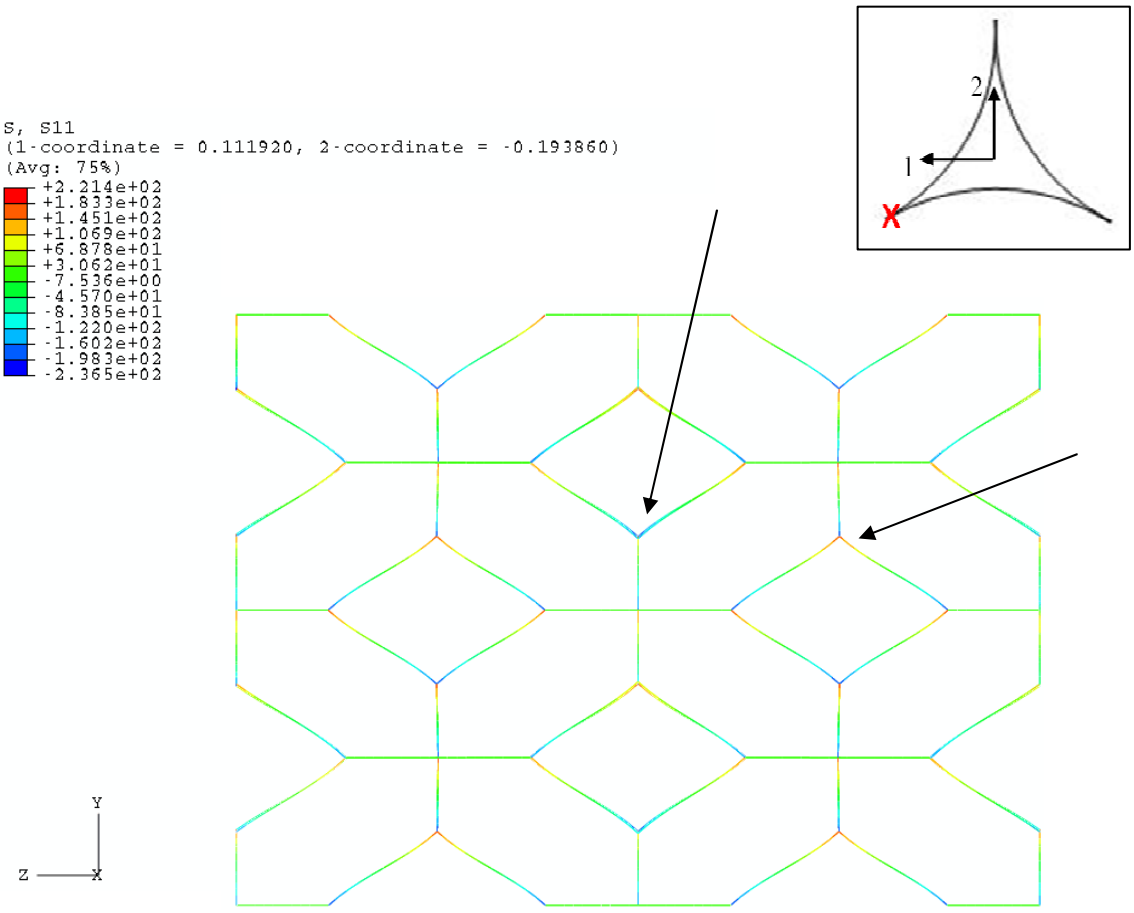

Figure 4.12. Contour plot of the axial stress in the ligaments occurring at the point in the cross-section highlighted by the red x in the inset. The maximum tensile stress is *221 MPa* whereas the maximum compressive stress is *237 MPa*, occurring in the ligaments highlighted by the arrows. (Contours are plotted on deformed shape with 20x scale).

4.3.7 Strength of Bulk Carbon Foam

Although the ligament properties of the carbon foam is unknown, the strength of the solid carbon is assumed to be the strength of reticulated vitreous carbon: 210 MPa tensile strength, and 690 MPa compressive strength[68]. The global compressive strain of 1% resulted in maximum tensile stresses of 221 MPa and compressive stresses of 237 MPa in the ligaments. Both of these maximums occur as a result of the bending component of the axial stress. Because these the allowable tensile strength is exceeded as a result of the 1% global strain, this global strain value is considered the allowable for the bulk foam. Because of the isotropic material properties and the symmetry involved in the RVE structure, the allowable is assumed to be approximately the same in any direction of loading, as well as the value for both tensile and compressive loads.

4.4 FE Simulation of HA/PDLGA/Carbon Foam

The HA/PDLGA/Carbon Foam is modeled with FE by embedding the foam RVE comprised of beam elements in a cube of solid elements that are assigned linear elastic properties of HA/PDLGA. This model is accomplished by taking advantage of embedded elements in ABAQUS. The HA/PDLGA/Carbon foam model is described, including the boundary and loading conditions and homogenization technique used to assess effective modulus. Additionally, the FE model is used to predict the strength of the composite system as well as study the changes in load paths resulting from the addition of the carbon foam to the HA/PDLGA phase.

4.4.1 Embedded Elements

Embedded elements are a kinematic constraint that can be applied through ABAQUS, where a set of elements can be embedded within another set of host elements. In this process, as described in the ABAQUS Analysis User's Manual, the translational degrees of freedom of the nodes of the embedded elements are eliminated by constraining them to the interpolated values of the degrees of freedom of the host element[69].

4.4.2 Mesh and Element Properties

The HA/PDLGA/Carbon Foam is modeled in by embedding the foam RVE described in Section 2.4.1 in a cube of solid elements that are assigned linear elastic properties of HA/PDLGA. Again using a single ligament length of 800 μm, the dimensions of the RVE and solid cube are both 4.5248 mm x 4.5248 mm x 4.5248 mm. As shown in Figure 4.13, the cube geometry completely encases the foam RVE and is first meshed with 1000 C3D20R solid elements, which is a 20-noded quadratic brick element with 8 integration points.

The properties assigned to the solid elements that represent the HA/PDLGA phase are those that are determined from the micromechanics analysis in Section 4.2.2. In this case, the properties are for a HA/PDLGA system with 15% HA v_f in the polymer phase as well as 5% void content in the entire material. This effective stiffness is determined to be 1580 MPa, as shown in Figure 4.8.

Meanwhile, the ligaments are simulated with 1200 B32 beam elements, a three-noded quadratic element and 17 integration points in the cross-section. The linear elastic and isotropic properties of carbon (E of 15610 MPa and ν of 0.33) are assigned to the ligaments as done in the previous carbon foam model in Section 4.3. The beam elements are computationally constrained in the solid elements through the use of the embedded option in ABAQUS, where the beam elements are defined as embedded elements and the solid elements act as host elements. It should be noted that in constraining the nodes of the beam elements to the interpolated values of the solid elements in this way, the beam elements will deform in a manner as if they were perfectly bonded to the solid elements. Thus, this FE model assumes perfect interfaces between the foam and the HA/PDLGA.

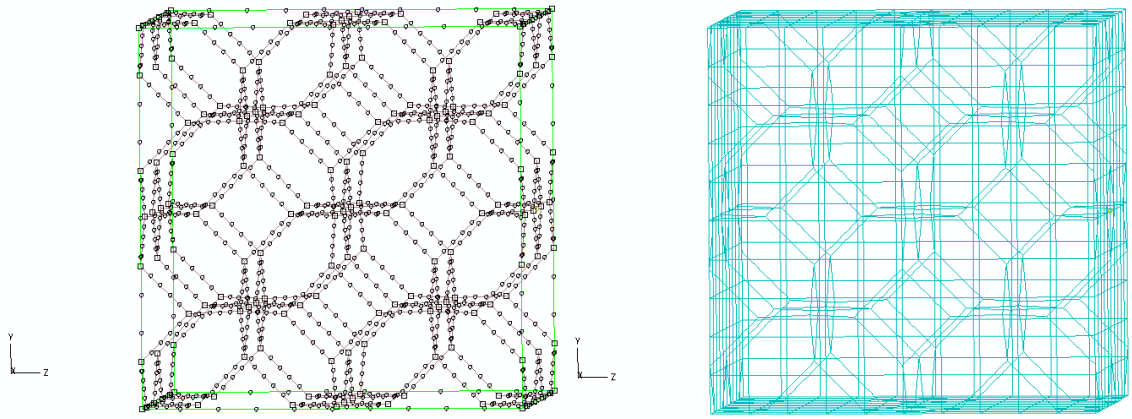

Figure 4.13. Illustration of foam RVE embedded in cube of solid elements that represent the HA/PDLGA.

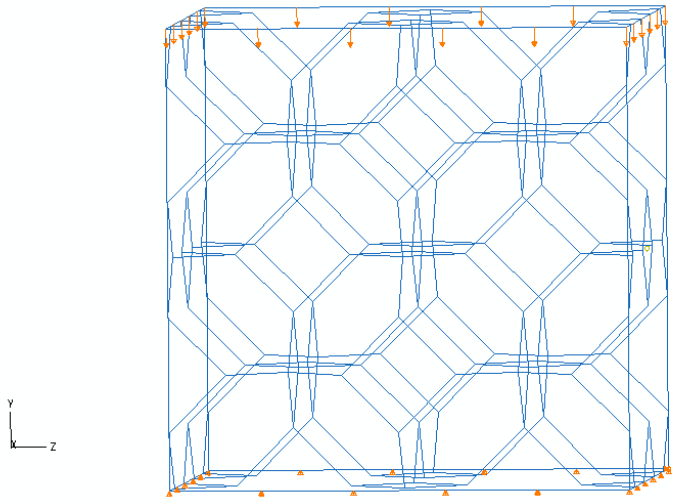

Figure 4.14. Illustration of displacement boundary conditions on the cube FE model.

Similar to the boundary conditions of the RVE described in Section 4.3.3, the nodes –y plane of the cube are constrained in the y-direction, as shown in Figure 4.14. A single point is also constrained in the x- and z- directions on this surface as well for computational stability. A displacement boundary condition is applied to all nodes on the +y surface of the cube; they are displaced an equal magnitude in the negative y-direction. The magnitude applied is 0.045248 mm, equivalent to 1% strain in the y-direction of the cube.

4.4.3 Deformation and Stress Distribution in Ligaments

Displacements of the beam elements in the HA/P/C model are shown in Figures 4.15 and 4.16. In these plots, the solid elements are removed in post-processing for visual purposes. The displacement contours are again plotted on deformed shape with a 20x to show deformation trends. As can be seen in Figure 4.15, the total y-displacements on the +y surface again reflects the applied displacements of 0.045248 mm. The z- and x-translations are given in Figure 4.16, here it is seen that the total expansion in both directions is 0.011 mm. This value is nearly half that of the 0.02 mm expansion in the x- and z-directions found in the carbon foam analysis with the same 1% global strain applied, as shown in Section 4.3.5. This smaller expansion value is attributed to constraints on the foam by the HA/PDLGA phase.

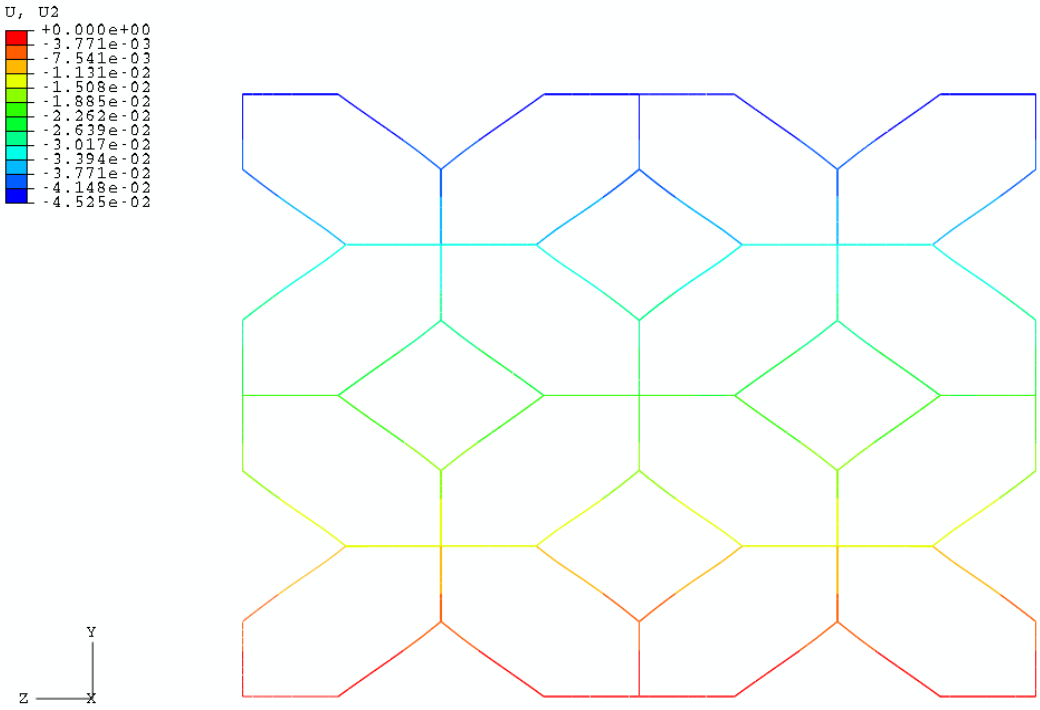

Figure 4.15. Contour plot of the y-displacements in the ligaments in the HA/P/C model.

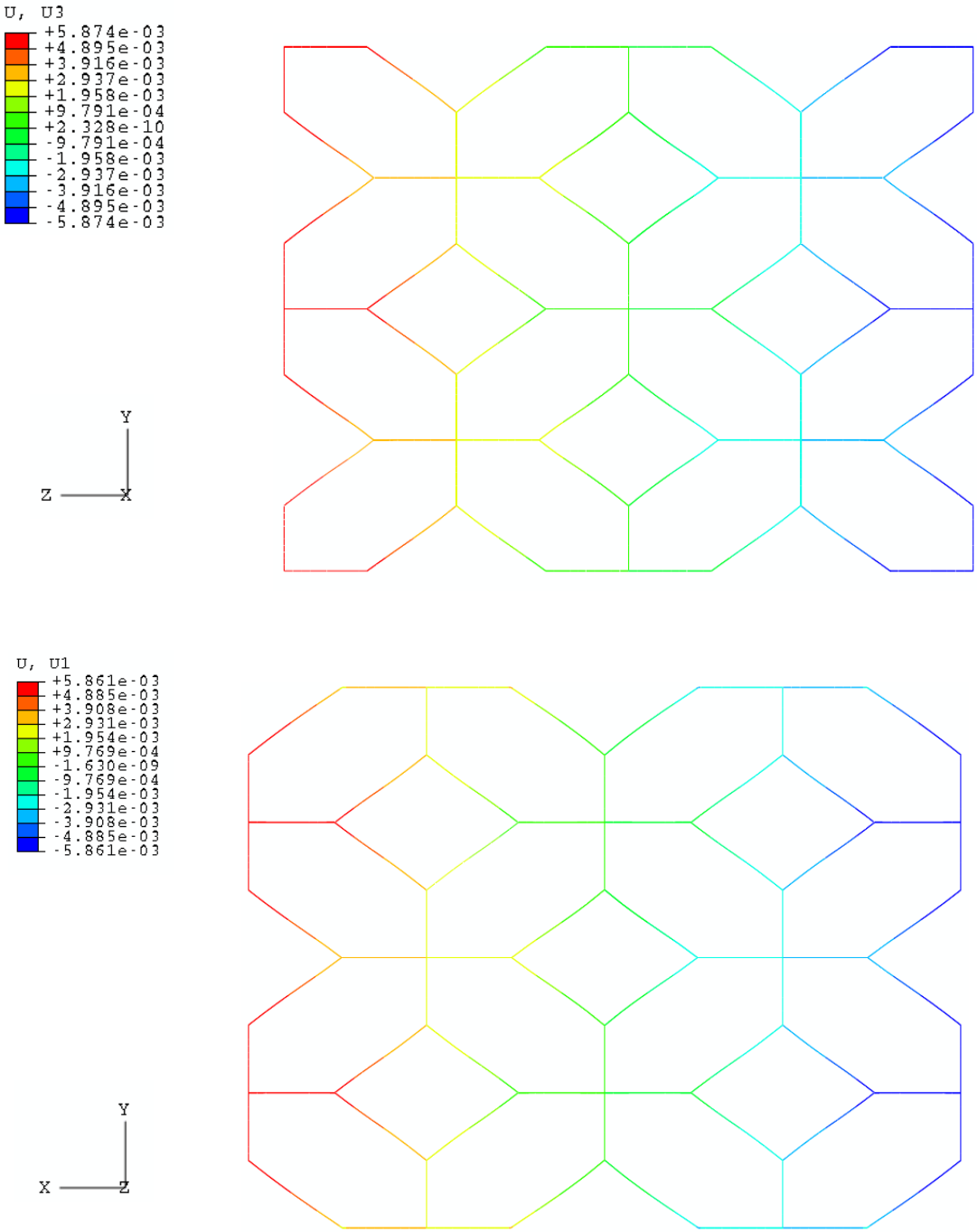

Figure 4.16. Contour plot of the x- and z-displacements in the ligaments in the HA/P/C model.

Figure 4.17 shows the stress contours in the ligaments that occur at the upper-most point in the cross-section as highlighted in the inset. The maximum stresses in the ligaments occur at this location in the cross-section, where a maximum tensile stress of 178 MPa and a maximum compressive stress of 252 MPa is seen.

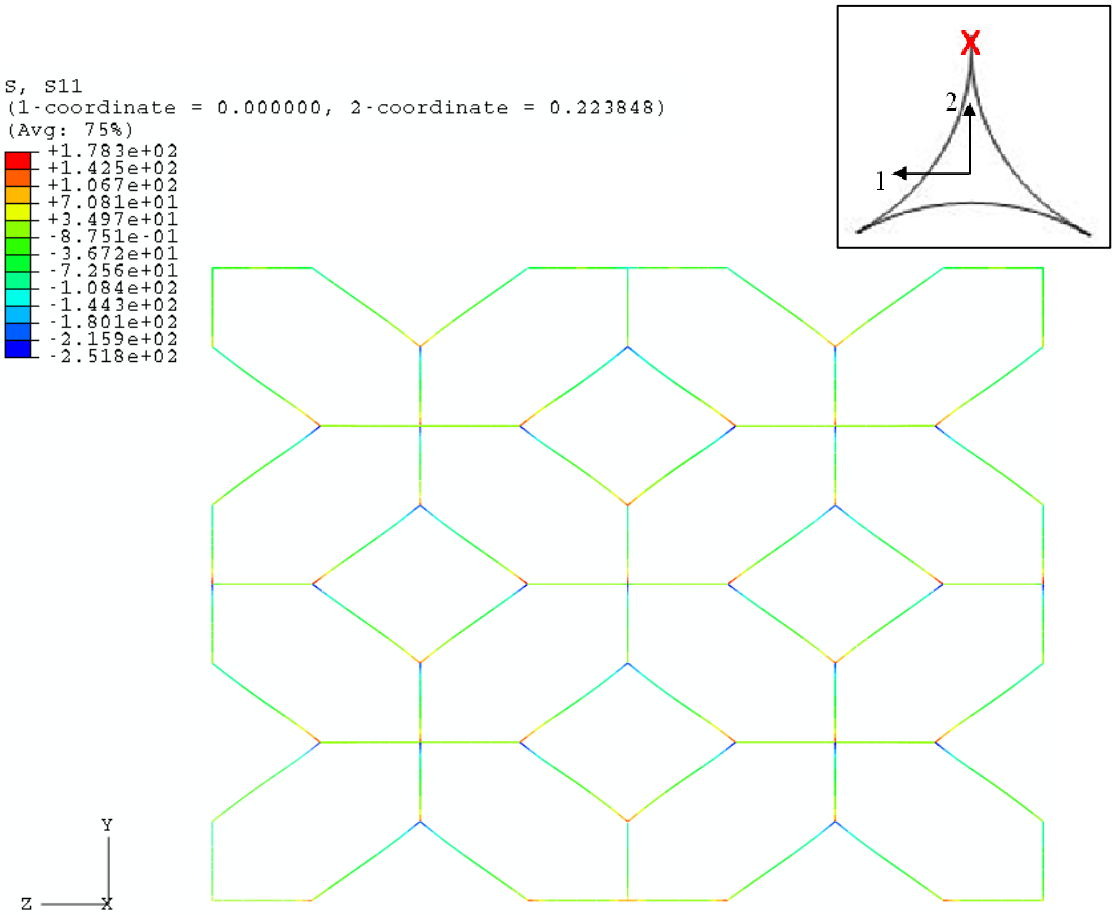

Figure 4.17. Contour plot of the axial stress (MPa) in the ligaments in the HA/P/C model. The location is at the point in the cross-section highlighted by the red x in the inset. The maximum tensile stress is *178 MPa* whereas the maximum compressive stress is *251 MPa*, occurring in the ligaments highlighted by the arrows. (Contours are plotted on deformed shape with 20x scale).

4.4.4 Deformation and Stress Distribution in HA/PDLGA Phase

Contour plots of the displacements of the HA/PDLGA solid elements in the x- and z-directions as a result of loading in the y-direction are shown in Figure 4.18. The total expansion value in the x-direction is 0.011 mm, as well as 0.011 mm in the z-direction; as expected, these are the same total expansion values seen in the ligaments. It is seen, however, that the displacements are non-uniform through the y-direction, a result of the addition of the carbon foam.

The stress contours in the HA/PDLGA are shown in Figure 4.19 where the contours are plotted on half-sections of the cube to illustrate the internal state of stress. When looking at the normal stresses in the y-direction, it is first noted that the majority of the HA/PDLGA experiences a σ_{22} of about -15 MPa. This value is expected based on the modulus of the HA/PDLGA (1580 MPa) and applied strain of 1%. Furthermore, the addition of carbon foam results in areas of stress concentrations of up to -18 MPa. These same concentrations can be seen in the contour plots of the σ_{33} and von Mises stress components as well.

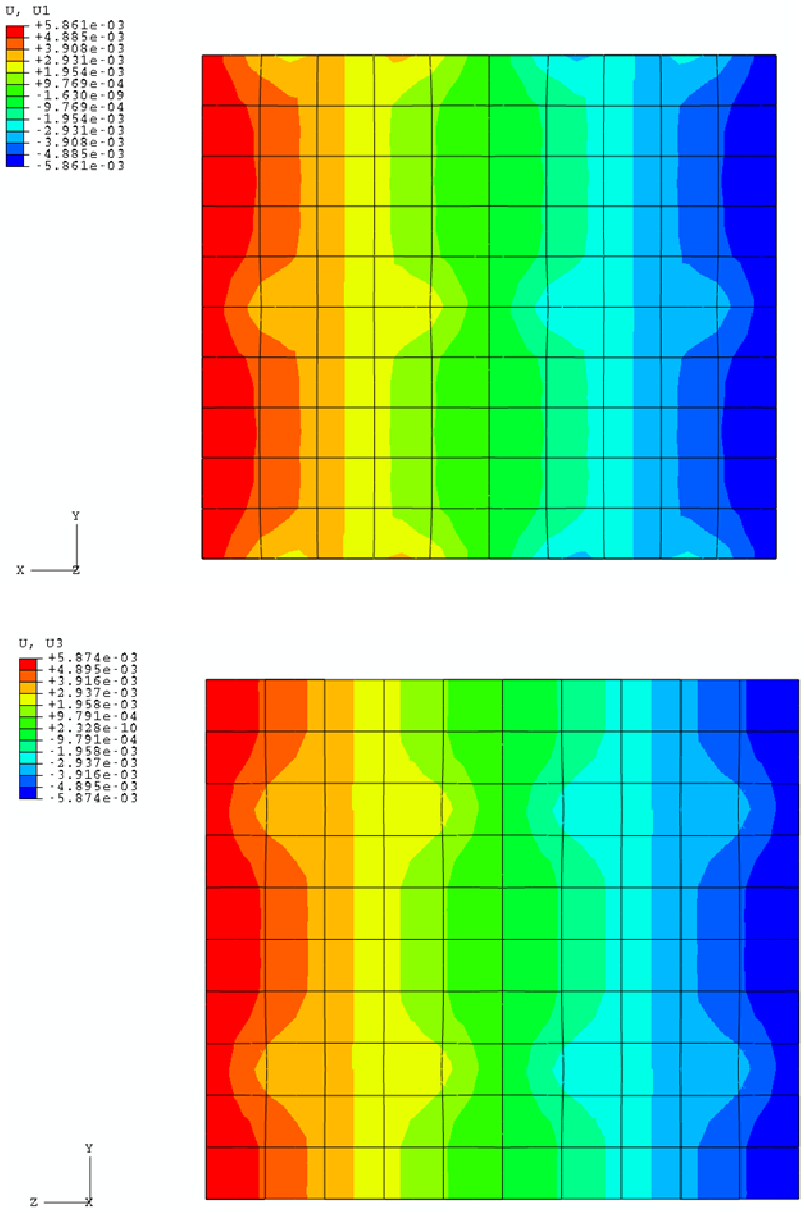

Figure 4.18. Contour plots of x- and z- translation on the solid elements representing the HA/PDLGA phase of the HA/P/C material system.

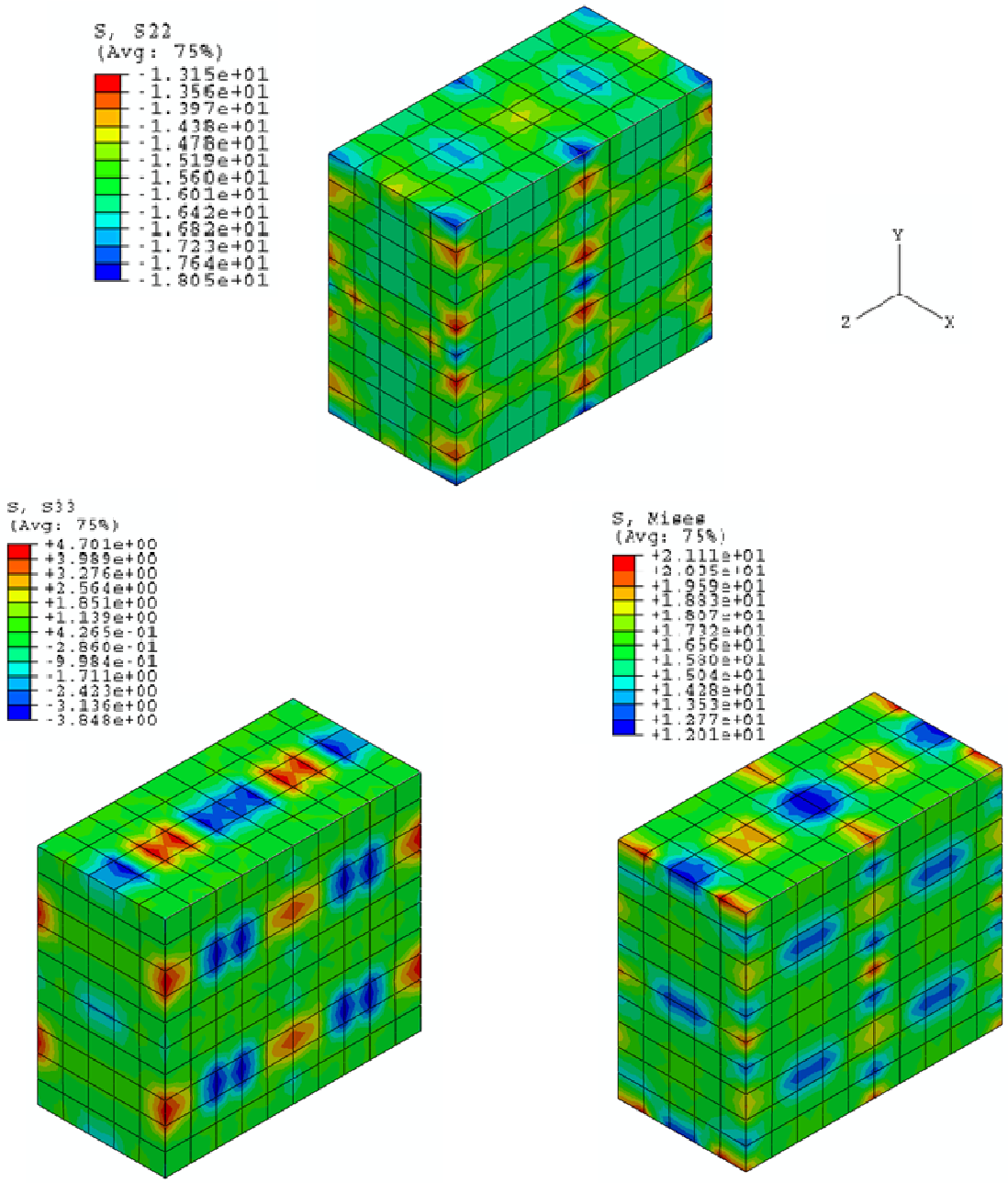

Figure 4.19. Contour plots of normal stresses in the y- and z-directions as well as the Von Mises stress. The stresses are plotted on half-sections of the cube to show the internal state of stress.

4.4.5 Effective Modulus and Strength Results

When applying a 1% strain to the HA/P/C RVE in the – y-direction, the summation of the resultant nodal reaction forces on the + y-surface leads to -341.1 N. Using Equation 4.9 again to calculate the effective stiffness E_y^* results in a value of 1665 MPa, representing an increase of 85 MPa from the modulus of HA/PDLGA of 1580 MPa used in this model.

The maximum stress seen in the foam ligaments is a tensile stress of 178 MPa and a compressive stress of 254 MPa. Again, the stress allowable of the ligaments is assumed to be 210 MPa in tensile mode, and 690 MPa in compressive mode.

The manufacturer reports the yield strength of the PDLGA to be 58 MPa, so the maximum von Mises stress of 21 MPa for the HA/PDLGA phase is within the yield stress for the polymer.

In this case, a 1% global strain results in a state of stress where the ligaments are likely to see failure before the HA/PDLGA yields. Again, because of the isotropic properties and the symmetry involved in the RVE structure, the allowable is assumed to be approximately the same in any direction of loading, as well as the value for both tensile and compressive loads.

4.5 Remarks

First, the computational models in this section demonstrate the addition of HA to PDLGA at a 15% volume fraction results in an effective modulus that is approximately 33% greater than that of PDLGA. For example, if the modulus of PDLGA is that as reported, 1300 MPa, the effective modulus of HA/PDLGA is 1740 MPa. However, if voids content in the HA/PDLGA material is 5% (as was measured in Section 2), the effective modulus is only 1580 MPa.

In addition, the FE analysis reveals that the addition of carbon foam with 95% porosity to the HA/PDLGA system results in a 5% increase in effective stiffness relative to the HA/PDLGA system. The carbon foam, however, results in a lower effective strength of the system, where the maximum global strain before damage is about 1%. In this scenario, the carbon ligaments experience a state of stress where exceeding the carbon allowable, whereas the stress state in the HA/PDLGA is below the yield strength.

5. FE SIMULATION OF INTERNAL FIXATION PLATE ATTACHED TO TRANSVERSELY FRACTURED FEMUR

5.1 Overview

To assess feasibility of the HA/PDLGA/Carbon Foam material system for use as an orthopedic fixation device, a FE model is created in which an internal fixation plate bridges a transverse diaphyseal fracture in a human femur. Here, the time-dependent constitutive response of the HA/PDLGA/Carbon Foam fixation plate is simulated by applying the empirical dissolution rate of HA/P/C to the fixation plate. Simultaneously, the fracture healing process is simulated by incorporating the mechanical properties of the progression of tissues in the fracture gap. Physiological loading conditions are applied to the femur and the resulting stress/strain distribution in the bone plate is studied to determine the capability of the HA/P/C plate to withstand the applied loads. Additionally, the stress/strain distribution in the bone fracture gap and surrounding area is investigated to determine if the HA/P/C bone plate is capable of maintaining fracture stability while loads are applied.

The geometry of the human femur and the subsequent idealized femur geometry used in the models are described in Section 5.2. The simulated geometry of a transverse diaphyseal fracture is also addressed in this section. Described in Section 5.3 is the approach used to computationally model the fracture, where the fractured volume is modeled as a discontinuity in material properties in comparison to the unaffected bone. Here, the healing of the fracture is modeled by defining the modulus of the fracture zone as a function of time using values obtained from literature.

The method of applying the empirical dissolution rate as determined in Section 3.4.6 to the HA/P/C fixation plate is discussed in Section 5.4. Here, dissolution is assumed to occur in two dimensions because of the aspect ratio of the plate (length to depth ratio and length to width ratio). Potential plate geometries are then selected based on comparison of plate dissolution rates with fracture healing rates; in this case, the time-variation of plate axial stiffness and fracture zone axial stiffness is investigated. The variation of the fracture zone axial stiffness is due to the change in tissue modulus over time, whereas the variation of the HA/P/C plate axial stiffness is due to the change in plate cross-section over time from dissolution.

5.2 Human Femur Characteristics

5.2.1 Femur CAD Model

A CAD model of the cortical bone of an adult left femur is downloaded as a SolidWorks Parts file and shown in Figure 5.1. This femur geometry has been created by Marco Vicentonti; it is available on the Internet through the BEL Repository managed by the Istituti Ortopedici Rizzoli, Bologna, Italy. Additionally, the femur geometries and meshes provided by BEL Repository have been used in numerous computational analyses[70-72].

The femur CAD model is ~485 mm in length; cross-sections of the middle 150 mm of the femur are examined and shown in Figure 5.1. The average inner and outer diameters of the cross-sections are 16.1 mm (1.77 Std Dev) and 31.5 mm (1.04 Std Dev), respectively. As can be seen from the cross-sectional images, the most distal cross-section has larger inner and outer diameters (18.7 mm and 32.5 mm) than the others.

5.2.2 Idealized Femur Diaphysis and Transverse Diaphyseal Fracture

Since the regions of interest in this analysis are the interfragmentary gap and the fixation plate, only the femur diaphysis is modeled in this study. Here, the diaphysis is idealized as a cylinder 200 mm in length with a constant cross-section (inner diameter, d_i, of 15 mm and outer diameter, d_o, of 31 mm). The cross-section dimensions are the approximate dimensions of the three most proximal cross-sections shown in Figure 5.1.

The simulated fracture in the current study is a transverse fracture at the midpoint of the idealized diaphysis. The fracture is 2 mm in thickness and retains the same cross-section of the idealized cylinder; no fracture callus is modeled here. The transverse fracture is the green portion of the idealized femur shown in Figure 5.1.

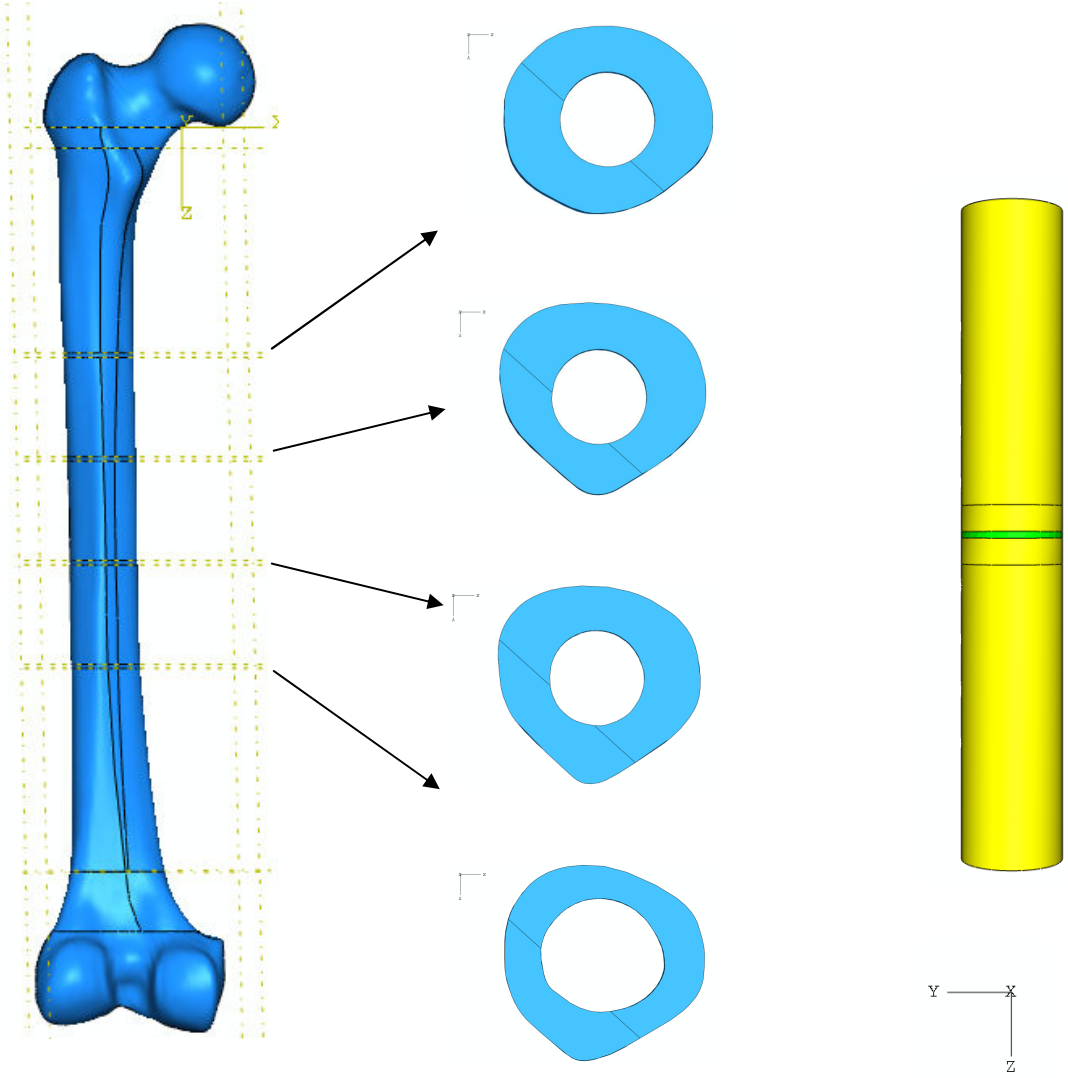

Figure 5.1. a) Images of femur CAD geometry as well as cross-sections located at the indicated planes. b) Image of idealized diaphysis of the femur used in this study, modeled as a cylinder 200 mm in length with constant cross-sectional dimensions of d_i: 15 mm and d_o: 31 mm. (Images are not to scale)

5.2.3 Fracture Healing Rate

To the best of the author's knowledge, there does not exist any data on a universal healing rate of fractures, i.e. a tissue modulus as a function of time. This is not surprising since so many variables are involved in the fracture healing process, including fracture type, size, and location, as well as physiological parameters that can vary from person-to-person such as blood flow, cell density, and nutrition. There has been research, however, where tissue differentiation during fracture healing is modeled based on mechano-regulation theory[73-79]. In this approach, FE models are used to simulate tissue differentiation in a transverse diaphyseal fracture in a long bone, often an ovine tibia. Differentiation is assumed to be regulated by various biophysical stimuli such as load-induced hydrostatic stress in a linear elastic analyses, or principal strains, hydrostatic pore pressure, deviatoric strain, or fluid velocity in poroelastic analyses. In these analyses, differentiation rates, and thus tissue modulus rates, are dependent upon fracture gap size and axial load magnitude.

Isakkson et al.[78] in particular reports interfragmentary stiffness rates as a result of differentiation for several differentiation algorithms. In this work, a fractured ovine tibia as shown in Figure 5.2 is modeled where tissue differentiation is investigated with several algorithms. As fracture healing progresses and the tissue differentiates, the material properties in the fracture are updated with the corresponding tissue properties. In Isakkson's work, the interfragmentary stiffness is reported as a function of time; the stiffness rate of one model from that work is shown in Figure 5.3.

Since the loads are axial in Isakkson's work, it is assumed the interfragmentary stiffness they report is comparable to a spring stiffness k, where the relationship between stiffness and modulus E is $k = (AE)/L$. This relationship is used to calculate the tissue modulus in the fracture gap based on the geometry of the Isakkson's model (A is πr^2 where r is 14 mm; L is 1.5 mm) and the interfragmentary stiffness they report. Because this relationship is used, it should be noted the calculated tissue modulus is an effective property, that is, it is an averaged value for the modulus across the entire fracture. The results for the fracture tissue modulus as function of time are shown in Figure 5.3 on the right y-axis. This modulus as a function of time is then assumed to be the normal healing rate for a transverse diaphyseal fracture. It is this healing rate that is implemented in the FE model developed in this section.

It should be noted that this healing rate results in a modulus of approximately 1600 MPa after 75 days of healing. This value is still one order of magnitude less than the modulus of healthy bone, 12-18 GPa. One possibility for this difference can be attributed to the foundation of the mechano-regulation analysis, where only tissue differentiation is modeled in the secondary healing process. Remodeling of the bone is not captured in this process, thus the healthy bone modulus is not achieved. As such, the fracture healing rate derived here is viewed as a conservative measure for this analysis.

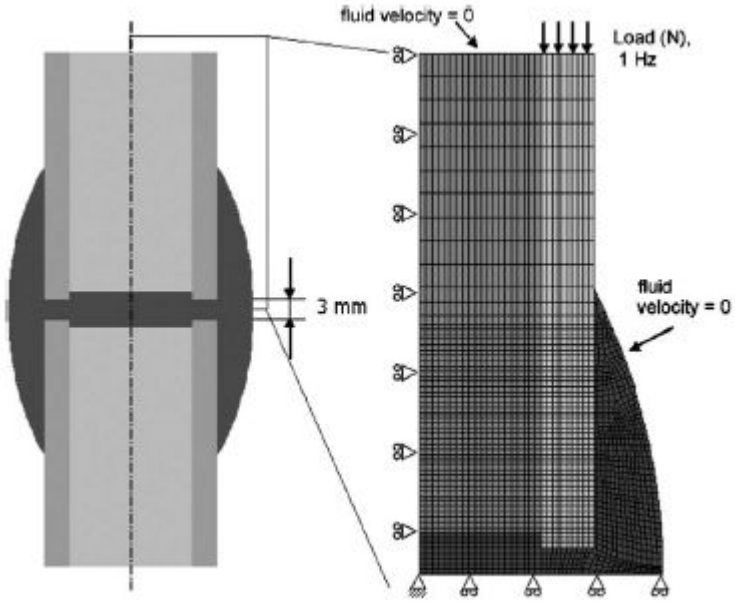

Figure 5.2. Illustration of geometry and FE mesh of ovine tibia with a 3 mm transverse fracture gap used in Isakkson et al.[78] (image copied from paper). The FE model utilizes axisymmetric elements with poroelastic material properties assigned to the fracture tissue. The cortical bone has inner and outer diameters of 14 mm and 20 mm, respectively, while the external callus has a diameter of 28 mm at the fracture gap.

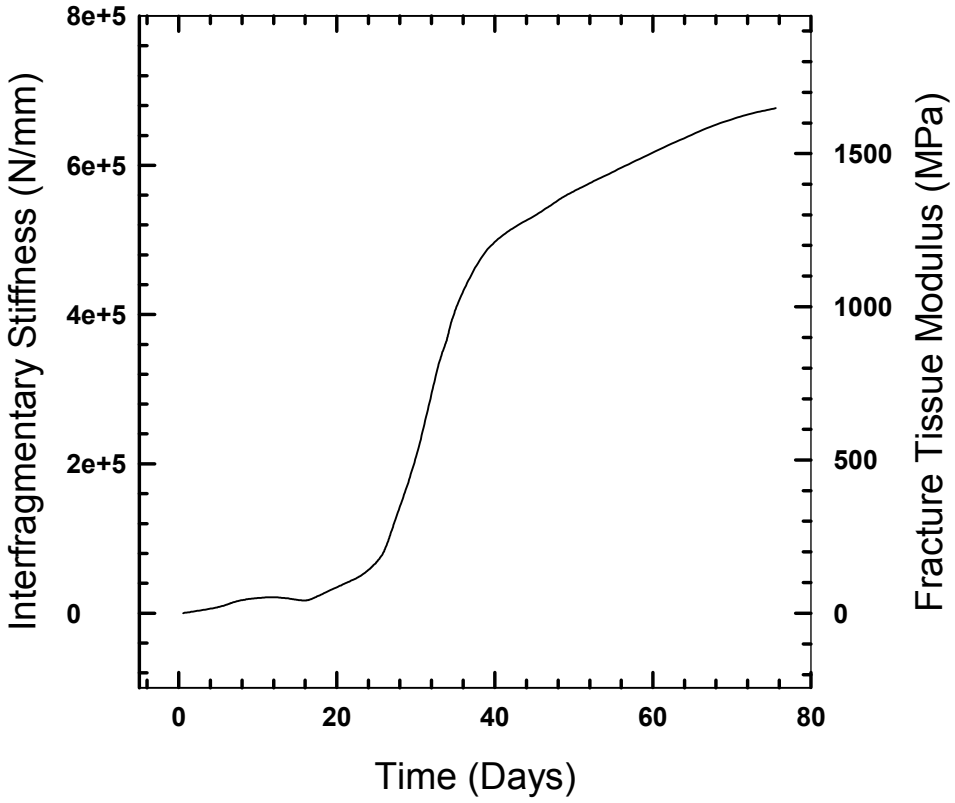

Figure 5.3. Plot showing the Isakkson et al[78]. interfragmentary stiffness data as a function of time; the geometry of the interfragmentary gap of their model is then used to calculate the effective tissue modulus in the interfragmentary gap (right y-axis). This tissue modulus as a function of time is then assumed to be the normal healing rate in these FE models.

5.2.4 Resultant Force and Moment from Standing

The loads applied in this study are the resultant force and moment on the femur diaphysis from a state of standing. Here, an 80 kg mass is assumed to be equally shared by both legs, resulting in approximately 400 N applied at each femoral head, applied in the z-direction in the illustration in Figure 5.4. Because of the offset between the femoral head and diaphysis, there will be a moment about the y-axis in addition to an axial compressive force. If the load is assumed to be applied as a point-load at the top-most point of the femoral head, the distance between the applied load and centroid of the diaphysis cross-section is 40 mm, as shown in Figure 5.4. This results in a moment of 16000 Nmm, which is applied to the idealized diaphysis shown to the right in Figure 5.4. Here it is seen that the fixation plate is attached to the side where tensile stresses arise from the applied moment, as that is where the plate is typically placed[80].

It should be noted that the standing load is assumed to be static and muscle forces are neglected in this analysis. In addition, this same load is applied to models at all times. Although it is unlikely the patient would be experiencing this standing load immediately after surgery, this load at day 0 is viewed as a worst-case scenario.

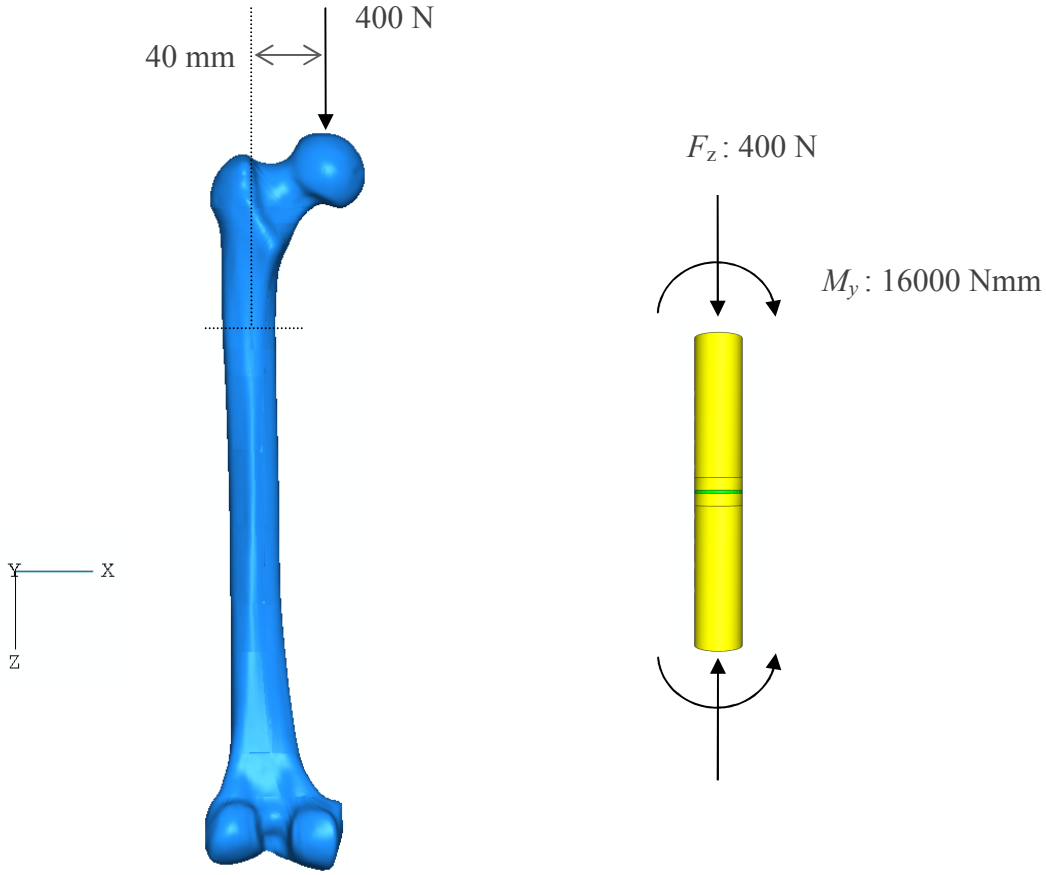

Figure 5.4. Illustration depicting offset of axial load applied at the femoral head, and the application of resultant force and moment to the idealized diaphysis.

5.3 Sizing of HA/P/C Internal Fixation Plate

5.3.1 Geometry

The initial geometry for the HA/P/C fixation plate is 4 mm x 12 mm x 180 mm, comparable to overall dimensions of commercially-available titanium compression plates. In addition, plates of similar dimensions are investigated in the literature for use as femoral fixation plates[37, 81-85]. In the current model, the idealized plate has a radius of curvature of 15.5 mm along the width, to match that of the outer surface of the femur. An image of the plate attached to the idealized femur is shown in Figure 5.5a.

The holes of the idealized plate are 5 mm in diameter, similar to titanium fixation plates, and they are not countersunk as they are in commercial plates. In addition, the four holes on each side of the fracture are spaced 16 mm from each other, as measured from the center of the holes. The two holes nearest the fracture are spaced 32 mm apart.

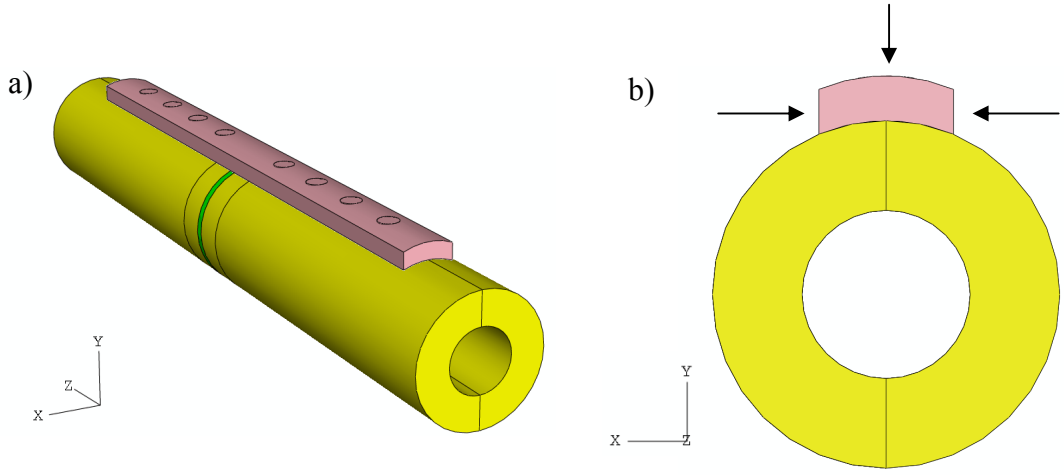

Figure 5.5. a) Image of standard fixation plate in relation to the idealized fractured femur. Dimensions of the plate are 4 mm x 12 mm x 180 mm with a radius of curvature of 15.5 mm on the top and bottom surfaces. b) Illustration of application of dissolution to the width and depth dimensions of the fixation plate.

5.3.2 Dissolution Rate of HA/P/C Plate

The dissolution rate for the HA/P/C material system determined in Section 3.4.6 is used in determining the change in the effective axial stiffness of the fixation plate in these FE models. Here, the one-dimensional dissolution rate is assumed to be valid for time periods beyond those tested (34 days), as such, the dissolution rate is extrapolated and one-dimensional dissolution depths are calculated for a time period up to 50 days. The extrapolated values are shown in Figure 5.6, where they are plotted on a linear scale as well as a logarithmic scale.

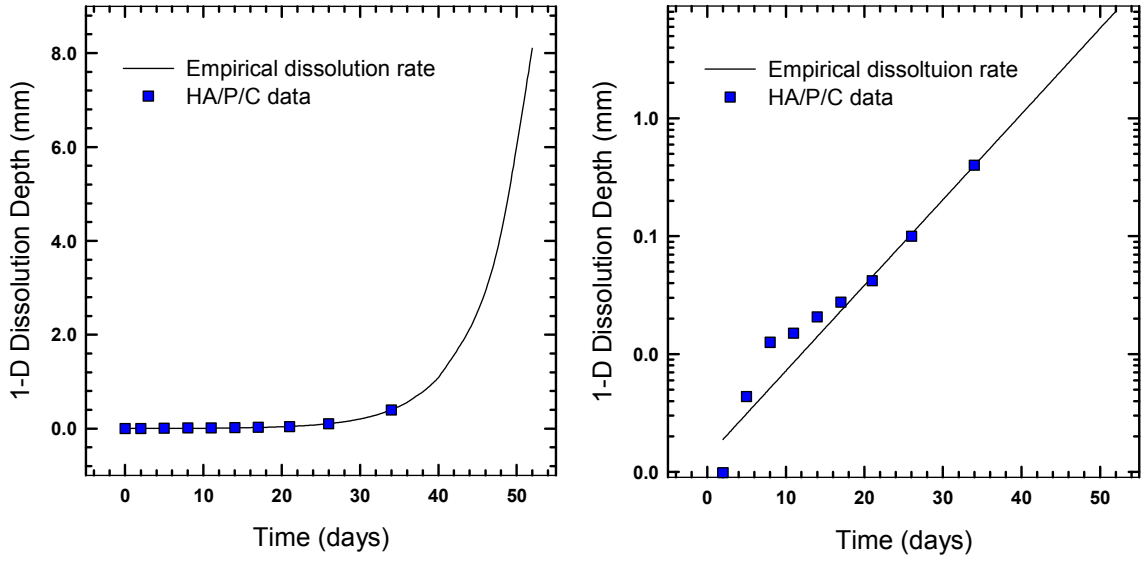

Figure 5.6. Plots of extrapolated dissolution depths based on the empirical dissolution rate determined experimentally in Section 3. The plot on the left is a linear scale whereas the plot on the right is a logarithmic scale to illustrate the exponential nature of the data. The empirical rate equation is $y = ae^{bt}$, where a is 0.00135 mm and b is 0.1673 day^{-1}.

Although the dissolution rate is determined based on one-dimensional data, the fixation plate is assumed to dissolve in two dimensions (the dissolution in the third dimension is assumed to be negligible because of the aspect ratio of the plate). The plate is assumed to dissolve in the cross-section, where the width and depth dimensions are each reduced by the one-dimensional dissolution depth corresponding to the appropriate day. In these models, the plate is flush with the femur, thus dissolution is assumed to only occur through the top surface in the depth direction, as shown in Figure 5.5b. In taking this approach, two-dimensional effects are neglected.

5.3.3 Healing Rate versus Dissolution Rate Considerations

To determine the cross-sectional dimensions of the HA/P/C fixation plate, the time-variation axial stiffness of potential plate geometries is compared to the time-variation of the interfragmentary axial stiffness. In this scenario, the variation of the interfragmentary stiffness is due to fracture healing (change in tissue modulus over time), whereas the variation of the HA/P/C plate axial stiffness is due to the change in effective plate modulus over time from dissolution of the HA/P phase.

In this analysis, the axial stiffness k is calculated as $k = (AE)/L$, where A is the appropriate cross-sectional area, E is modulus, and L is length. Since the fixation plate bridges the fracture gap, the length of interest for comparison is that of the fracture gap. As such, for both the plate and the fracture stiffness calculations, L is 1 mm (the interfragmentary gap), as shown in Figure 5.7. The cross-section of the fracture area is $\pi(r_o^2 - r_i^2)$, or 580 mm^2, and $E_{fracture}(t)$ is taken as the curve presented in Figure 5.3. The axial stiffness of the fracture area is calculated and presented in Figure 5.8.

The variation in the axial stiffness of the plate comes from dissolution of the HA/P phase, and thus a variation on the effective modulus of the plate over time. As the HA/PDLGA phase dissolves from the plate surface, the carbon foam remains. As such, that area where only carbon foam remains has a modulus of 40 MPa (as determined in the RVE model in Section 4) and the remaining unaffected area of the plate has a modulus of 2000 MPa.

The effective axial modulus of the plate, E^*_{plate}, is determined using composite theory, where the rule-of-mixtures is utilized and is as follows:

$$E^*_{plate} = E_{HA/P/C}\frac{A_{HA/P/C}}{A_{plate}} + E_C\frac{A_C}{A_{plate}} \quad \textbf{(5.1)}$$

where the subscripts *HA*/*P*/*C* and *C* indicate the respective values for the HA/P/C phase and the carbon foam phase. If it is the curvature of the plate is neglected, the above can be rewritten in terms of the plate width and thickness, *b* and *h*, as:

$$E^*_{plate} = E_{HA/P/C}\frac{(b-2d)(h-d)}{bh} + E_C\frac{(bd)+2d(h-d)}{bh} \quad \textbf{(5.2)}$$

where *d* is the dissolution depth as a function of time.

The E^*_{plate} values are used to determine the variation of the plate axial stiffness using $k_{\text{plate}} = \left(E^*_{plate}bh\right)/L$ for plates of three different dimensions: i) 4 mm x 12 mm, ii) 4 mm x 6 mm, and iii) 6 mm x 20 mm. The axial stiffness for each plate is given in Figure 5.8.

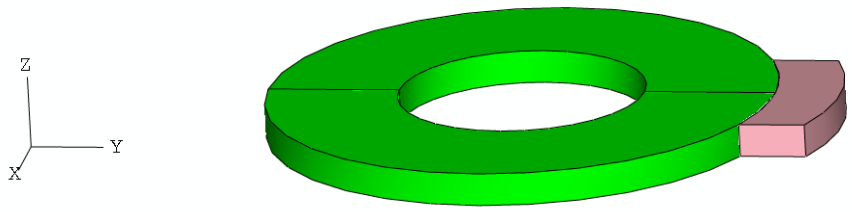

Figure 5.7. Interfragmentary sections used in the axial stiffness computations.

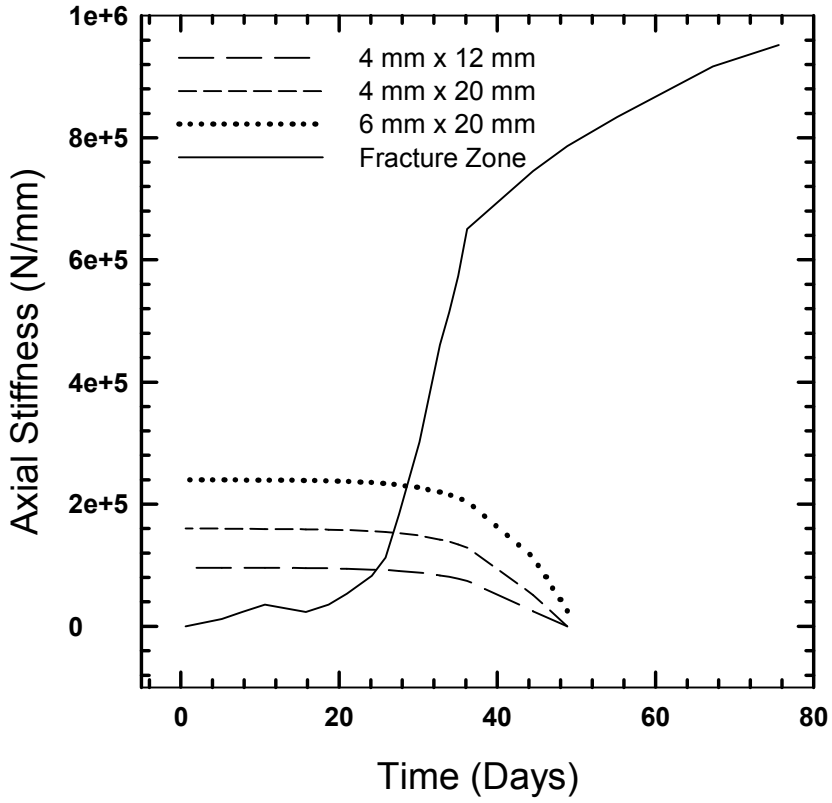

Figure 5.8. Plot comparing the axial stiffness of the fracture zone and the axial stiffness of various HA/P/C plates as a function of time. The variation of the fracture zone axial stiffness is due to the change in tissue modulus over time, whereas the variation of the HA/P/C plate axial stiffness is due to a change in plate effective modulus from dissolution.

As can be seen from the comparison of the axial stiffness of the fracture and HA/P/C plates, the stiffness of the plates remain near their original value until about day 30. At this time, the stiffness begins to decrease slowly until day 36 where the values begin to decrease more rapidly. The rate at which the stiffness decreases reflects the relationship's dependence on the dissolution depth that exponentially increases with time. The fracture stiffness is initially zero, reflecting the low tissue modulus in the early stages of healing, and then begins a rapid increase between days 28 and 36. This period of rapid increase in fracture stiffness occurs immediately prior to the decrease in period of rapid decrease in plate stiffness.

Because of the exponential relationship of the dissolution depth as a function of time, all the axial stiffness of all plates reach near-zero at approximately the same time – day 47 for the two smaller plates and day 48 for the larger plate. At this time, the fracture modulus from the healing rate derived in Section 5.2.3 is approximately 1350 MPa. As stated in that section, this healing rate is viewed as a conservative measure, so the modulus could potentially be higher at this time.

The plates with 4 mm x 12 mm and 6 mm x 20 mm cross-sections and properties of HA/P/C are to be considered in this analysis. Additionally, a titanium plate with a cross-section of 4 mm x 12 mm is considered for comparison. The analysis will be performed at time of 0 days, reflecting immediately after fixation, and at a time of 35 days where the plates begin to rapidly lose axial stiffness.

5.4 Mesh Creation and Element Properties

Because of the symmetry involved in the problem, the idealized femur/fixation plate is modeled as using a half-model with a plane of z-symmetry about the mid-plane of the bone (mid-fracture). In this half-model, then, the idealized bone is 100 mm in length, the interfragmentary gap is 1 mm, and the fixation plate is 80 mm in length.

After the geometries are created, the idealized plate and screws are meshed with 8-noded linear solid elements (C3D8R) and the idealized femur diaphysis is meshed with 20-noded quadratic solid elements (C3D20R); each node has u_x, u_y, and u_z degrees-of-freedom. The plate consists of 12012 elements and each screw consists of 924 elements; the bone consists of 21006 elements where the mesh is refined toward the fracture. Images of each mesh are presented in Figure 5.9.

Linear elastic properties are assigned to all elements in this model. Since titanium alloys are preferred in bone screws[86, 87], the properties of Ti-6Al-4V (TAV) are assigned to the idealized screws in all models, with an E of 110 GPa and 0.33 v. In addition, pure titanium properties (E of 110 GPa and 0.33 v) are assigned to the titanium

fixation plate. The healthy bone is assigned an isotropic modulus of 18 GPa and v of 0.28, and the interfragmentary modulus is assigned using the time-dependent modulus values shown in Figure 5.3. Some values of this modulus at various days are given in Table 5.1.

At initial fixation of the HA/P/C plate, day 0, there is no dissolution and thus the elastic modulus of the HA/P/C system determined in Section 4.4 is assigned to the entire plate (2000 MPa). At specified times, the plate is partitioned based on the dissolution depths in the plate width and thickness dimensions. Those elements where the HA/PDLGA dissolved are assigned the properties of bulk carbon foam as determined in Section 4.3, a modulus of 40 MPa and v of 0.44. For example, the inset in Figure 5.9 illustrates the cross-sectional mesh of a 4 mm x 12 mm plate at day 35, where the dissolution depth is 0.47. The blue elements in the inset are assigned carbon foam properties to reflect the dissolution of the HA/P phase. Some values of dissolution depths at various days are given in Table 5.1.

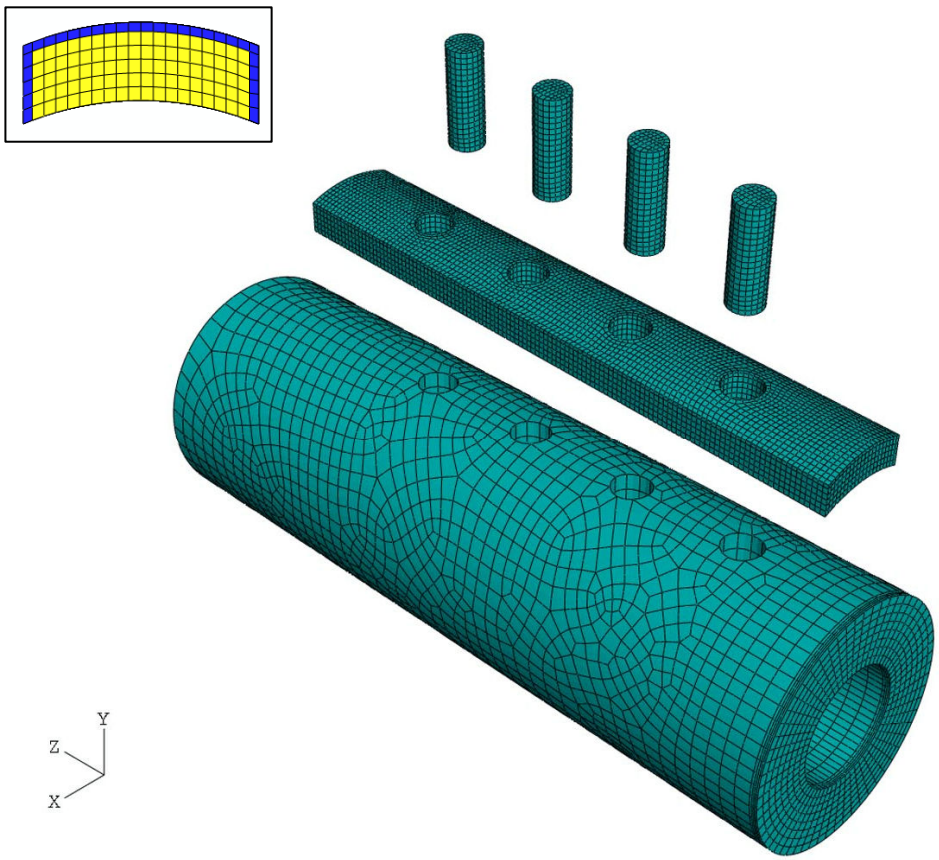

Figure 5.9. Image of mesh of idealized bone, fixation plate, and screws. The inset is the cross-sectional mesh of a 4 mm x 12 mm plate at day 35, where the blue elements as assigned carbon foam properties and the yellow elements are assigned HA/P/C properties.

Table 5.1. List of HA/P/C dissolution depth and tissue modulus as a function of time.

Time (Days)	HA/P/C 1-D Dissolution Depth (mm)	Interfragmentary Modulus (MPa)
0	0.0	10
21	0.045	90
28	0.146	320
35	0.47	990
42	1.52	1260
49	4.90	1370

5.5 Boundary and Loading Conditions

5.5.1 Simulating Plate Attachment

The fixation plate is attached to the bone with the idealized screws via the use of the *TIE constraint option in ABAQUS. Here, the screw/bone interface of each screw is tied such that the nodes on each surface have the same displacements; the screw/plate interface is tied similarly. To do this, the surface of the screw which interacts with the bone is defined as a master surface. (The surfaces on each pin are shown in Figure 5.10). The corresponding surface of the hole of the bone is then defined as a slave surface, where the element nodes on this surface are constrained to the same displacement value of the closest node on the master surface (screw). This process is repeated for the screw/plate interface, where the screw surface is defined as the master surface and the plate-hole surface is defined as the slave surface.

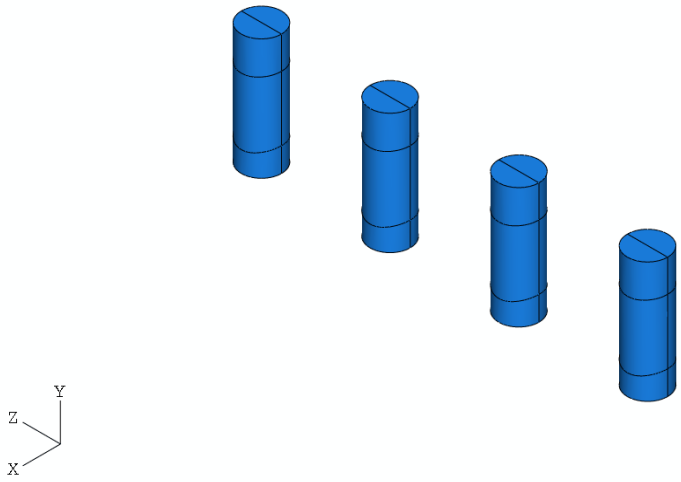

Figure 5.10. Image showing the surfaces of the screws that interact with the plate and the surfaces that interact with the bone.

5.5.2 Symmetry Conditions

Z-symmetry boundary conditions are placed on the - z-plane of the half model (the mid-plane of the full model) by constraining all of the nodes on that surface to zero translation in the z-direction ($u_z = 0$). Z-symmetry conditions also constrain the rotations about the x- and y-axes at each node, but these constraints are not necessary when using solid elements since each node has only translation degrees-of-freedom. In addition to the symmetry conditions, a single point on the symmetry plane is constrained in the x-, y-, and z-translations, as shown in Figure 5.11.

5.5.3 Loading Conditions

Both the axial and moment component of the standing load are applied in a single, static step. Because large displacements are likely to occur in the interfragmentary gap in the early stages of healing, the analysis is performed accounting for non-linear geometry effects. In this approach, the higher-order terms are used in the strain-displacement formulations, where large displacements will impact the results.

A distributed load of -0.7 MPa is applied normal to the + z-surface of the idealized bone as depicted in Figure 5.11. This load is comparable to the axial component of the standing load described in Section 5.4 (400 N / 578 mm^2).

To apply the resultant moment of 16000 Nmm, a reference point is created at the center of the cross-section at the end of the idealized femur, as marked with a yellow X in Figure 5.11. A rigid body is then created where the nodes on the surface of this cross-section are tied to the motion of the reference point defined at the cross-sectional centroid, where the resultant moment is applied. Here, all the relative positions of the

rigid body stay the same but the rigid body can undergo large rigid body motions. Although applying the moment in this manner can create stress and strain concentrations in the rigid body elements from a constraint of Poisson's effects, these concentrations occur in an area that will not affect areas of interest. Also, in these models, the moment is applied about the x-axis since there is a change of coordinate system from the previous coordinate system shown in Figure 5.4.

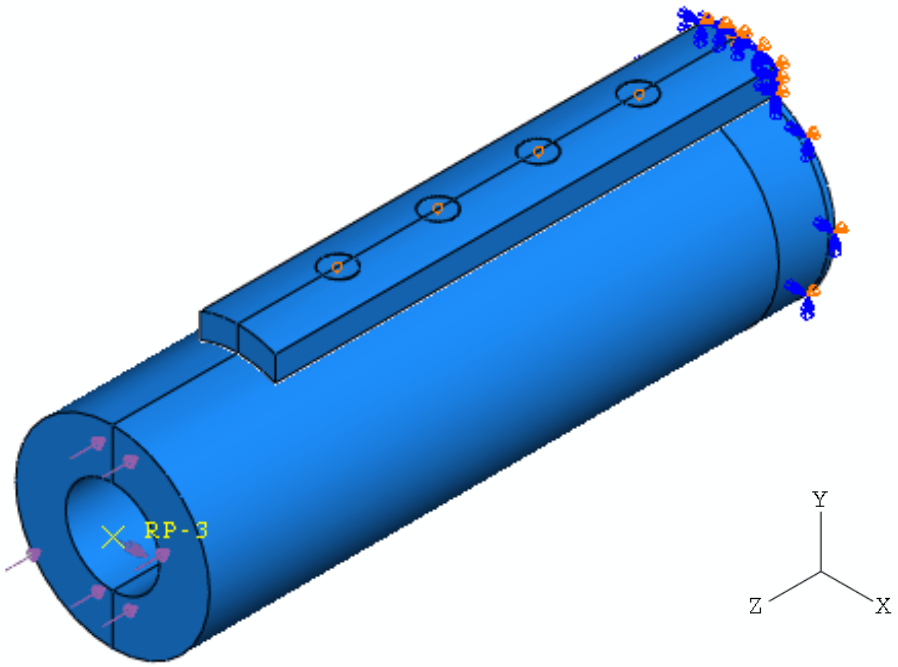

Figure 5.11. Image illustrating the location of applied distributed load of -0.7 MPa to the + z-surface of the bone and the z-symmetry boundary conditions applied to the - z-surface of the bone/plate. The arrow indicates the single point that is constrained in all three translations.

5.6 Results and Discussion

The results for the models given in Table 5.2 are presented in this section. Here, the three plates investigated at day 0 are done so on a model with an interfragmentary modulus of 10 MPa. The 4 mm x 12 mm HA/P/C plate is analyzed at day 35, where the dissolution depth is 0.47 mm and the fracture modulus is 990 MPa. Additionally, the larger HA/P/C plate is analyzed at day 42, where the healing is assumed to be delayed by two weeks. In this case, the fracture modulus is 320 MPa and the dissolution depth incorporated into the plate is 1.57 mm. This case is studied to determine the impact of variability in the healing rate.

Table 5.2. FE models of internal fixation plate attached to transversely fractured femur subjected to axial loading conditions. (+ represents models with normal healing rate, o represents healing rate delayed by 2 weeks).

Internal Fixation Plate		Models		
Material	Cross-Section	Day 0	Day 35	Day 42
Titanium	4 mm x 12 mm	+		
HA/P/C	4 mm x 12 mm	+	+	
	6 mm x 20 mm	+		o

5.6.1 Titanium Plate Model

In investigating the response of the titanium fixation plate model at day 0 (immediately after placement), it is necessary to investigate the displacement, strain, and stress fields in each component to get a complete picture of what is happening. Most of the contour plots presented here are plotted on the half-sections of the bone, screws, and plate for visualization purposes. These plots allow for views of the internal states of deformation, strain, and stress.

First looking at the displacement fields shown in Figure 5.12, it is seen that the translations in the z-direction, u_3, are not uniform throughout the x-z planes (Figure 5.12a). Here, the compressive displacements are much smaller (by an order of magnitude) near the fixation plate as compared to the displacements in the x-z plane opposite of the plate. This is expected, since the fixation plate is acting as an axial stiffener in the z-direction, thus the z-displacements would be smaller in magnitude. Additionally, the u_3 at near the top of the plate are positive whereas those near throughout the bone are negative in value, reflecting the bending displacements expected from the applied moment.

Figure 5.12c shows a magnified image of u_3 in the interfragmentary gap, at the bottom-most x-z planes (opposite of the plate). Here it is seen that u_3 is 0 on the right-most x-y plane, reflecting the boundary condition on that plane. Additionally, the z-displacements on the left-most x-y plane (fracture/healthy bone interface) are similar to the z-displacements in Figure 5.12a, both in magnitude and gradient. This indicates the majority of the z-displacements occurring throughout the entire bone are a result of the displacements in the fracture zone.

Figure 5.12b shows how the displacements in the y-direction, u_2, vary in the bone/plate system. Here, the elements in the left-most x-y planes have significant displacements in the –y direction (~0.2 mm). The u_2 values decrease in the elements that are nearer to the plane of z-symmetry (the values decrease almost linearly with distance). These u_2 affects can be contributed to displacements from bending as well as global-rotations of the bone about the x-axis as a result of the uneven u_3 compression in the fracture zone.

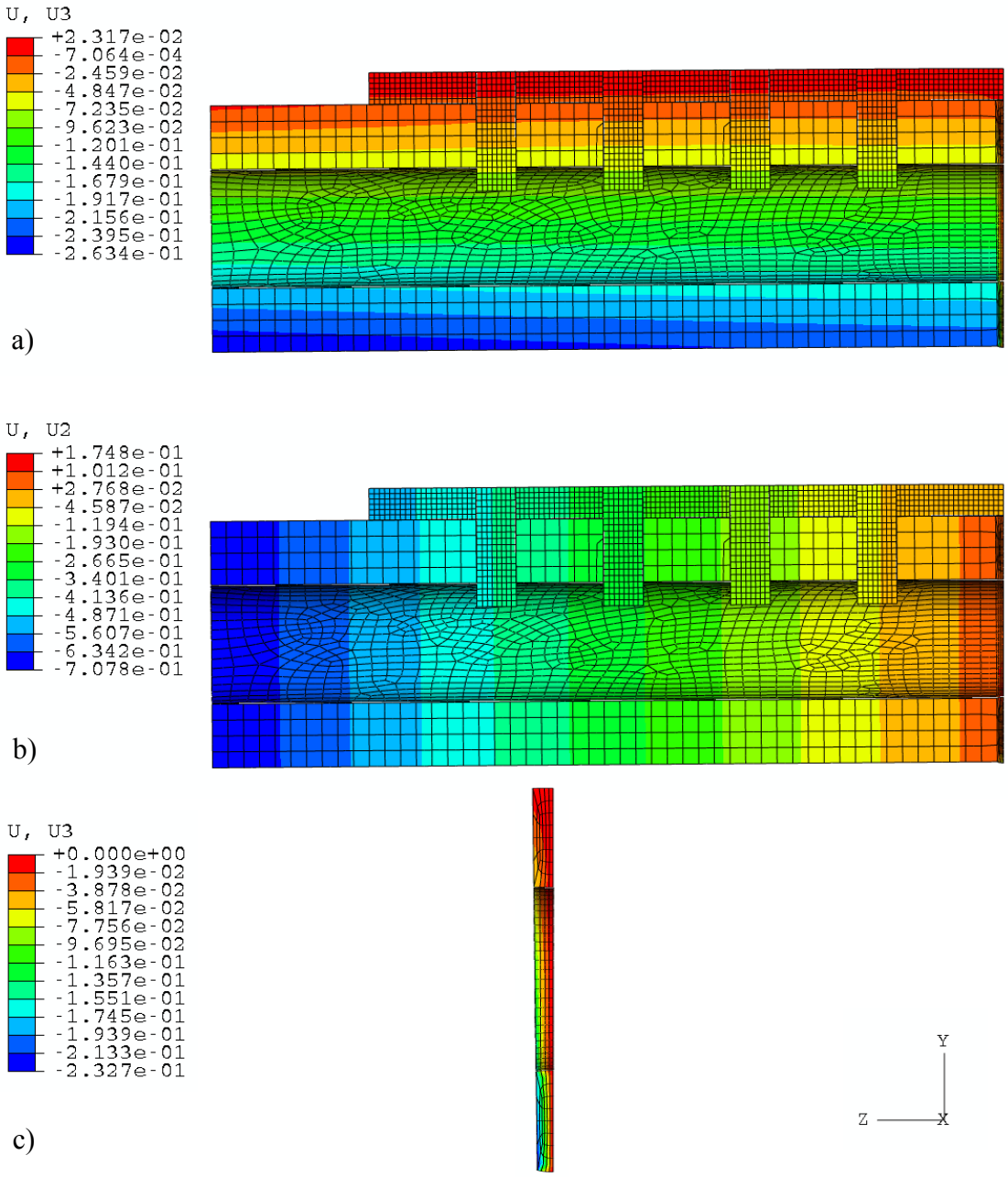

Figure 5.12. Contour plots of z- and y-translations on the deformed shape of the titanium plate model at week 0 (shape is 1x actual deformations).

When looking at the reaction forces on the plane of z-symmetry, as shown in Figure 5.13, it is seen that: a) the plate reaction forces $R_{f,3}$ are both positive and negative and are consistent with bending occurring in the plate, and b) the fracture reaction forces are a mix of positive and negative values throughout the cross-section, with the greatest values being positive. Since the applied axial load is in the -z direction, positive $R_{f,3}$ indicates compressive forces whereas negative $R_{f,3}$ indicates tensile forces. In this model, the $R_{f,3}$ indicate the titanium plate is in a state of bending about the x-axis, where the upper-most x-z planes in the plate are in tension and the lower-most x-z planes are in compression. In addition, a transition through zero forces occurs near the middle x-z planes in the plate, as marked by the dotted line in Figure 5.13.

Although there are negative values of $R_{f,3}$ occurring on the fracture surface, these values are smaller in value compared to the positive reaction forces. Additionally, the negative reaction forces only occur at the corner nodes of all elements, whereas the negative reaction forces occur at the mid-side nodes, indicating that the negative values are a result of the quadratic element shape function.

To understand the reaction force results, and ultimately the state of stress and strain in the plate and fracture, it is of interest to calculate the location of the neutral axis $\bar{x}$ of the bone/plate, as shown in the inset of Figure 5.13. In this effort, the section is treated as a composite beam and the following relationship is used[80]:

$$\bar{x} = \frac{x' E_P A_P}{E_B A_B + E_P A_P} \tag{5.3}$$

where x' is the location of the plate neutral axis, E is modulus, A is area, and subscripts B and P indicate bone and plate, respectively. In this idealized section, x' is 17.5 mm,

and using the moduli of the fracture (here, 10 MPa) and titanium (100 GPa) and the corresponding areas, the composite neutral axis $\bar{x}$ is calculated to be 17.48 mm. So, the composite neutral axis is approximately the same as the titanium plate neutral axis in this model (due to the high mismatch of titanium and fracture zone moduli).

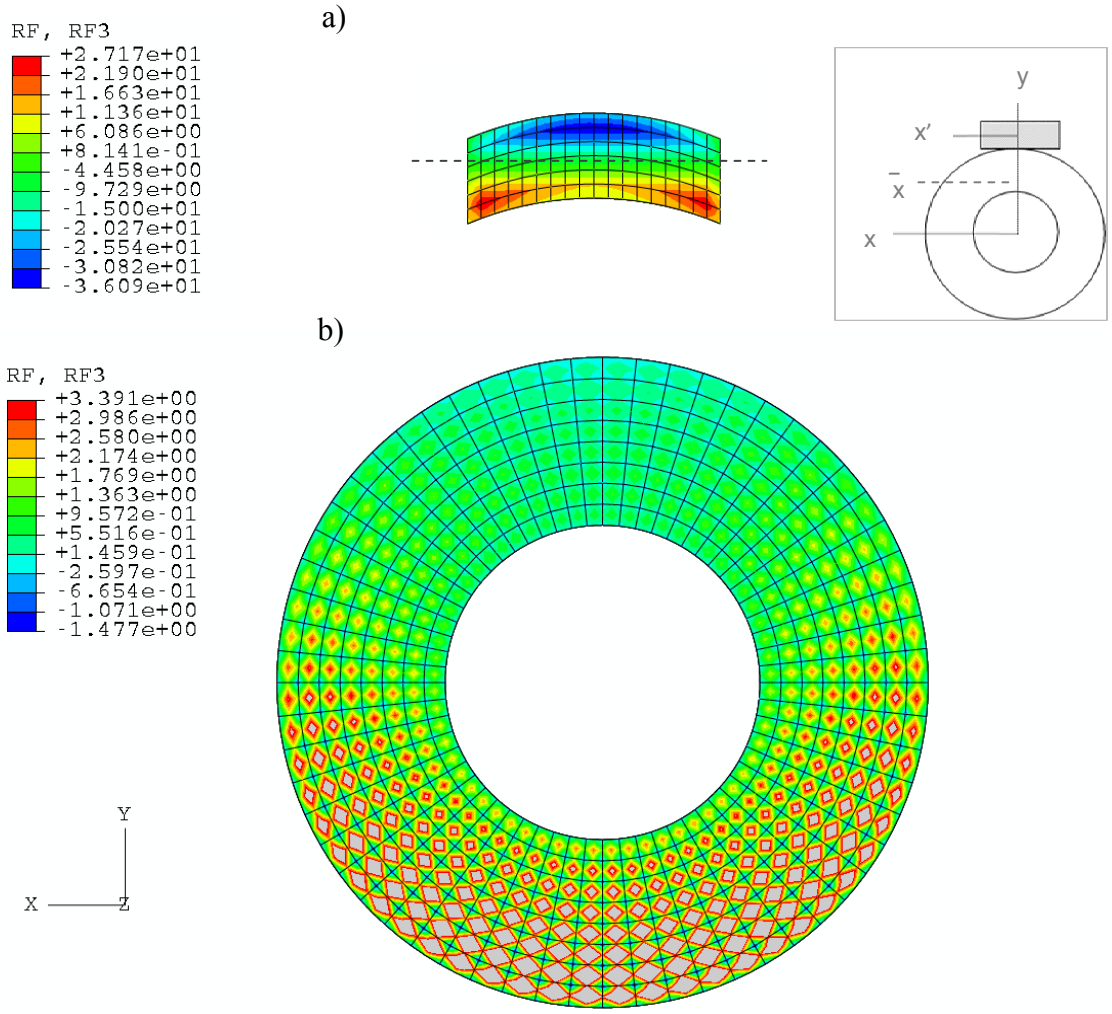

Figure 5.13. Contour plots of reaction forces (N) on the a) titanium plate and b) fracture, for the titanium plate model at day 0.

Figure 5.14a shows the logarithmic strain (true strain) normal to the z-direction, ε_{33}, for elements in the fracture zone as well as elements in the healthy bone adjacent to the fracture. The ε_{33} results are presented here because these strains are the largest strains occurring in the fracture zone, by an order of magnitude over the nearest component. In addition, when plotting the minimum principal strain contours, the strain values and contour are similar to those of the ε_{33} component, indicating the ε_{33} component is the primary component of the minimum principal strain.

As can be seen from Figure 5.14a, there is a gradient of ε_{33} through the y-direction, reflecting the displacements trends seen in Figure 5.12c. The maximum strains in the fracture zone occur towards the bottom, with a value of 30% strain in compression.

The contour of the normal stress in the z-direction, σ_{33}, in the bone and screws are shown in Figure 5.14b. First, estimating σ_{33} using $P/A + Mc/I$ for the outer surface of the bone ($c = \pm 15.5$ mm) results in values of -6.57 MPa and 5.17 MPa. The results from the model predict a stress at point A in Figure 5.14c of 5.1 MPa, and -6.3 MPa at point B, corresponding to the stresses estimated using the closed-form solution.

At locations C and D in Figure 5.14c, areas in the healthy bone near the fracture, the stress values are -0.27 MPa and -3.5 MPa, respectively; these values indicate the loads are reduced in these areas and are carried by the titanium plate. In addition, screw IV experiences stresses of 90 MPa and -45 MPa in areas where it is tied to the fixation plate. The stresses in screws II and III are a maximum of ~10 MPa and 12 MPa in screw I, indicating the majority of the load transfer is occurring in screw IV.

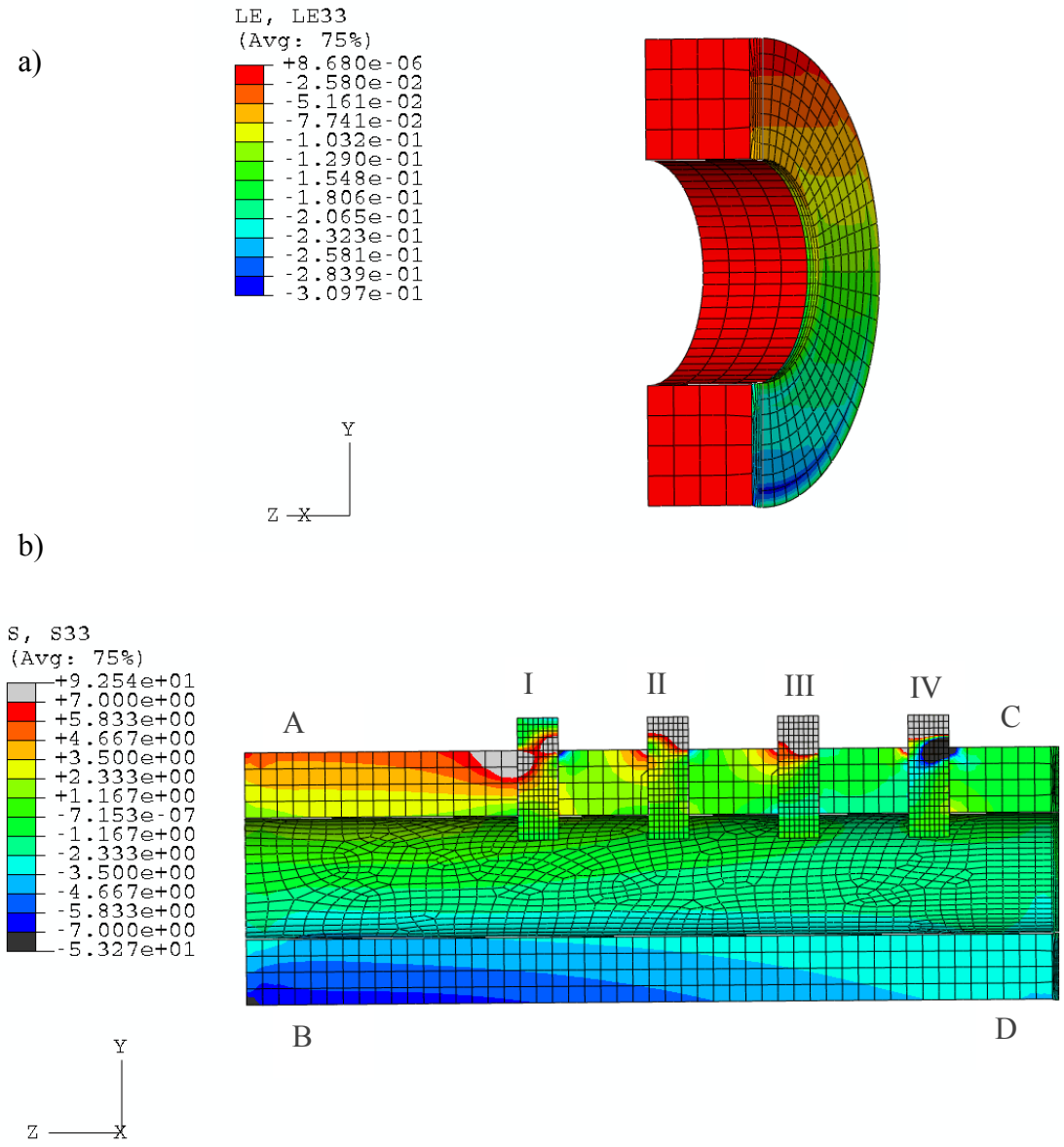

Figure 5.14. Contour plots of the logarithmic (true) strain in the 33-direction of a) elements immediate to the fracture and b) bone and screws for the titanium plate attached to the idealized femur at week 0.

The contours of the normal stress in the z-direction, σ_{33}, in the titanium plate are shown in Figure 5.15. Here it is seen the highest stresses occur in location between the hole IV and the fracture, consistent with the observations that the majority of the load is transferred through screw IV. In addition, maximum tensile stresses of 98 MPa occur at location A and the maximum compressive stresses of 84 MPa occur at location B, consistent with the reaction forces seen in Figure 5.13a. Additionally, these stresses are within the yield stress of ~140 MPa for pure titanium, indicating no yielding will occur in the plate.

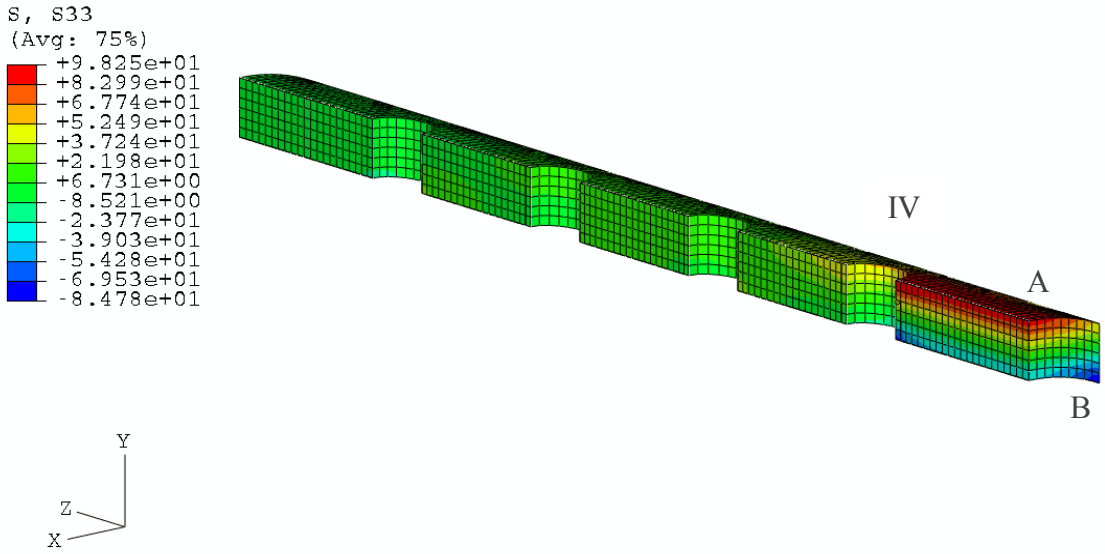

Figure 5.15. Stress contours (MPa) in the 33-direction on the titanium plate in the day 0 model.

5.6.2 HA/P/C Plate – 4 mm x 12 mm

The x-translation and y-translation contours are plotted in Figure 5.16 for the HA/P/C plate 1 model at day 0. When looking at the x-translations, it is seen that the trends in these values are unlike those seen in the titanium plate model in Figure 5.12a. Although the maximum u_3 in the –z-direction in this model is -0.34 mm compared to that of -0.26 mm for the titanium plate, the maximum u_3 in the +z-direction here is 0.13 mm, whereas the maximum for the titanium model is 0.002 mm. These values and gradient of u_3 translations are consistent with bending deformations. Additionally, the maximum u_2 in the HA/P/C model is -1.1 mm, compared to that of -0.7 mm for the titanium plate model.

The reaction forces in the z-direction, $R_{f,3}$, for the plate and fracture are plotted in Figure 5.17. It is seen that all of the $R_{f,3}$ values in the plate are negative, indicating a state of tension throughout the plate. This state is entirely different than that of the titanium plate shown in Figure 5.13a, where the forces pass through zero at the dotted line, indicating a state of bending in the plate. This difference can be explained when determining the neutral axis of the composite section with the HA/P/C plate, using Equation 5.1. This value of $\bar{x}$ is found to be 16.5 mm, which still lies in the plate. Although this calculation for the composite neutral axis indicates that bending should be taking place in the HA/P/C plate, it should be noted Equation 5.3 is an estimation since the geometry of the plate is idealized as rectangular. In addition, the moment is applied at the bone centroid, so effects of the application of the moment offset from the composite neutral axis could be contributing to reaction force results.

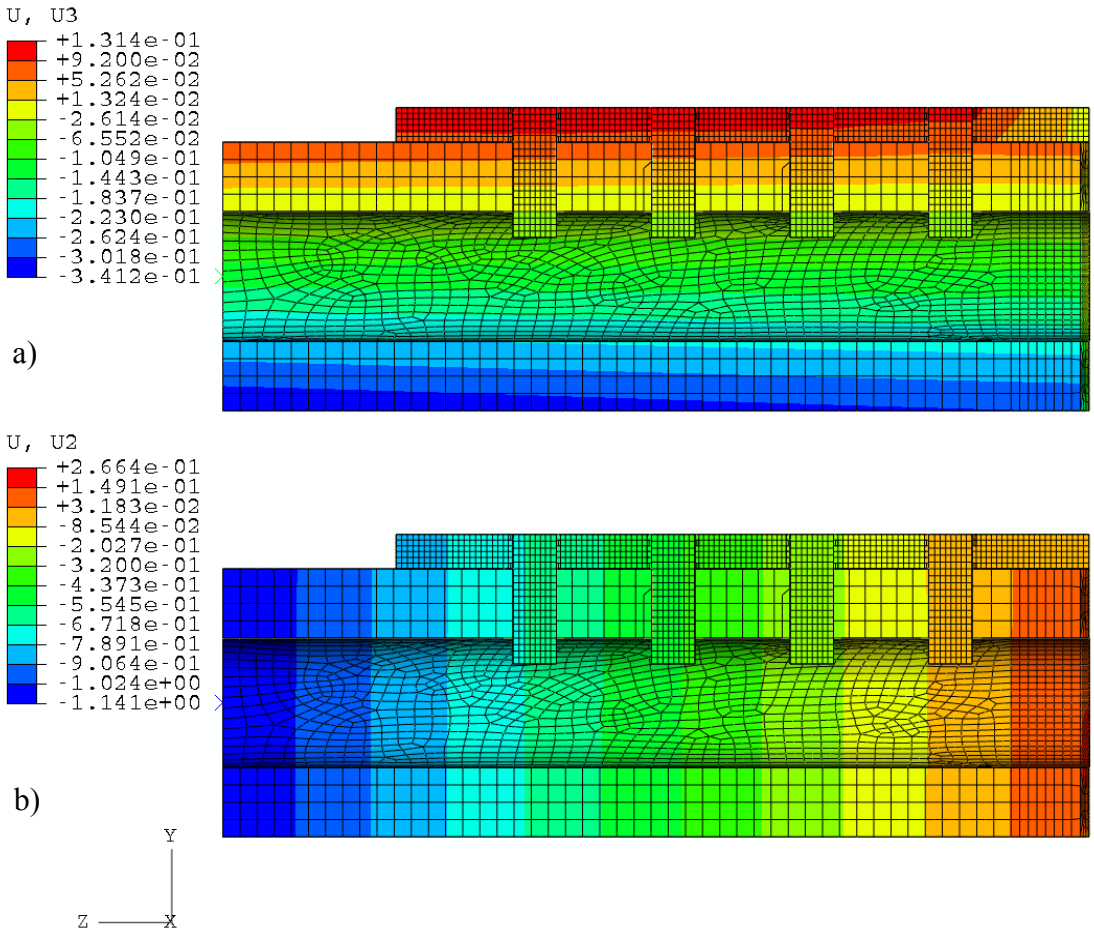

Figure 5.16. Translation contour plots for the HA/P/C plate 1 model at day 0.

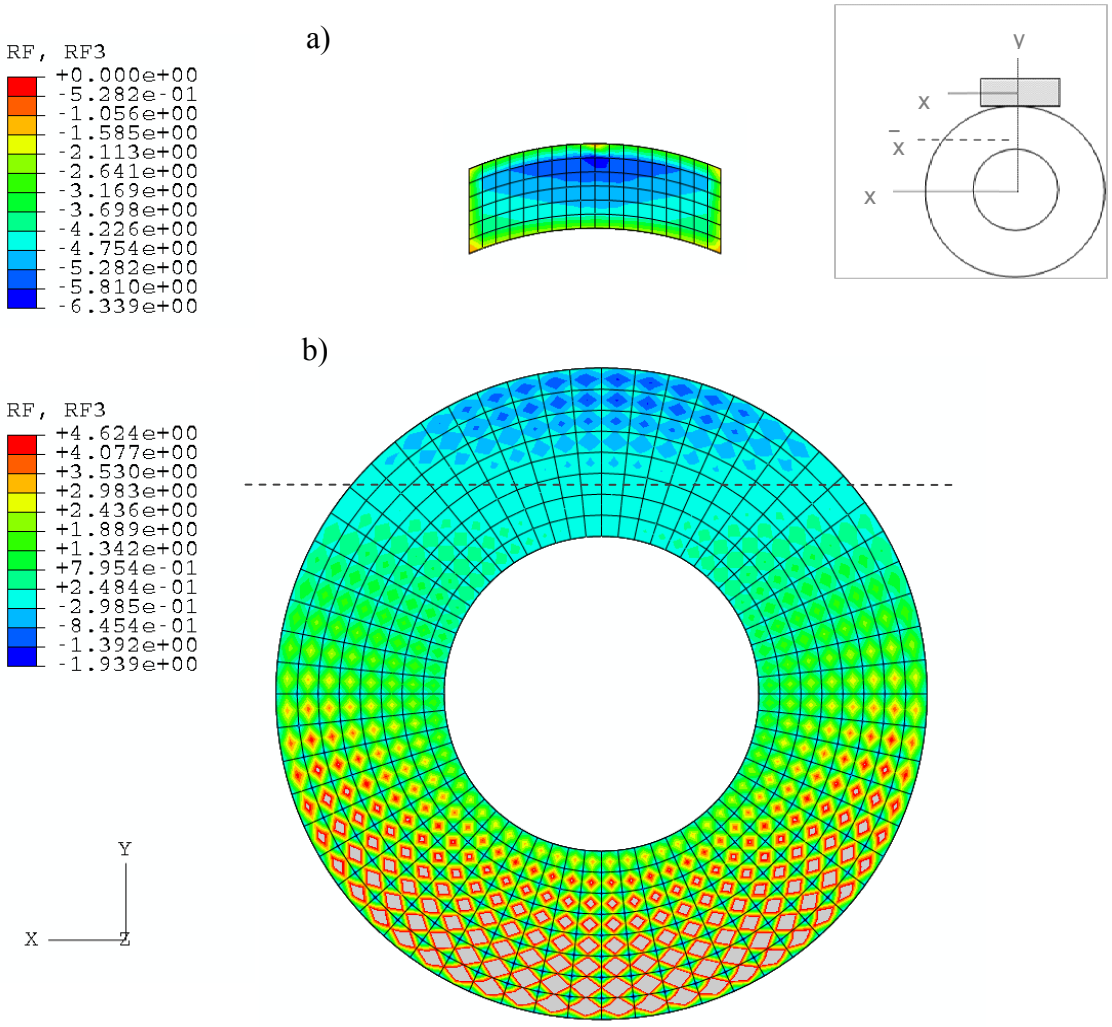

Figure 5.17. Contour plots of reaction forces (N) on the a) HA/P/C plate, and b) fracture, for the HA/P/C plate 1 model at day 0.

The logarithmic strain (true strain) normal to the z-direction, ε_{33}, for the fracture elements and adjacent elements are shown in Figure 5.18a. Again the same gradient of ε_{33} through the y-direction is seen here, similar to the results of the titanium model shown in Figure 5.14a. The maximum strains in the fracture zone in this HA/P/C model are about 42% strain in compression, compared to the ~30% maximum strain observed in the titanium model. In addition, in comparing the contour values between the two models, it is seen that at the same location in the fracture, the strain values in the HA/P/C model are about twice those of the titanium model's.

In looking at the σ_{33} contours of the bone and screws shown in Figure 5.18b, it is seen that the stress values are locations C and D are -0.24 MPa and -4.7 MPa, respectively. Compared to those in the titanium model in Figure 5.14b, -0.27 MPa and -3.5 MPa, it is seen that elements adjacent to the fracture carry more load in this HA/P/C model. This is consistent with the higher strains experienced in the fracture in this model compared to those in the titanium model. Additionally, there are less stress gradients through the bone and screw interfaces in screws I, II, and III in the HA/P/C results shown in Figure 5.18b, when compared to the stress gradients seen in the titanium plate results in Figure 5.14b. This indicates the load transfer is shared more evenly in the screws when the HA/P/C plate is used, whereas the load transfer is seen to occur primarily through screw IV when the titanium plate is used.

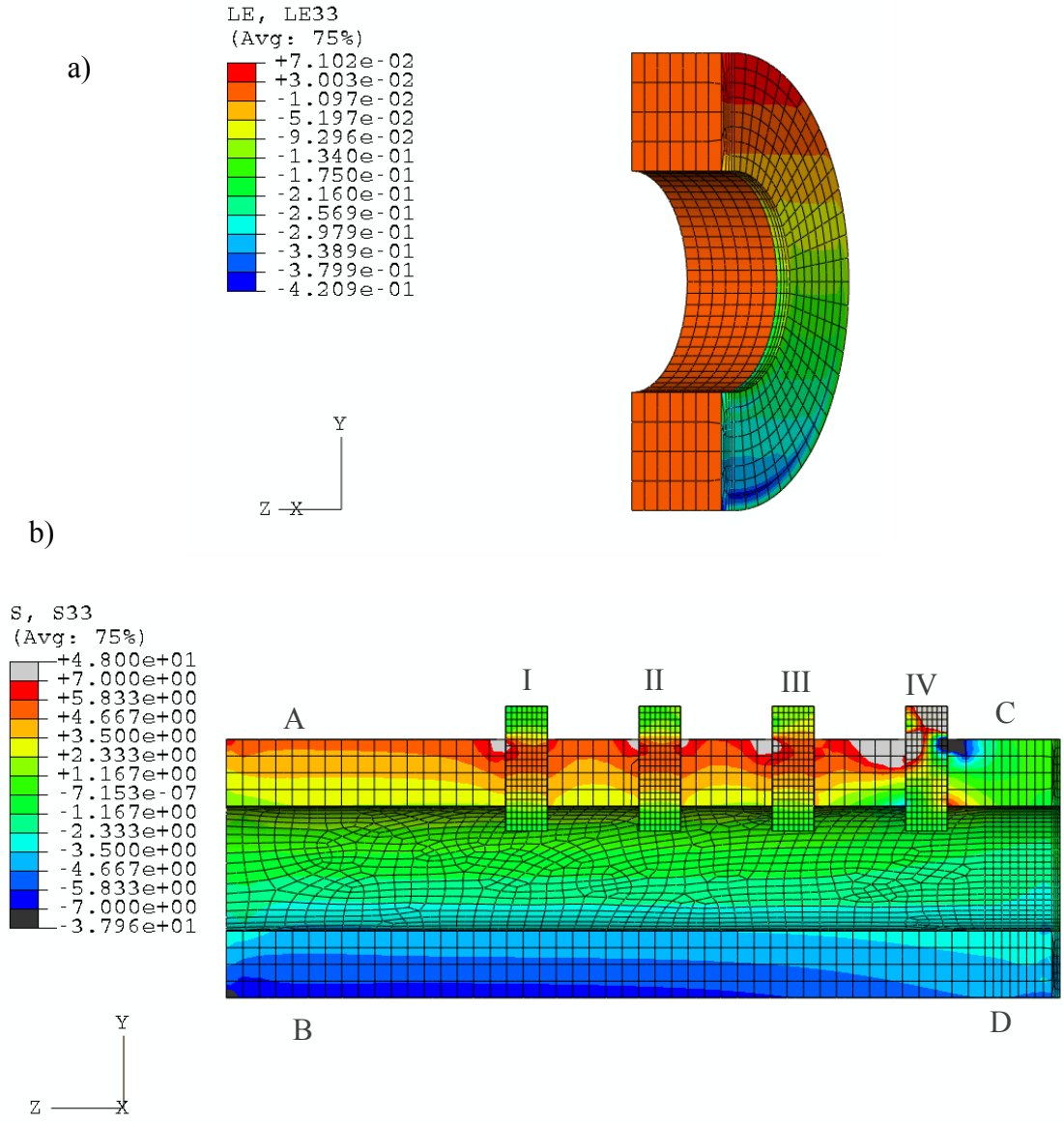

Figure 5.18. Contour plots of the logarithmic (true) strain in the 33-direction of a) elements immediate to the fracture and b) bone and screws for the HA/P/C plate 1 model at day 0.

The contours of the normal stress in the z-direction, σ_{33}, in the titanium plate are shown in Figure 5.15. Here it is seen the highest stresses occur in location between the hole IV and the fracture, consistent with the observations that the majority of the load is transferred through screw IV. In addition, maximum tensile stresses of 98 MPa occur at location A and the maximum compressive stresses of 84 MPa occur at location B, consistent with the reaction forces seen in Figure 5.13a. Additionally, these stresses are within the yield stress of ~140 MPa for pure titanium, indicating no yielding will occur in the plate.

The normal stress and strain contours of the HA/P/C plate are shown in Figure 5.19. The largest strains of 13000 μm/m occur in the elements adjacent to screw IV. Although these values exceed the strain allowable of HA/P/C found in Section 4, they are a result of the idealized treatment of the screws attached to the bone plate. The strain in the elements that bridge the fracture are approximately 6500 μm/m, within the allowable.

a)

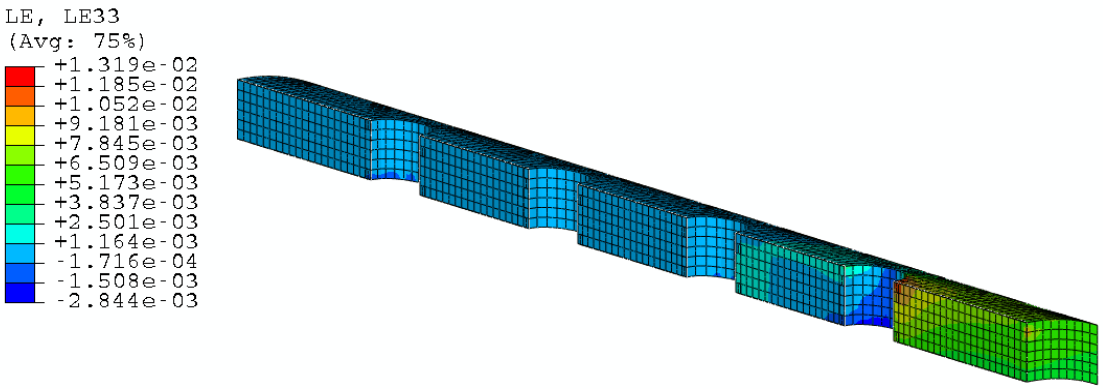

b)

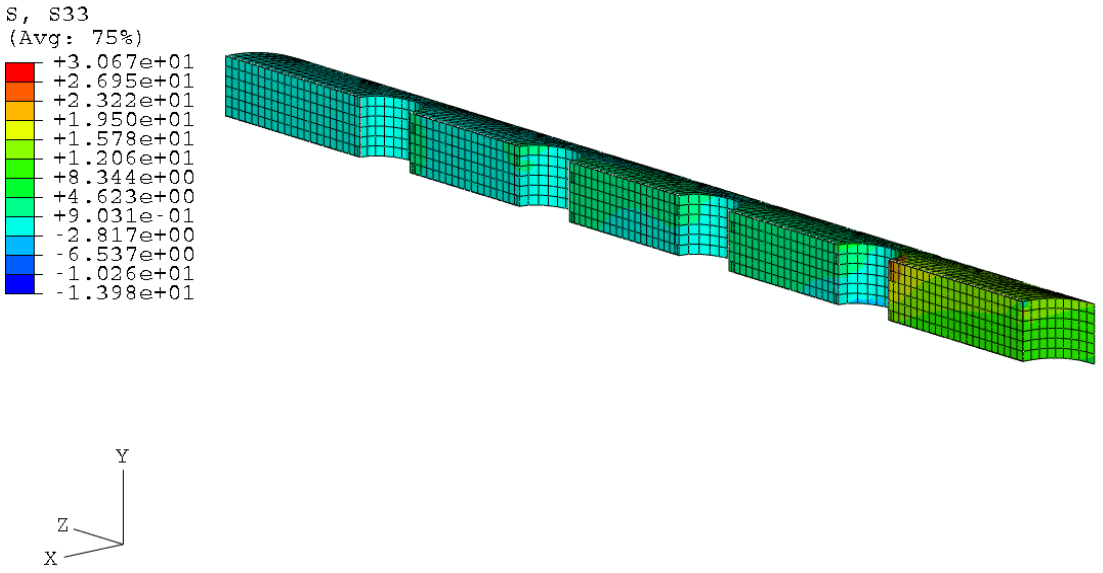

Figure 5.19. Stress (MPa) and strain contours in the 33-direction in the HA/P/C plate 1 at day 0.

5.6.3 HA/P/C Plate – 6 mm x 20 mm

The x-translation and y-translation contours are plotted in Figure 5.20 for the HA/P/C plate 2 model at day 0. Again, the trends are similar to those reported for the HA/P/C plate 1 in Figure 5.12. Compared to the results for the HA/P/C plate 1 shown in Figure 5.16, the results here indicate a stiffer system; this is expected because the HA/P/C plate 2 is 6 mm x 20 mm compared to the plate 1 geometry of 4 mm x 12 mm.

The reaction forces in the z-direction, $R_{f,3}$, for the plate and fracture are plotted in Figure 5.21. In this model, the reaction forces seen in the plate are both positive and negative. This trend indicated that this HA/P/C plate is in a state of bending, unlike the smaller HA/P/C plate. Again, this can be attributed to the location of the composite neutral axis. Because of the larger dimensions of this plate, the composite neutral axis $\bar{x}$ estimated by Equation 5.3 is located at 18.1 mm, whereas the plate neutral axis x' is located at 18.5 mm (inset of Figure 5.21).

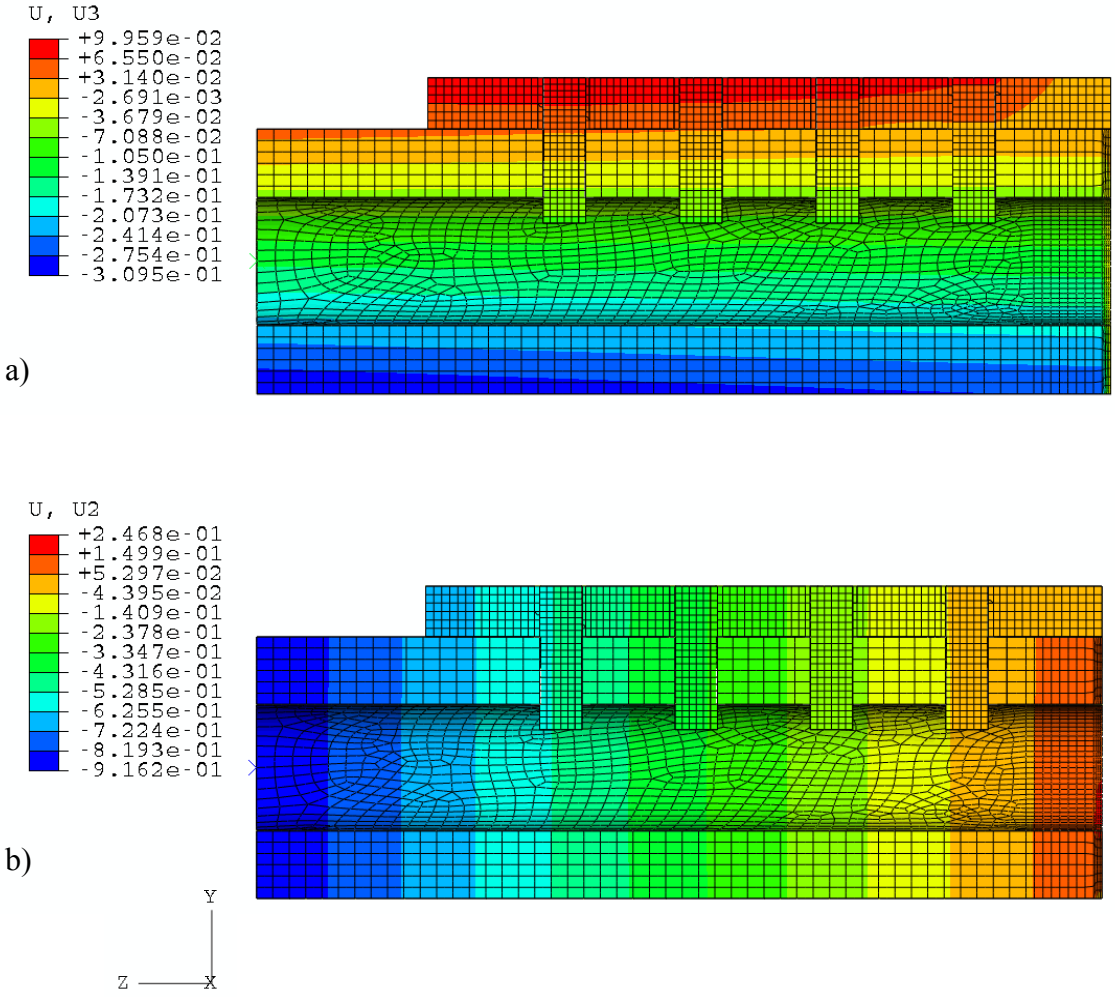

Figure 5.20. Translation contour plots for the 6 mm x 20 mm HA/P/C plate at day 0.

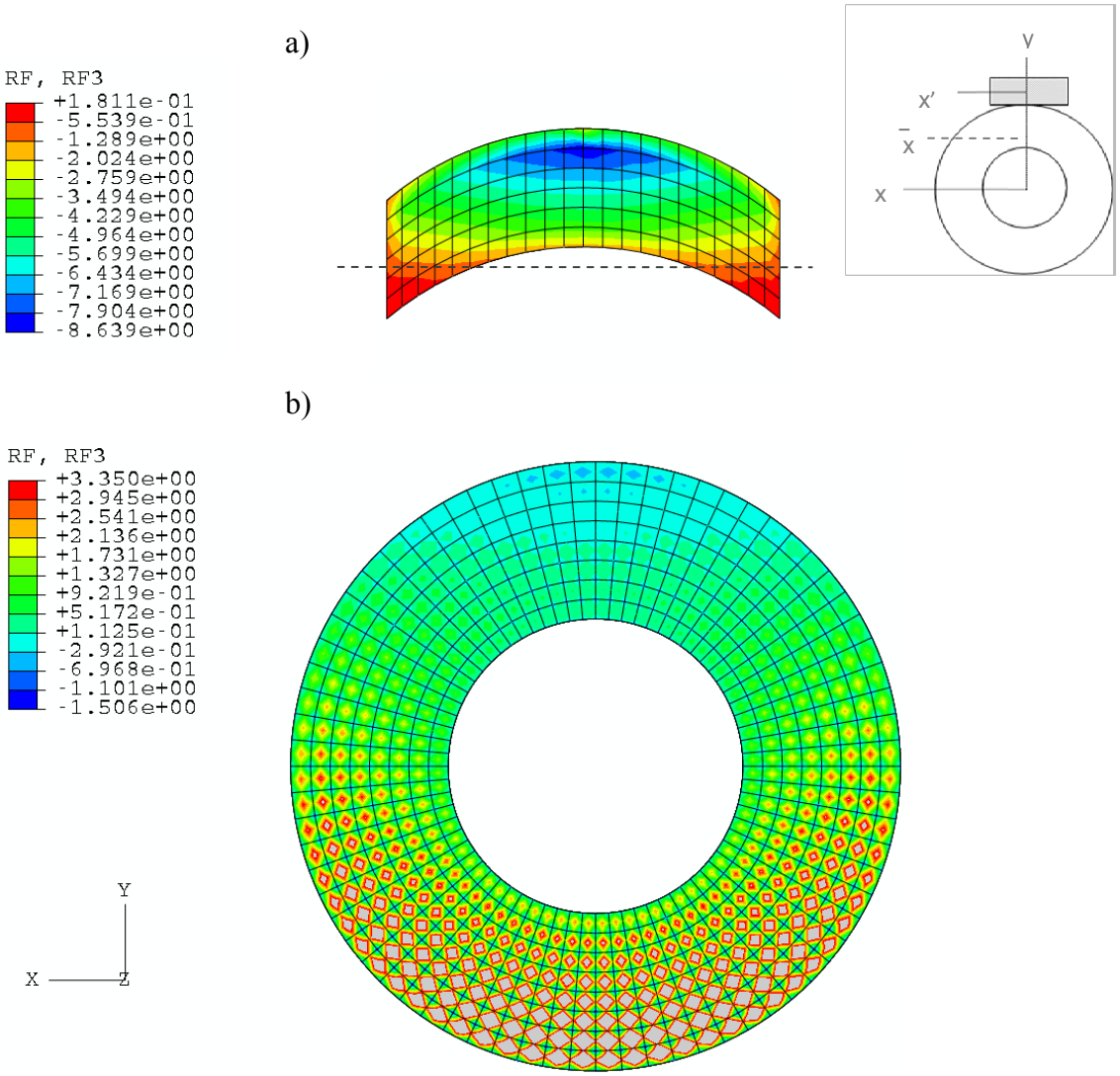

Figure 5.21. Contour plots of reaction forces (N) on the a) HA/P/C plate, and b) fracture, for the 6 mm x 20 mm plate at day 0.

The logarithmic strain (true strain) normal to the z-direction, ε_{33}, for the fracture elements and adjacent elements are shown in Figure 5.22a. Again the same gradient of ε_{33} through the y-direction is seen here, similar to the results of the titanium and HA/P/C plate 1 models. Even though this HA/P/C is larger in comparison to the HA/P/C plate 1, the maximum strains and strain gradients in the fracture of the two models are similar, as can be seen in a comparison of Figure 5.22a and Figure 5.18a. Intuitively, one would expect the larger plate to result in more load carrying capacity, and thus smaller strains in the fracture. However, the fracture represents a large discontinuity in properties from the healthy bone, so this could influence the results in the fracture. In addition, the fracture is modeled with linear elastic properties, which is just an approximation for the fracture properties, especially when high strains are experienced.

In looking at the σ_{33} contours of the bone and screws shown in Figure 5.22b, similar observations are made as those in the HA/P/C plate 1 model: 1) there are less stress gradients through the bone and screw interfaces in screws I, II, and III, indicating a more distributed load transfer through all screws, as opposed to the load transfer primarily through screw IV in the titanium plate model, 2) slightly higher stresses are seen near the fracture, indicating the fracture is carrying more load as compared to the titanium plate fracture.

When looking at the strain contours in the plate in Figure 5.23, it is seen that the strain in the elements that bridge the fracture ranges from 3600 μm/m to -1000 μm/m, within the allowable. In addition, the larger plate results in a smaller strain at screw IV than that seen in the previous plate, 6900 μm/m versus 13000 μm/m.

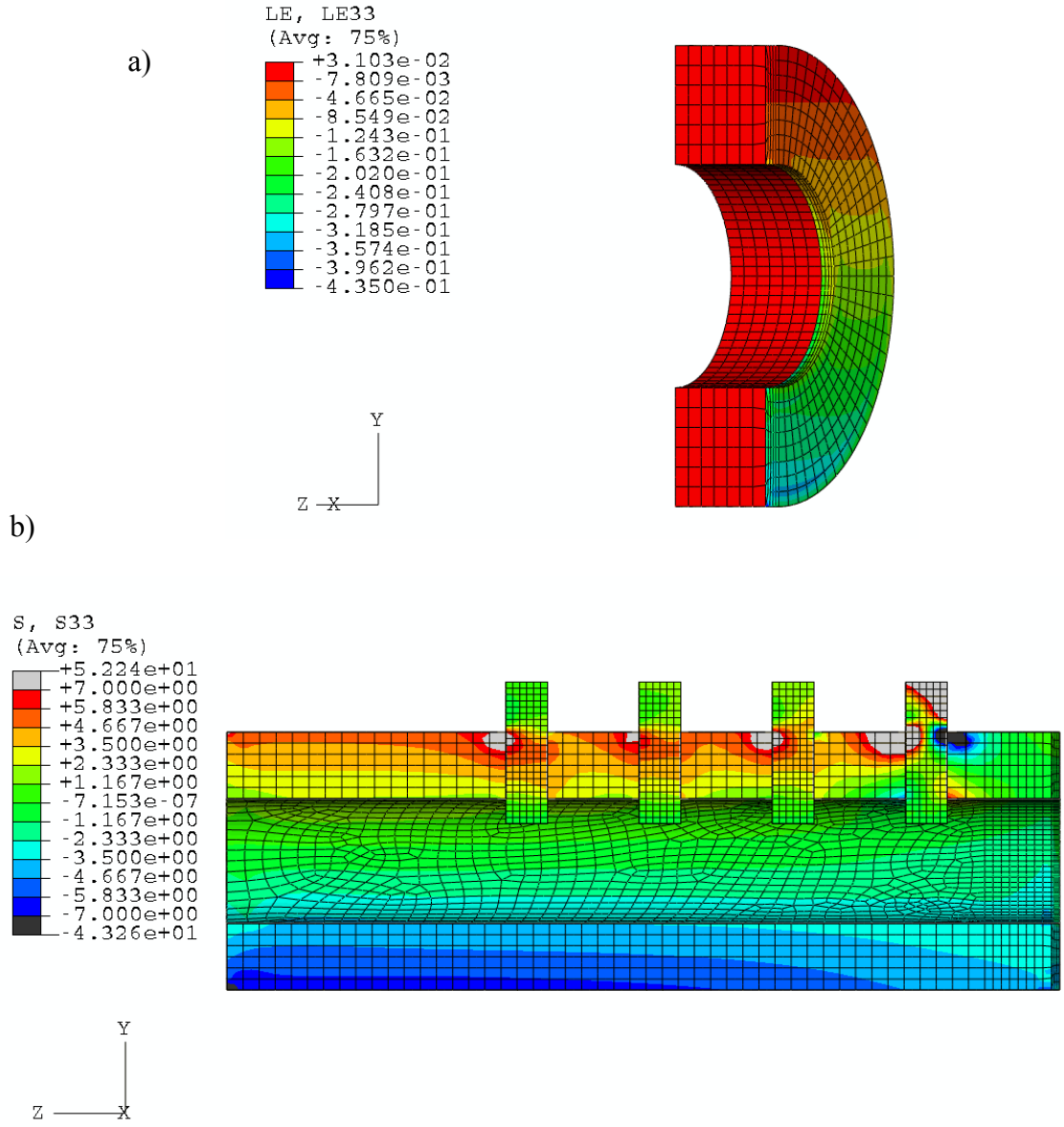

Figure 5.22. Contour plots of the logarithmic (true) strain in the 33-direction of a) elements immediate to the fracture and b) bone and screws for the HA/P/C plate 1 model at day 0.

a)

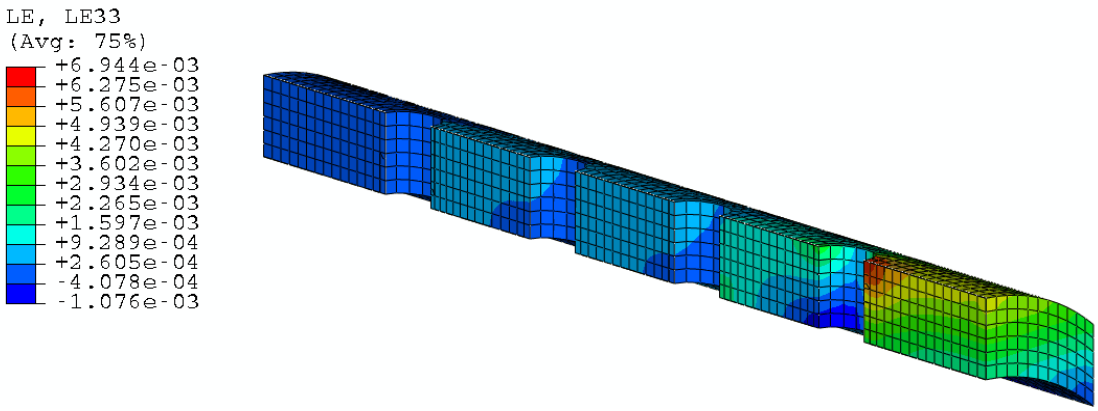

b)

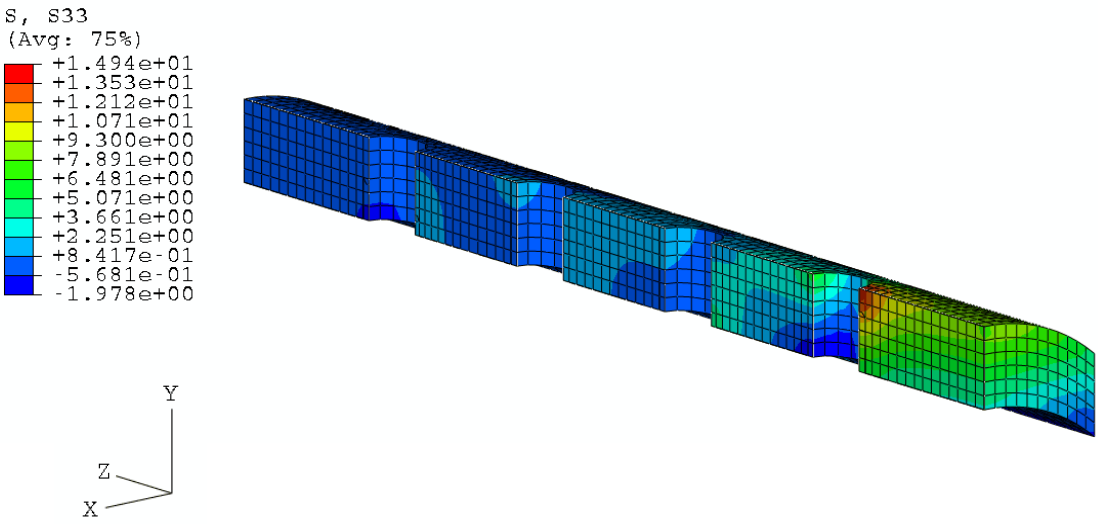

Figure 5.23. Stress (MPa) and strain contours in the 33-direction in the HA/P/C plate 1 at day 0.

5.6.4 HA/P/C Plate at Day 35

This model incorporates the effects of dissolution of the HA/P/C fixation plate as well as the healing rate in the interfragmentary gap. Recalling from Table 5.1, the dissolution depth after 35 days is 0.47 mm while the modulus of the fracture is 990 MPa (compared to the modulus of 10 MPa at day 0).

The y-translation and z-translation contours are plotted in Figure 5.24 for the HA/P/C plate where dissolution and healing properties for day 35 are used. The maximum values of u_3 displacements in this model are smaller than those seen in the day 0 model (Figure 5.16) by an order of magnitude (+0.03 mm and -0.04 mm compared to +0.1 mm and -0.3 mm). The u_2 displacements are smaller by an order of magnitude as well.

The reaction forces in the z-direction, $R_{f,3}$, for the plate and fracture in this model are plotted in Figure 5.25. In addition, the inset in the figure illustrates the elements where dissolution has taken place; these elements are depicted in blue and are assigned properties of the carbon foam. When looking at the $R_{f,3}$ of the plate, it is seen all values are negative, indicating a state of tension through elements on this surface. It is also seen that the $R_{f,3}$ values are near zero in the elements where only carbon foam exists, indicating those elements are taking relatively little load as compared to the remaining HA/P/C elements (elements in yellow in the inset). The sum of $R_{f,3}$ on the plate is -45.2 N.

The reaction forces of the bone shown in Figure 5.25 reveal both positive and negative values, with magnitudes order larger than those seen in the plate. Again, the

elements near the bottom-half of the cross-section experience positive reaction forces and those near the top-half experience negative reaction forces, consistent with a state of bending. The total sum of the reaction forces on the bone is 449.8 N, indicating the bone at this stage of healing takes the majority of the applied load.

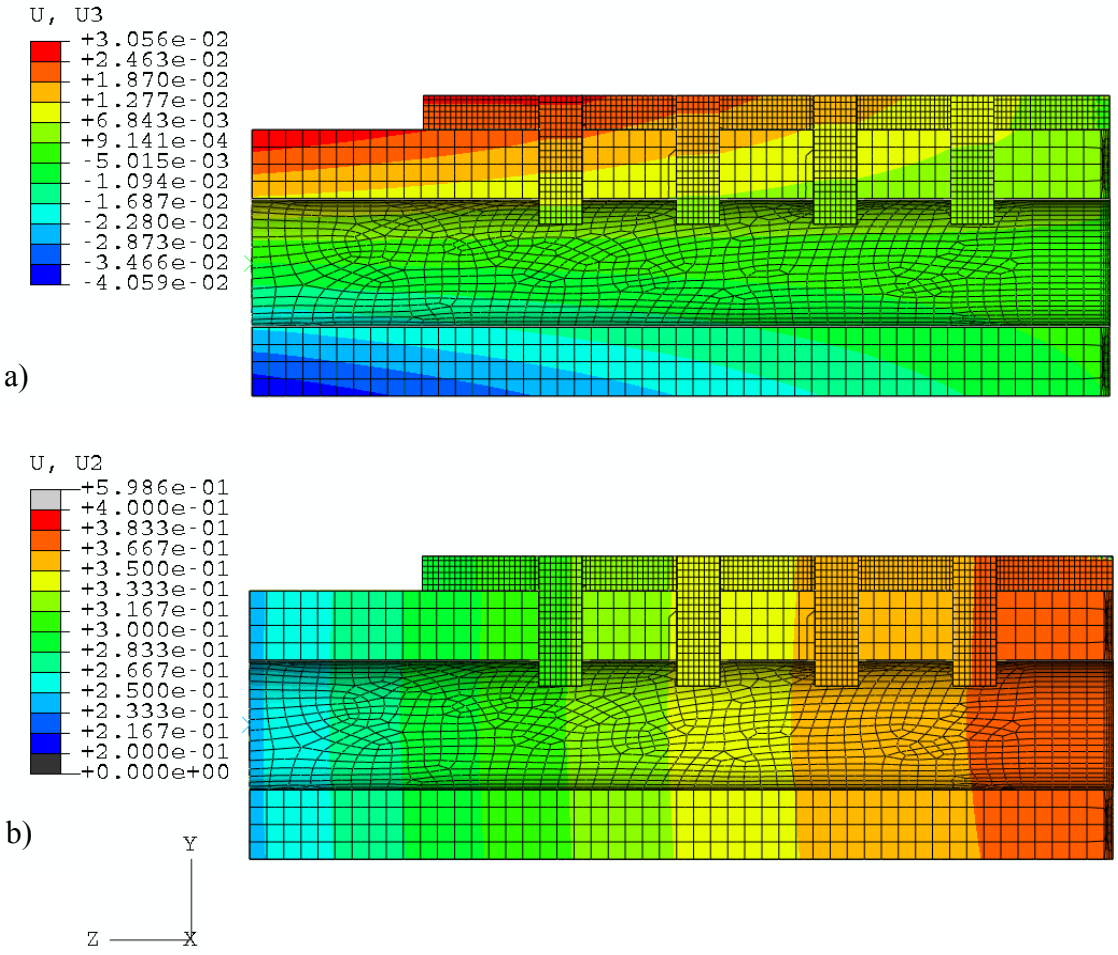

Figure 5.24. Translation contour plots for the HA/P/C plate 1 model at day 35, incorporating the effects of dissolution and healing rate ($E_{fracture}$ of 990 MPa and dissolution depth of 0.47 mm).

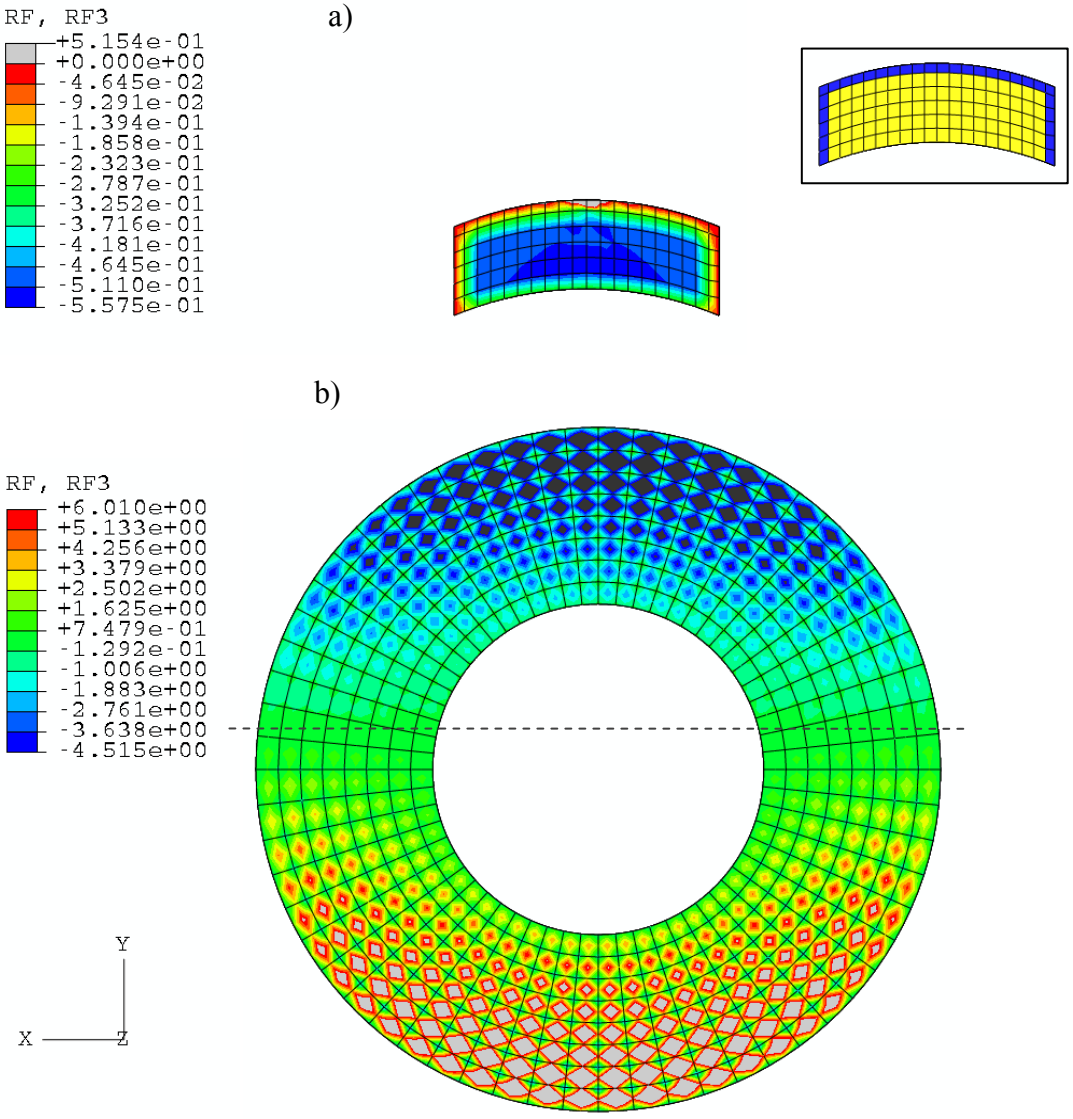

Figure 5.25. Contour plots of reaction forces (N) on the a) HA/P/C plate, and b) fracture, for the HA/P/C plate 1 model at day 35. The inset shows the dissolution zone of the plate cross-section in blue, where those elements are assigned properties of the carbon foam.

In looking at the strains in the fracture area, as shown in Figure 5.26, it is seen that the strains are consistent with bending from the applied moment. Here, it is confirmed that the elements in the upper-half of the interfragmentary gap are in tension while those in the lower-half are in compression. In addition, although the majority of the load is supported by the fracture in this model, as evident by the reaction force observations, the maximum strain in the fracture is still two orders of magnitude less than those seen in the model at day 0 in Figure 5.18.

In looking at the σ_{33} contours of the bone and screws shown in Figure 5.26b, it is observed that the stress gradients bone/screw interfaces are more uniform when compared to the gradients of the model at day 0 in Figure 5.18b. This is especially evident when comparing the stresses at screw IV and location C in both models. In addition, the stress values and gradients at locations A and C are similar in this model, as well as the values and gradients at locations B and D. This is further evidence that the bone transfers the majority of the applied moment and axial load.

Investigating the ε_{33} distribution in the plate as shown in Figure 5.27 reveals the strains in the plate are about the same between screws I, II, and III. The strains at these locations, marked as A, B and C in the figure are: 350 μm/m, 379 μm/m, and 399 μm/m, respectively. The concentration at location D has a value of about 1000 μm/m. The strain at location E, where the plate bridges the interfragmentray gap, is 608 μm/m. The highest strain seen in the foam is 1140 μm/m (this is aside from the computational concentrations arising from constraining the single point for convergence purposes). All of these values are within the 10,000 μm/m allowable for both the foam and HA/P/C, as predicted in Section 4.

The σ_{33} distribution of the plate is also presented in Figure 5.27 to illustrate the discontinuity in stresses between the carbon foam elements and the HA/P/C elements. As seen from the strain distribution, the strains in the plate are continuous, which is expected. However, since the carbon foam modulus is smaller by two orders of magnitude than the HA/P/C modulus (40 MPa compared to 2000 MPa), the stresses in the carbon foam are much smaller, leading to the observed discontinuity.

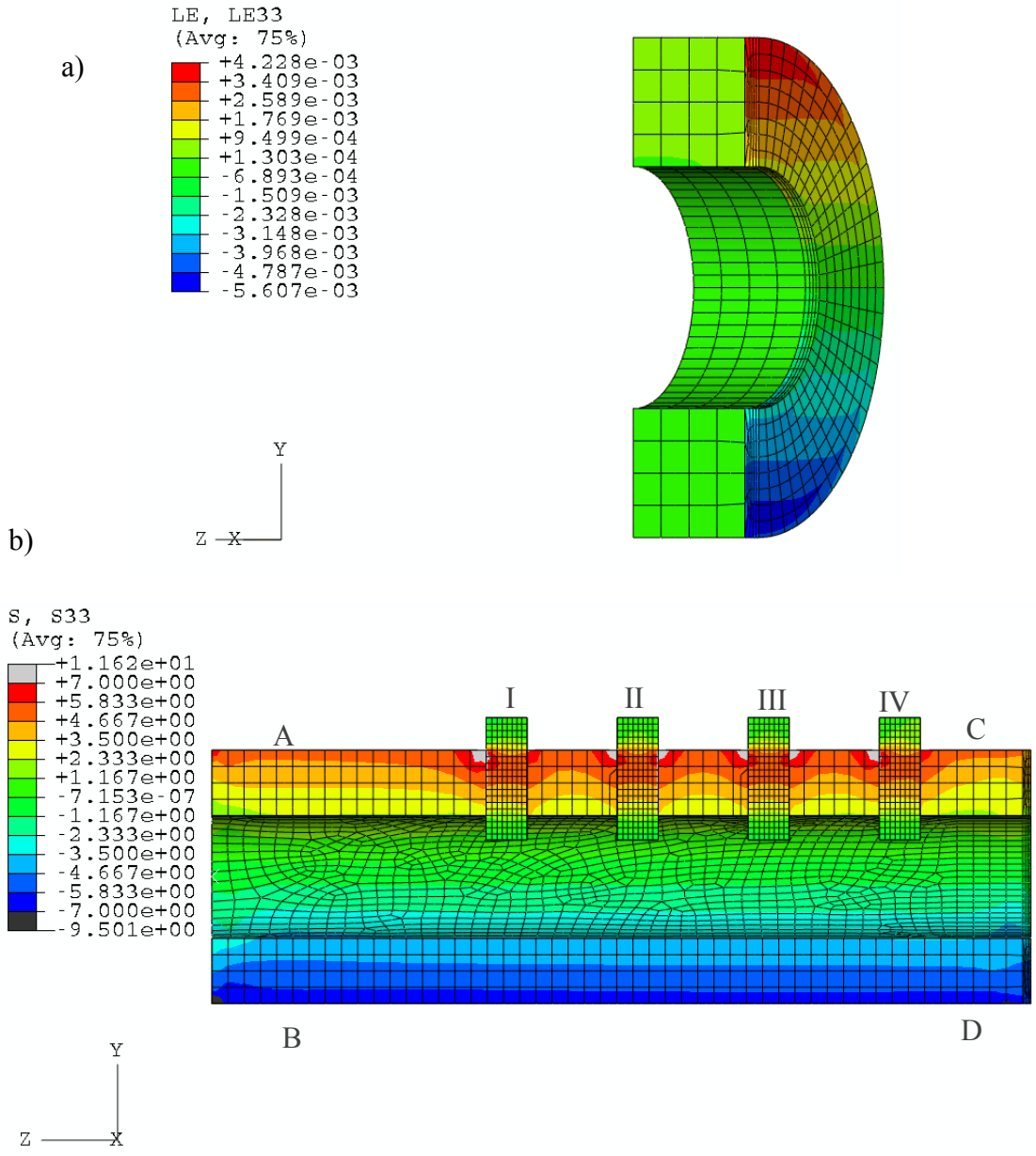

Figure 5.26. Contour plots of the logarithmic (true) strain in the 33-direction of a) elements immediate to the fracture and b) bone and screws for the HA/P/C plate 1 model at day 35.

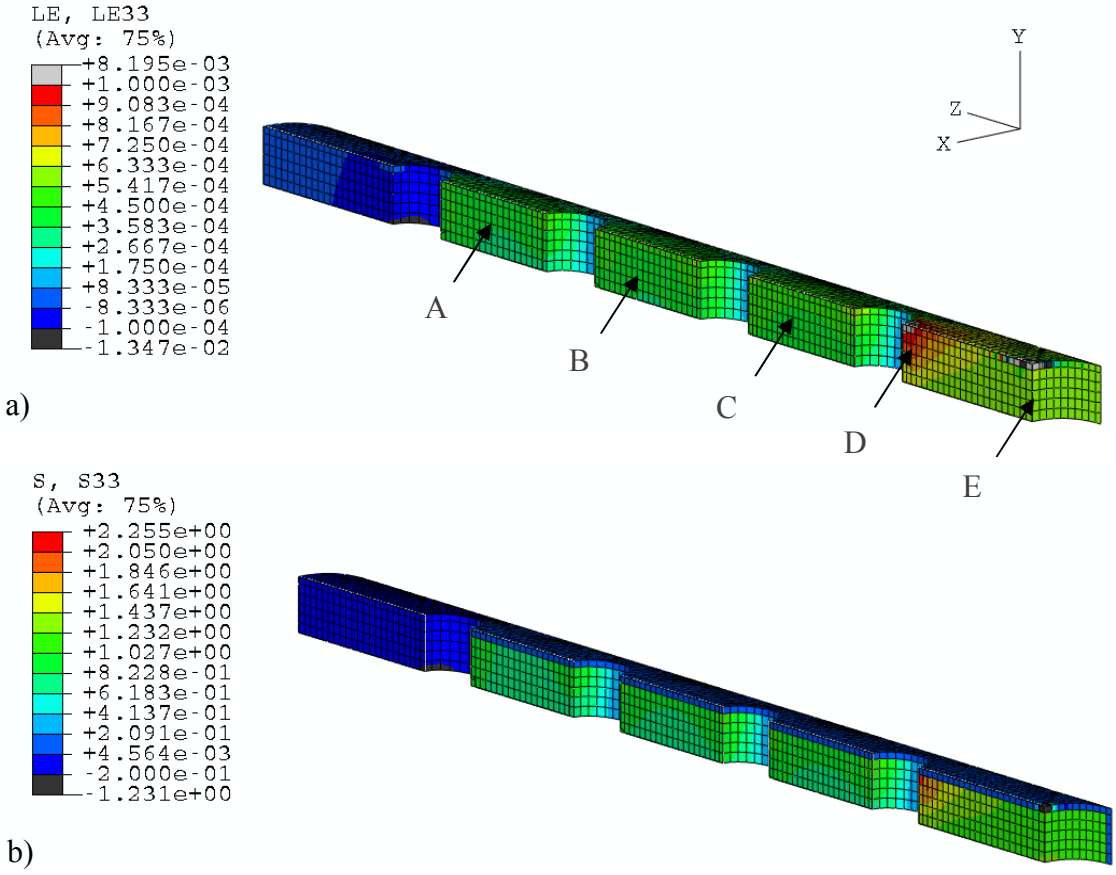

Figure 5.27. Strain and stress (MPa) contours in the 33-direction in the HA/P/C plate at 35 days.

5.6.5 Delayed Healing Model

The logarithmic strain normal to the z-direction, ε_{33}, is presented in contour plots in Figure 5.28 for the fracture elements as well as the HA/P/C plate (6 mm x 20 mm cross-section). In looking at the strains in the fracture area, it is seen that the strains are consistent with bending from the applied moment. Here, the elements in the upper-half of the interfragmentary gap are in tension while those in the lower-half are in compression. The maximum tensile strain experienced is 1.2 % while the maximum compressive strain is 1.7 %.

When investigating the strain contours in the plate, it is seen that the strain in the elements at point B is 1085 μm/m, within the allowable of 10,000 μm/m. Additionally, the strain at point A is 1500 μm/m; this increased strain value is caused by the concentrations arising from the constraints used to simulate the screw attachment.

It is also noted the strain concentrations at point C in the plate are a result of the fixed displacement boundary conditions imposed on the single node at the point. Since this fixed node is part of an element which undergoes dissolution, the resulting decrease in modulus in this constrained element leads to increased stress/strain concentrations in this element and as well as adjacent elements. An alternate model is run where the fixed node is located in the healthy bone (100 mm away from the fracture); the strain results in the fracture and plate in this model are shown in Figure 5.29. It is seen that the strains in the fracture are comparable to those in Figure 5.28. In addition, changing the location of the fixed node results in no concentrations at point C in Figure 5.29. Here, the strain is observed to be ~1200 μm/m, still well within the strain allowable.

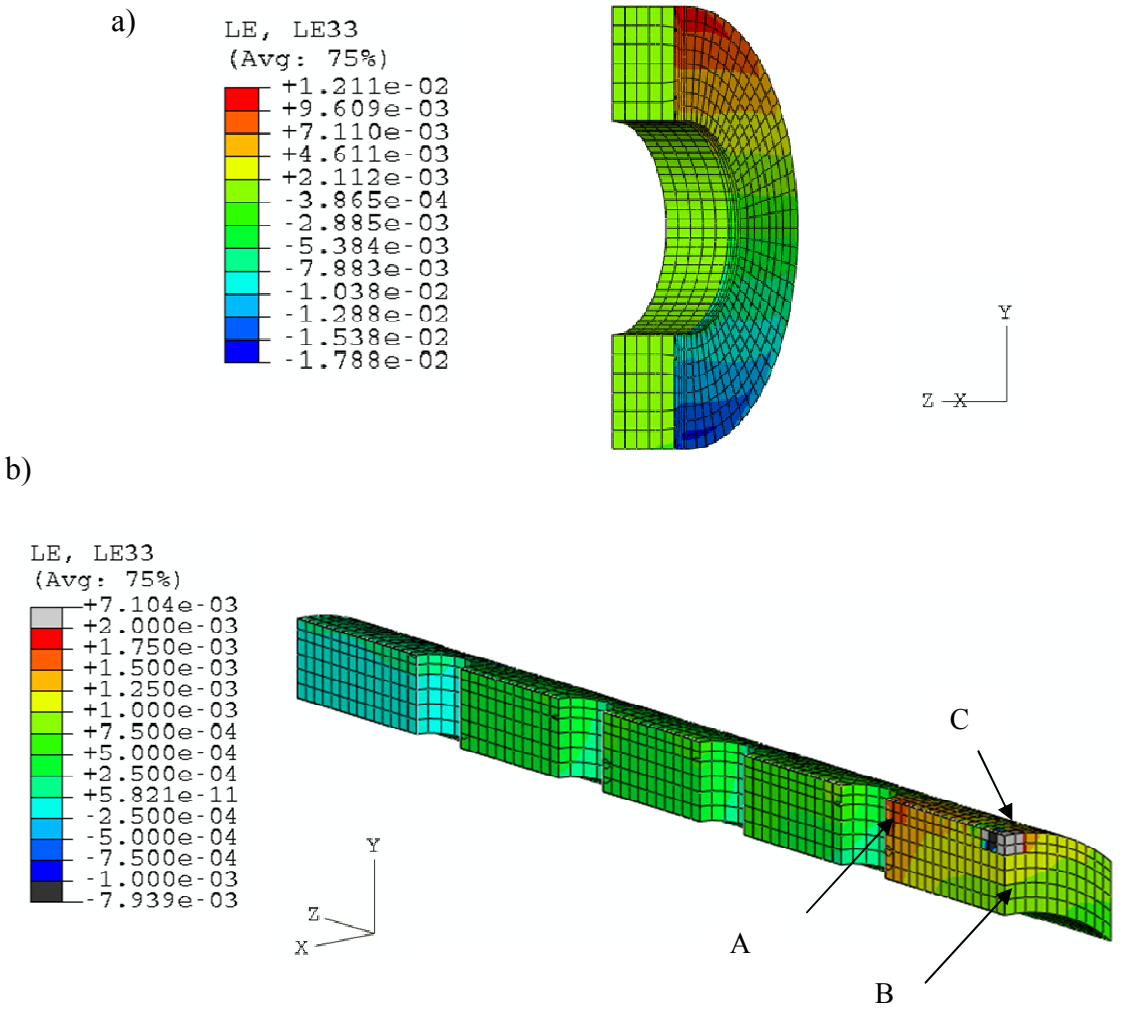

Figure 5.28. Strain contours in a) fracture and b) HA/P/C plate at 42 days with healing delayed by two weeks.

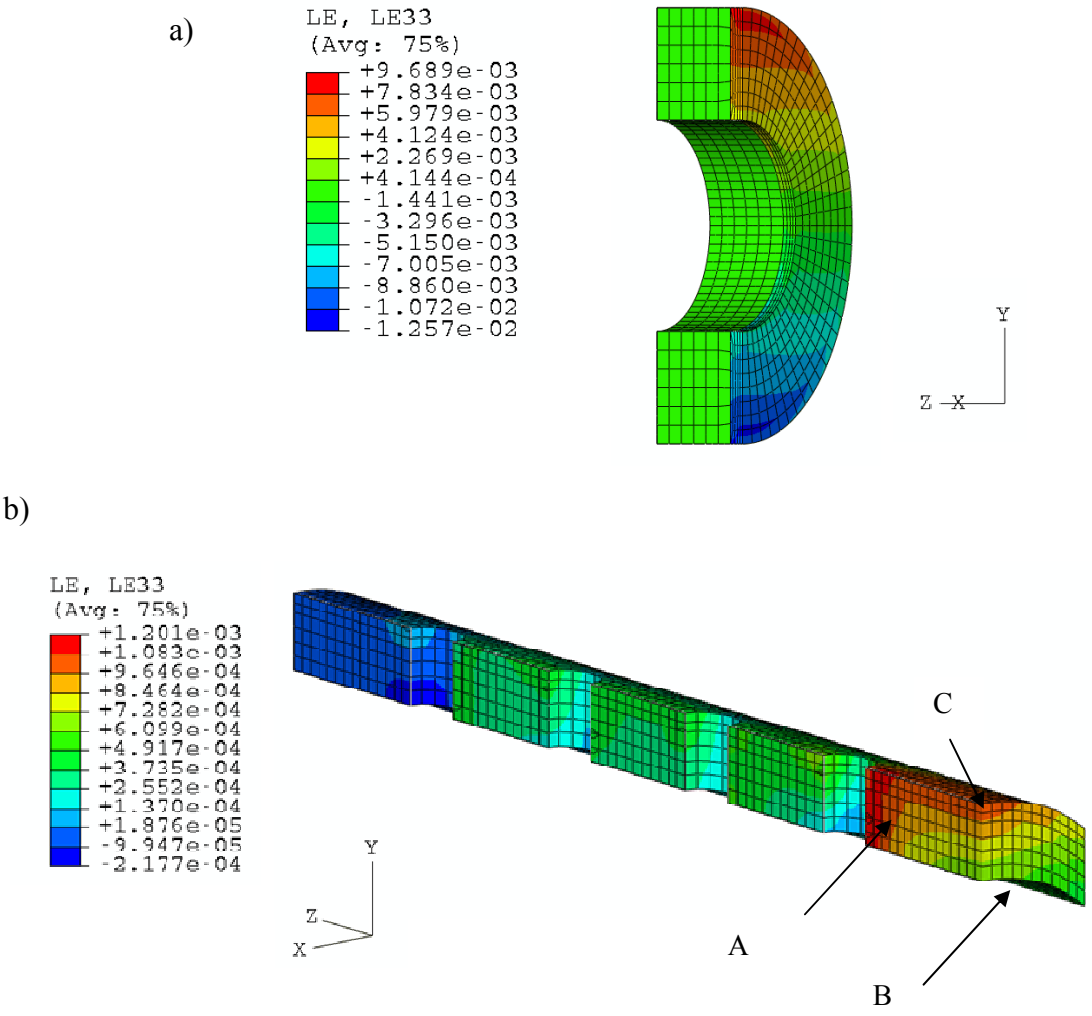

Figure 5.29. Strain contours in a) fracture and b) HA/P/C plate at 42 days with healing delayed by two weeks, where the fixed node is located in an element with healthy bone properties, far from the fracture.

5.7 Remarks

In this section, a basis to select the size of the HA/P/C plate is created through the comparison of axial stiffness of plate and fracture, where dissolution rate and healing rate are used. This analysis shows the reduction in stiffness of the plate is heavily dependent on the form of the dissolution rate, in this case, an exponential relationship with time.

Additionally, computational simulations are performed of an idealized plate attached to a fractured femur with applied loads to demonstrate the effects of a tailored plate as healing rate progresses. Although results for the stress/strain response in the fracture zone are presented, they are mainly used to determine an overall trend in the response in the fracture. Great lengths are taken to interpret the healing rate for the fracture, where linear elastic properties are assigned. Note there is there is a significant stiffness mismatch in the fracture in the early stages of healing, so the results in the fracture are affected by this discontinuity. Overall, the models still serve as a basis for analysis of the plate response to loads while dissolution and healing effects are accounted for.

When the dissolution aspect of degradation over time is integrated into the material response of the plate, it is seen the 4 mm x 12 mm HA/P/C plate reaches strains that exceed the allowable of the material in the day 0 model. This location of these maximum strains, however, is adjacent to the idealized screw interface. Since the attachment of the screw is an idealized representation of the real scenario, the stress concentrations predicted in this area will differ from those in the real case. It is seen

that the strains in the part of the plate that bridge the fracture are half that of the allowable.

At day 35 of dissolution, the maximum strains in the plate are smaller than those experienced at day 0, even though dissolution is already taking place. This is attributed to the change in load transfer as a result of fracture healing, where the fracture carries a majority of the load at day 35. It should be stated here that the same resultant force and moment from the standing load is applied at day 35. To get a more accurate representation of physiological loading conditions, perhaps the load must be increased to reflect the patient's increase in mobility as healing proceeds.

The delayed healing model indicates that a healing rate which may be delayed by two weeks does not negatively impact the HA/P/C plate in regards to strength. As shown in Section 5.6.5, the strains experienced in the 6 mm x 20 mm plate in this model are only 10-15% of the allowable. The elements in the fracture at this stage of healing experience maximum strain 1.2% in tension and 1.7% in compression. The allowables are unknown in the fracture zone at this stage of healing, however, so no determination can be made regarding the fracture stability in this scenario.

In this particular HA/P/C material system, the dissolution rate is such that dissolution of the entire plate is expected to occur after 7 weeks. Although this material system may not be appropriate as a fixation plate because of this dissolution outcome, the process of tailoring the plate based on dissolution shows that the transfer of load as healing progresses should be accounted for in the design of other potential material systems.

6. CONCLUSIONS

In this study, a bioresorbable-based material system is created for potential use in orthopedic applications and experiments are undertaken to examine the degradation characteristics of the system. These experiments are designed to determine the degradation rate at a material scale, avoiding three-dimensional geometry effects of test specimens. Since this degradation rate is one-dimensional, the material degradation rate is then applied in computational simulations to a device on the structural scale; these simulations also incorporate time-dependent bone healing properties.

First, a material system is created by infiltrating carbon foam with a hydroxyapatite/poly($_{D,L}$-lactide)-co-poly(glycolide) (HA/PDLGA) system. The processing technique to create this system is developed and extensive morphological examinations are performed to determine the quality of HA distribution and the presence of defects as a result of processing. These investigations reveal that there is a trade-off in infiltrating the carbon foam: care must be taken when pressing the HA/PDLGA melt through the carbon foam so as not to damage the foam ligaments; however voids occur in the HA/PDLGA phase when too little force is applied in the infiltration process. As shown in the computational predictions of the effective elastic properties of the system, these voids negatively impact the effective modulus, reducing the gains achieved when introducing HA to the system. In addition to the morphological examinations, short-term cell studies with rat calvarial osteoblasts are also performed to establish a starting point for biocompatibility.

In characterizing the degradation rates, diffusion theory is used to design the experiment since degradation is governed in-part by water uptake. Dissolution rates of the material systems are determined based on the specimen mass loss over time. Furthermore, these experiments reveal that the addition of carbon foam to HA/PDLGA, even at 3% by volume, affects both the water uptake of the material as well as the dissolution rate. Additionally, these analyses only take into account time-dependent effects of dissolution of a bioresorbable system. As such, it is learned that this approach is more suitable for a material system in which degradation occurs at a faster rate than water uptake, leading to a surface erosion mode of degradation. In order to more accurately account for degradation in materials which absorb water on the same order as degrade, a relationship between modulus and water concentration must be made and integrated into the approach.

Computational analyses are performed to predict the elastic effective modulus and strength of the HA/P/C system as processed. These simulations capture the effects of the foam microstructure on the composite material, as well as the change in load paths as a result of the carbon foam.

Finally, as a demonstration of tailoring a bioresorbable material based on time-dependent properties, a computational analysis is performed to study the response of an internal fixation plate attached to a transversely fractured femur. Here, the dissolution rate is applied to the HA/P/C plate and a fracture healing rate is derived based on mechano-regulation studies in the literature. A basis to select the size of the HA/P/C plate is created through the comparison of axial stiffness of plate and fracture, where

dissolution rate and healing rate are used. This analysis shows the reduction in stiffness of the plate is heavily dependent on the form of the dissolution rate, in this case, an exponential relationship with time. Computational simulations are performed of an idealized plate attached to an idealized femur with applied loads to demonstrate the effects of a tailored plate as healing rate progresses.

REFERENCES

1. Kulkarni RK, Pani KC, Neuman C, Leonard F. Polylactic acid for surgical implants. Arch Surg 1966;93(5):839-843.

2. Kohn J, Abramsom S, Langer R. Bioresorbable and bioerodible materials. In: Ratner BD, Hoffman AS, Schoen FJ, Lemons JE, editors. Biomaterials science: An introduction to materials in medicine. 2nd ed. Amsterdam: Elsevier Academic Press, 2004. p. 115-127.

3. Gilbert JA. Stress protection osteopenia due to rigid plating. Clinical Biomechanics 1988;3(3):179-186.

4. Frost HM. Bone remodelling dynamics. Springfield, IL: Charles C Thomas, 1963.

5. Cowin SC. Bone mechanics handbook. 2nd ed. Boca Raton, FL: CRC Press, 2001.

6. Cowin SC. The false premise in wolff's law. In: Cowin SC, editor. Bone biomechanics handbook. Boca Raton, FL: CRC Press, 2001. p. 30-31.

7. Ruff C, Holt B, Trinkaus B. Who's afraid of the big bad Wolff?: "Wolff's law" And bone functional adaptation. American Journal of Physical Anthropology 2006;129(4):484-498.

8. Barber FA. Resorbable fixation devices: A product guide. Orthopedics (Special Edition) 1998;4:1111-1117.

9. Middleton JC, Tipton AJ. Synthetic biodegradable polymers as orthopedic devices. Biomaterials 2000;21(23):2335-2346.

10. Middleton JC, Tipton AI. Synthetic biodegradable polymers as medical devices. Medical Plastic and Biomaterials 1998;5:30-39.

11. Pietrzak WS. Principles of development and use of absorbable internal fixation. Tissue Eng 2000;6(4):425-433.

12. Black J, Hastings GW. Handbook of biomaterial properties. London: Chapman & Hall, 1998.

13. Ramakrishna S, Mayer J, Wintermantel E, Leong KW. Biomedical applications of polymer-composite materials: A review. Composites Science and Technology 2001;61(9):1189-1224.

14. An YH, Woolf SK, Friedman RJ. Pre-clinical in vivo evaluation of orthopaedic bioabsorbable devices. Biomaterials 2000;21(24):2635-2652.

15. Pachence JM, Bohrer MP, Kohn J, Robert L, Robert L, Joseph V. Biodegradable polymers. In: Lanza R, Langer R, Vacanti J, editors. Principles of tissue engineering. 3rd ed. Burlington, VT: Academic Press, 2007. p. 323-339.

16. Nair LS, Laurencin CT. Biodegradable polymers as biomaterials. Progress in Polymer Science 2007;32(8-9):762-798.

17. Gunatillake P, Mayadunne R, Adhikari R, El-Gewely MR. Recent developments in biodegradable synthetic polymers. Biotechnology Annual Review 2006;12:301-347.

18. Mano JF, Sousa RA, Boesel LF, Neves NM, Reis RL. Bioinert, biodegradable and injectable polymeric matrix composites for hard tissue replacement: State of the art and recent developments. Composites Science and Technology 2004;64(6):789-817.

19. Göpferich A. Mechanisms of polymer degradation and elimination. In: Domb AJ, Kost J, Wiseman DM, editors. Handbook of biodegradable polymers. Amsterdam: Harwood Academic Publishers, 1997. p. 451-472.

20. Burkersroda Fv, Schedl L, Göpferich A. Why degradable polymers undergo surface erosion or bulk erosion. Biomaterials 2002;23(21):4221-4231.

21. Schenderlein S, Luck M, Muller BW. Partial solubility parameters of poly(d,l-lactide-co-glycolide). International Journal of Pharmaceutics 2004;286(1-2):19-26.

22. Hasirci V. Biodegradable biomedical polymers: A review of degradation of and in vivo response to polylactides and polyhydroxyalkanoates. In: Wise DL, editor. Biomaterials and bioengineering handbook. New York: Marcel Dekker, Inc., 2000. p. 141-155.

23. Murugan R, Ramakrishna S. Development of nanocomposites for bone grafting. Composites Science and Technology 2005;65(15-16):2385-2406.

24. Zhang K, Wang Y, Hillmyer MA, Francis LF. Processing and properties of porous poly(l-lactide)/bioactive glass composites. Biomaterials 2004;25(13):2489-2500.

25. Bleach NC, Nazhat SN, Tanner KE, Kellomaki M, Tormala P. Effect of filler content on mechanical and dynamic mechanical properties of particulate biphasic calcium phosphate-polylactide composites. Biomaterials 2002;23(7):1579-1585.

26. Boccaccini AR, Maquet V. Bioresorbable and bioactive polymer/bioglass® composites with tailored pore structure for tissue engineering applications. Composites Science and Technology 2003;63(16):2417-2429.

27. Ramay HRR, Zhang M. Biphasic calcium phosphate nanocomposite porous scaffolds for load-bearing bone tissue engineering. Biomaterials 2004;25(21):5171-5180.

28. Wei G, Ma PX. Structure and properties of nano-hydroxyapatite/polymer composite scaffolds for bone tissue engineering. Biomaterials 2004;25(19):4749-4757.

29. Furukawa T, Matsusue Y, Yasunaga T, Shikinami Y, Okuno M, Nakamura T. Biodegradation behavior of ultra-high-strength hydroxyapatite/poly (l-lactide) composite rods for internal fixation of bone fractures. Biomaterials 2000;21(9):889-898.

30. Dauner M, Planck H, Caramaro L, Missirlis Y, Panagiotopoulos E. Resorbable continuous-fibre reinforced polymers for osteosynthesis. Journal of Materials Science: Materials in Medicine 1998;9(3):173-179.

31. Shikinami Y, Okuno M. Bioresorbable devices made of forged composites of hydroxyapatite (HA) particles and poly-l-lactide (PLLA): Part i. Basic characteristics. Biomaterials 1999;20(9):859-877.

32. Shikinami Y, Okuno M. Bioresorbable devices made of forged composites of hydroxyapatite (HA) particles and poly-l-lactide (PLLA). Part ii: Practical properties of miniscrews and miniplates. Biomaterials 2001;22(23):3197-3211.

33. Shikinami Y, Okuno M. Mechanical evaluation of novel spinal interbody fusion cages made of bioactive, resorbable composites. Biomaterials 2003;24(18):3161-3170.

34. Balac I, Uskokovic PS, Ignjatovic N, Aleksic R, Uskokovic D. Stress analysis in hydroxyapatite/poly-l-lactide composite biomaterials. Computational Materials Science 2001;20(2):275-283.

35. Guild FJ, Bonfield W. Predictive modelling of the mechanical properties and failure processes in hydroxyapatite-polyethylene (hapex^{tm}) composite. Journal of Materials Science: Materials in Medicine 1998;9(9):497-502.

36. Fan JP, Tsui CP, Tang CY. Modeling of the mechanical behavior of HA/PEEK biocomposite under quasi-static tensile load. Materials Science and Engineering A 2004;382(1-2):341-350.

37. Veerabagu S, Fujihara K, Dasari GR, Ramakrishna S. Strain distribution analysis of braided composite bone plates. Composites Science and Technology 2003;63(3-4):427-435.

38. Cox T, Kohn MW, Impelluso T. Computerized analysis of resorbable polymer plates and screws for the rigid fixation of mandibular angle fractures. Journal of Oral and Maxillofacial Surgery 2003;61(4):481-487.

39. Gibson LJ, Ashby MF. Cellular solids - structure and properties. Cambridge: Cambridge University Press, 1997.

40. Cowlard FC, Lewis JC. Vitreous carbon - a new form of carbon. Journal of Materials Science 1967;2(6):507-512.

41. Gallego NC, Klett JW. Carbon foams for thermal management. Carbon 2003;41(7):1461-1466.

42. Wang J. Reticulated vitreous carbon - a new versatile electrode material. Electrochimica Acta 1981;26(12):1721-1726.

43. Gong L, Kyriakides S, Jang WY. Compressive response of open-cell foams. Part i: Morphology and elastic properties. International Journal of Solids and Structures 2005;42(5-6):1355-1379.

44. Sivalingam G, Madras G. Thermal degradation of binary physical mixtures and copolymers of poly(ε-caprolactone), poly(d,l-lactide), poly(glycolide). Polymer Degradation and Stability 2004;84(3):393-398.

45. D'Antone S, Bignotti F, Sartore L, D'Amore A, Spagnoli G, Penco M. Thermogravimetric investigation of two classes of block copolymers based on poly(lactic-glycolic acid) and poly(ε-caprolactone) or poly(ethylene glycol). Polymer Degradation and Stability 2001;74(1):119-124.

46. Groenewoud W. Characterisation of polymers by thermal analysis. First ed. Amsterdam: Elsevier, 2001.

47. ASTM D790: Standard test methods for flexural properties of unreinforced and reinforced plastics and electrical insulating materials. West Conshohocken, PA: ASTM International, 2003.

48. Hasegawa S, Ishii S, Tamura J, Furukawa T, Neo M, Matsusue Y, et al. A 5-7 year in vivo study of high-strength hydroxyapatite/poly(l-lactide) composite rods for the internal fixation of bone fractures. Biomaterials 2006;27(8):1327-1332.

49. Hahn M, McHale M, Wang E, Schmedlen R, West J. Physiologic pulsatile flow bioreactor conditioning of poly(ethylene glycol)-based tissue engineered vascular grafts. Annals of Biomedical Engineering 2007;35(2):190-200.

50. Ellis EA, Pendleton MW. Vapor coating: A simple, economical procedure for preparing difficult specimens for scanning electron microscopy. Microscopy Today 2007;15(4):44.

51. Brown GM, Butler JH. New method for the characterization of domain morphology of polymer blends using ruthenium tetroxide staining and low voltage scanning electron microscopy (LVSEM). Polymer 1997;38(15):3937-3945.

52. Neogi P. Diffusion in polymers. New York: Marcel Dekker, 1996.

53. Crank J. The mathematics of diffusion. 2nd ed. Oxford: Clarendon Press, 1975.

54. Grayson ACR, Cima MJ, Langer R. Molecular release from a polymeric microreservoir device: Influence of chemistry, polymer swelling, and loading on device performance. Journal of Biomedical Materials Research Part A 2004;69A(3):502-512.

55. Grayson ACR, Cima MJ, Langer R. Size and temperature effects on poly(lactic-co-glycolic acid) degradation and microreservoir device performance. Biomaterials 2005;26(14):2137-2145.

56. Eshelby JD. The determination of the elastic field of an ellipsoidal inclusion, and related problems. Proceedings of the Royal Society of London Series A, Mathematical and Physical Sciences 1957;241(1226):376-396.

57. Benveniste Y. A new approach to the application of mori-tanaka's theory in composite materials. Mechanics of Materials 1987;6(2):147-157.

58. Mori T, Tanaka K. Average stress in matrix and average elastic energy of materials with misfitting inclusions. Acta Metallurgica 1973;21(5):571-574.

59. Berryman JG, Berge PA. Critique of two explicit schemes for estimating elastic properties of multiphase composites. Mechanics of Materials 1996;22(2):149-164.

60. Christensen RM. A critical evaluation for a class of micro-mechanics models. Journal of the Mechanics and Physics of Solids 1990;38(3):379-404.

61. Entchev PB, Lagoudas DC. Modeling porous shape memory alloys using micromechanical averaging techniques. Mechanics of Materials 2002;34(1):1-24.

62. Li K, Gao XL, Roy AK. Micromechanics model for three-dimensional open-cell foams using a tetrakaidecahedral unit cell and Castigliano's second theorem. Composites Science and Technology 2003;63(12):1769-1781.

63. Gong L, Kyriakides S. Compressive response of open cell foams part ii: Initiation and evolution of crushing. International Journal of Solids and Structures 2005;42(5-6):1381-1399.

64. Gong L, Kyriakides S, Triantafyllidis N. On the stability of kelvin cell foams under compressive loads. Journal of the Mechanics and Physics of Solids 2005;53(4):771-794.

65. Laroussi M, Sab K, Alaoui A. Foam mechanics: Nonlinear response of an elastic 3d-periodic microstructure. International Journal of Solids and Structures 2002;39(13-14):3599-3623.

66. Sihn SW, Roy AK. Modeling and prediction of bulk properties of open-cell carbon foam. Journal of the Mechanics and Physics of Solids 2004;52(1):167-191.

67. Sullivan RM, Ghosn LJ, Lerch BA. A general tetrakaidecahedron model for open-celled foams. International Journal of Solids and Structures 2008;45(6):1754-1765.

68. Hollister SJ, Levy RA, Chu T-M, Halloran JW, Feinberg SE. An image-based approach for designing and manufacturing craniofacial scaffolds. International Journal of Oral and Maxillofacial Surgery 2000;29(1):66-66.

69. Abaqus analysis user's manual. Fourth ed. Pawtucket, RI: Hibbit, Karlsson & Sorensen, Inc., 1993.

70. Perez A, Mahar A, Negus C, Newton P, Impelluso T. A computational evaluation of the effect of intramedullary nail material properties on the stabilization of simulated femoral shaft fractures. Medical Engineering & Physics 2008;30(6):755-760.

71. Lee W, Frossard L, Cairns N, Branemark R, Evans J, Adam C, et al. Finite element modeling to aid in refining the rehabilitation of amputees using osseointegrated prostheses. In: Duffy VD, editor. Digital human modeling. Berlin: Springer, 2007. p. 655-658.

72. Cheung G, Zalzal P, Bhandari M, Spelt JK, Papini M. Finite element analysis of a femoral retrograde intramedullary nail subject to gait loading. Medical Engineering & Physics 2004;26(2):93-108.

73. Andreykiv A, van Keulen F, Prendergast P. Simulation of fracture healing incorporating mechanoregulation of tissue differentiation and dispersal/proliferation of cells. Biomechanics and Modeling in Mechanobiology 2008;7(6):443-461.

74. Claes L. Biomechanics of fracture healing. Journal of Biomechanics 2006;39(Supplement 1):S8-S9.

75. Claes LE, Heigele CA. Magnitudes of local stress and strain along bony surfaces predict the course and type of fracture healing. Journal of Biomechanics 1999;32(3):255-266.

76. Gardner TN, Stoll T, Marks L, Mishra S, Knothe Tate M. The influence of mechanical stimulus on the pattern of tissue differentiation in a long bone fracture - an FEM study. Journal of Biomechanics 2000;33(4):415-425.

77. Hanna Isaksson CCvDRHKI. Corroboration of mechanoregulatory algorithms for tissue differentiation during fracture healing: Comparison with in vivo results. Journal of Orthopaedic Research 2006;24(5):898-907.

78. Isaksson H, Wilson W, van Donkelaar CC, Huiskes R, Ito K. Comparison of biophysical stimuli for mechano-regulation of tissue differentiation during fracture healing. Journal of Biomechanics 2006;39(8):1507-1516.

79. Lacroix D, Prendergast PJ. A mechano-regulation model for tissue differentiation during fracture healing: Analysis of gap size and loading. Journal of Biomechanics 2002;35(9):1163-1171.

80. Bartel DL, Davy DT, Keaveny TM. Orthopaedic biomechanics: Mechanics and design in musculoskeletal systems. Upper Saddle River, NJ: Pearson / Prentice Hall, 2006.

81. Borgeaud M, Cordey J, Leyvraz PF, Perren SM. Mechanical analysis of the bone to plate interface of the lc-dcp and of the pc-fix on human femora. Injury 2000;31(Supplement 3):29-36.

82. Cordey J, Borgeaud M, Perren SM. Force transfer between the plate and the bone: Relative importance of the bending stiffness of the screws and the friction between plate and bone. Injury 2000;31(Supplement 3):21-28.

83. Krishna KR, Sridhar I, Ghista DN. Analysis of the helical plate for bone fracture fixation. Injury 2008;39(12):1421-1436.

84. Talbot M, Zdero R, Garneau D, Cole PA, Schemitsch EH. Fixation of long bone segmental defects: A biomechanical study. Injury 2008;39(2):181-186.

85. Zdero R, Walker R, Waddell J, Schemitsch E. Biomechanical evaluation of periprosthetic femoral fracture fixation. Journal of Bone & Joint Surgery 2008;90-A(5):1068-1077.

86. Disegi JA. Titanium alloys for fracture fixation implants. Injury 2000;31(Supplement 4):D14-D17.

87. Ganesh VK, Ramakrishna K, Ghista D. Biomechanics of bone-fracture fixation by stiffness-graded plates in comparison with stainless-steel plates. BioMedical Engineering OnLine 2005;4(1):46.

APPENDIX A

The solution to the concentration profile $C(x,t)$ using Fick's 2nd law with the initial boundary conditions on a thin specimen as shown in Figure A.1 is given by Crank as

$$\frac{C - C_O}{C_1 - C_O} = 1 - \frac{4}{\pi}\sum_{n=0}^{\infty}\frac{(-1)^n}{2n+1}\cos\frac{(2n+1)\pi x}{2l}\,exp\left[\frac{-D(2n+1)^2\pi^2 t}{4l^2}\right] \qquad \textbf{(A.1)}$$

To find the entire amount of substance absorbed in the specimen at time t, Equation A.1 must be integrated over the thickness. As such, letting M_t denote the total moisture content at time t and M_∞ denote total moisture content at time ∞, M_t is found by integrating Eqn (3.5) over the specimen thickness

$$M_t = \int_{-l}^{l} C(x,t)\,dx \qquad \textbf{(A.2)}$$

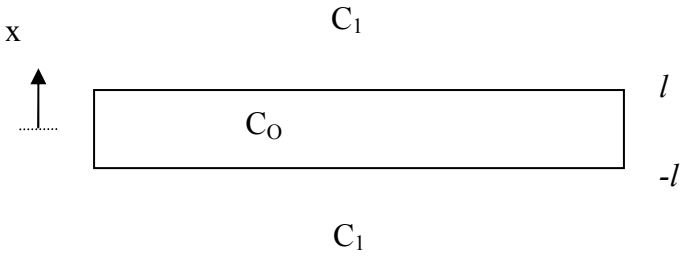

$C = C_O$ at $-l < x < l$ for $t = 0$

$C = C_1$ at $x = -l$ for $t \geq 0$
$x = l$

Figure A.1. Initial and boundary conditions on a thin specimen with l half-thickness.

Substituting Equation A.1 into A.2 and setting C_O = 0 for the case where there is no initial moisture content, results in

$$M_t = \int_{-l}^{l} \left(C_1 - \frac{4}{\pi} C_1 \sum_{n=0}^{\infty} \frac{(-1)^n}{2n+1} \cos \frac{(2n+1)\pi x}{2l} exp \left[\frac{-D(2n+1)^2 \pi^2 t}{4l^2} \right] \right) dx \qquad \textbf{(A.3)}$$

or

$$M_t = \int_{-l}^{l} C_1 dx - \frac{4}{\pi} C_1 \int_{-l}^{l} \sum_{n=0}^{\infty} \frac{(-1)^n}{2n+1} \cos \frac{(2n+1)\pi x}{2l} exp \left[\frac{-D(2n+1)^2 \pi^2 t}{4l^2} \right] dx \qquad \textbf{(A.4)}$$

Applying the rule $\int \sum_{r=a}^{b} f(r,x)dx = \sum_{r=a}^{b} \int f(r,x)dx$, Equation A.4 is rewritten as

$$M_t = \int_{-l}^{l} C_1 dx - \frac{4}{\pi} C_1 \sum_{n=0}^{\infty} \int_{-l}^{l} \frac{(-1)^n}{2n+1} \cos \frac{(2n+1)\pi x}{2l} exp \left[\frac{-D(2n+1)^2 \pi^2 t}{4l^2} \right] dx \qquad \textbf{(A.5)}$$

Solving the second term on the RHS of Equation A.5 results in

$$\frac{4}{\pi} C_1 \sum_{n=0}^{\infty} \left(\frac{(-1)^n}{(2n+1)} \frac{2l}{(2n+1)\pi} \sin \frac{(2n+1)\pi x}{2l} exp \left[\frac{-D(2n+1)^2 \pi^2 t}{4l^2} \right] + A \right)_{x=-l}^{x=l} \qquad \textbf{(A.6)}$$

Evaluating Equation A.6 for $x = l$ and $x = -l$ gives

$$\begin{aligned} &\frac{4}{\pi} C_1 \sum_{n=0}^{\infty} \left[(-1)^n \frac{2l}{(2n+1)^2 \pi} \sin \frac{(2n+1)\pi}{2} exp \left[\frac{-D(2n+1)^2 \pi^2 t}{4l^2} \right] \right. \\ &\left. - (-1)^n \frac{2l}{(2n+1)^2 \pi} \sin \frac{-(2n+1)\pi}{2} exp \left[\frac{-D(2n+1)^2 \pi^2 t}{4l^2} \right] \right] \end{aligned} \qquad \textbf{(A.7)}$$

Further evaluating Equation A.7 results in

$$\frac{4}{\pi} C_1 \sum_{n=0}^{\infty} 2 \frac{2l}{(2n+1)^2 \pi} exp \left[\frac{-D(2n+1)^2 \pi^2 t}{4l^2} \right] \qquad \textbf{(A.8)}$$

Evaluating the first term on the RHS of Equation A.5 and rewriting Equation A.8 and substituting into Eqn A.5 results in

$$M_t = 2C_1 l - 2C_1 l \sum_{n=0}^{\infty} \frac{8}{(2n+1)^2 \pi^2} exp\left[\frac{-D(2n+1)^2 \pi^2 t}{4l^2}\right] \quad \textbf{(A.9)}$$

At $t = \infty$ we see that the exponential function is 0, thus

$$M_\infty = 2C_1 l \quad \textbf{(A.10)}$$

Finally dividing Equation A.9 by A.10 results in the form presented by Crank

$$\frac{M_t}{M_\infty} = 1 - \sum_{n=0}^{\infty} \frac{8}{(2n+1)^2 \pi^2} exp\left[\frac{-D(2n+1)^2 \pi^2 t}{4l^2}\right] \quad \textbf{(A.11)}$$

VITA

Douglas Eugene Rodriguez received his Bachelor of Science degree in mechanical engineering from Texas A&M University in December 2000. As an undergraduate, Douglas began research as a participant in the Accelerated B.S./M.S. Program offered in the College of Engineering at Texas A&M. Here, he worked with Professor Ozden O. Ochoa on the experimental and computational analyses of flexible composite tubular. He received his Master of Science degree in mechanical engineering in May 2002.

Douglas began his Ph.D. studies with Dr. Ochoa in January 2003, where he focused on the processing, characterization, and computational analyses of biocomposites for orthopedic applications. He received a NSF Bridge to the Doctorate Fellowship under the Louis Stokes Alliance for Minority Participation program, allowing him to focus his studies on this emerging area. In addition, Douglas performed research at National Taiwan University in the Department of Biomedical Engineering with Dr. Tai-Horng Young as a participant in the NSF East Asia and Pacific Summer Institute program in the summer of 2004. Douglas received his Ph.D. in mechanical engineering in August 2009.

Douglas can be reached at douglas.e.rodriguez@gmail.com or through Dr. Ozden O. Ochoa, Department of Mechanical Engineering, Texas A&M University, College Station, TX 77843-3123.